High Q^2 Diffractive Physics at HERA

John Lomas

THE UNIVERSITY
of MANCHESTER

High Energy Group
Department of Physics and Astronomy
July 1996

A thesis submitted to The University of Manchester for the degree of Doctor of Philosophy in the Faculty of Science and Engineering.

✓

Contents

Abstract

Diffractive processes are studied in the regime of high Q^2 ($Q^2 \gtrsim 100$ GeV^2) for the first time. A sample of events exhibiting little or no hadronic energy in the region of pseudo-rapidity covered by the forward detectors is selected from the data taken during the 1994 running of H1. The limited form of the diffractive proton structure function, $F_2^D(\beta, Q^2, x_{\mathbb{P}})$, is subsequently measured over the kinematic range $140 \leq Q^2 \leq 300$ GeV^2, $2.37 \times 10^{-3} \leq x \leq 0.0133$ and $0.1 \leq \beta \leq 0.9$. The dependence of $F_2^D(\beta, Q^2, x_{\mathbb{P}})$ on $x_{\mathbb{P}}$ is found to be consistent with the form $x_{\mathbb{P}}^{-n}$, where, under the assumption of factorisation $n = 1.08 \pm 0.21_{(stat.)} \pm 0.07_{(sys.)}$. There is, however, some evidence to suggest that factorisation is broken, with n having a quadratic dependence on β. A measurement of the deep inelastic structure of the pomeron, $\tilde{F}_2^D(\beta, Q^2)$, reveals unambiguous scaling violations with a $log(Q^2)$ dependence and is consistent with a highly gluonic pomeron.

Evidence for diffraction in the Charged Current process is sought. One candidate event satisfying all selection criteria is located, from which the upper limit to the diffractive Charged Current cross section is calculated to be $\sigma_{UL}(e^+p \rightarrow \overline{\nu}_e pX \,|\, V > 10\,\mathrm{GeV}) = 8.0 \pm 0.6_{(sys.)}$ pb.

No portion of the work referred to in this thesis has been submitted in support of an application for another degree or qualification of this or any other institute of learning.

The ownership of any intellectual property rights which may be described in this thesis is vested in the University of Manchester, subject to any prior agreement to the contrary, and may not be made available for use by third parties without the written permission of the University, which will prescribe the terms and conditions of any such agreement. So there.

Further information on the conditions under which disclosures and exploitation may take place is available from the Head of Department of Physics and Astronomy.

This work was supported financially by the Particle Physics and Astronomy Research Council (P.P.A.R.C.), formerly the Science and Engineering Research Council (S.E.R.C.), between October 1992 and October 1995.

The author was educated at St. Katherine's School, Pill, Bristol between 1981 and 1988 and in 1991 obtained a first class honours degree in Physics from the University of Manchester. The work presented in this thesis was conducted at DESY, Hamburg and latterly at the University of Manchester.

Dedicated to
Tabs, Toby, Herb and Frankie

Chapter 1

Introduction

One of the main aims of the HERA $e^{\pm}p$ collider is to provide tests of the theory of Quantum Chromodynamics (QCD) via the study of Deep Inelastic scattering (DIS) interactions. In the DIS process, the lepton, mediated by a virtual boson, scatters from one of the partons within the proton. From such a probe the structure of the proton can be determined and is typically expressed in terms of the structure function $F_2^P(x,Q^2)$. Excellent fits to the measured values of $F_2^P(x,Q^2)$ have been obtained from QCD parameterisations.

Diffractive processes, first observed in hadron-hadron collisions, form a significant subset of the DIS sample. Here, the interaction involves the exchange of colourless objects. There exists, as yet, no understanding of these interactions in terms of perturbative QCD and they are modelled phenomenologically with Regge Theory. Within this framework the diffractive process can be seen as the scattering of the incident lepton off a colourless entity emerging from the proton, known as the pomeron. In analogy to the case of lepton-proton scattering, the structure of the pomeron can be investigated through DIS, and quantified in terms of the diffractive structure function $F_2^D(\beta,Q^2,x_{\mathbb{P}},t)$.

HERA provides a unique environment for the study of diffractive physics. The exceptionally high centre of mass energy which can be achieved facilitates measurements in the previously unreachable range of very low x, the Bjorken scaling variable. In this region the diffractive process is expected to be most pronounced.

The main thrust of the analysis presented in this thesis is the observation and subsequent measurement of diffractive DIS phenomena in the hitherto unexplored region of high virtuality, or Q^2. This regime is accessible to Neutral Current processes in which the incident lepton is deflected through a large angle upon collision and Charged Current interactions mediated by the $W^{\pm}$ bosons. Analysis was performed on data obtained during the 1994 running of HERA, prior to which the low luminosities and hence statistics achieved made such a study impracticable.

A brief overview of the HERA collider and a description of the H1 detector is provided in chapter 2. In chapter 3 the general physics of DIS and its understanding through the application of QCD is reviewed. The phenomenology of Regge Theory and the present theoretical and experimental descriptions of diffraction are outlined in chapter 4. Descriptions of the selection of pure high Q^2 Neutral Current and Charged Current samples form chapters 5 and 6 respectively. The work described in chapter 6 is that of the Electroweak group at H1, not of the author. The analysis was repeated by the author and is presented in order to introduce some of the analysis tools used in the subsequent work. In chapters 7 and 8 Neutral Current diffractive events are isolated from which a first measurement of the limited form of the diffractive proton structure function, $F_2^D(\beta, Q^2, x_{\mathbb{P}})$, in the region $Q^2 \gtrsim 85$ GeV^2 is made. A search for diffractive signatures within the Charged Current sample is detailed in chapter 9.

Chapter 2

The H1 Detector

2.1 The HERA Collider

The HERA accelerator is the first electron(positron)-proton collider to be constructed. It is designed to accelerate 210 electron[1] and 30 proton bunches to energies of 30 GeV and 820 GeV respectively. Due to the differing masses of the colliding particles, two independent storage rings are required to achieve this. Both rings, 6.3 km in circumference, are situated in the same tunnel, and the two beams are arranged to intersect at four interaction points, two of which house the general purpose detectors H1 and ZEUS.

The HERA layout is shown in figure 2.1. The lepton ring accepts electrons at 14 GeV from the PETRA II device and accelerates them by means of RF cavities. The electron beam energy attainable is limited by synchrotron radiation and has, as yet, not reached the design value of 30 GeV. In the case of the proton beam the level of synchrotron radiation is negligible and the beam energy is limited by the applied magnetic field. To reach the required energy the proton ring employs liquid-helium cooled superconducting bending magnets with 40 GeV protons injected from PETRA II.

The magnets focus the particles into bunches at intervals of ~ 28.8 m or

---

[1] Unless otherwise stated the term electron refers to both electrons and positrons throughout this work.

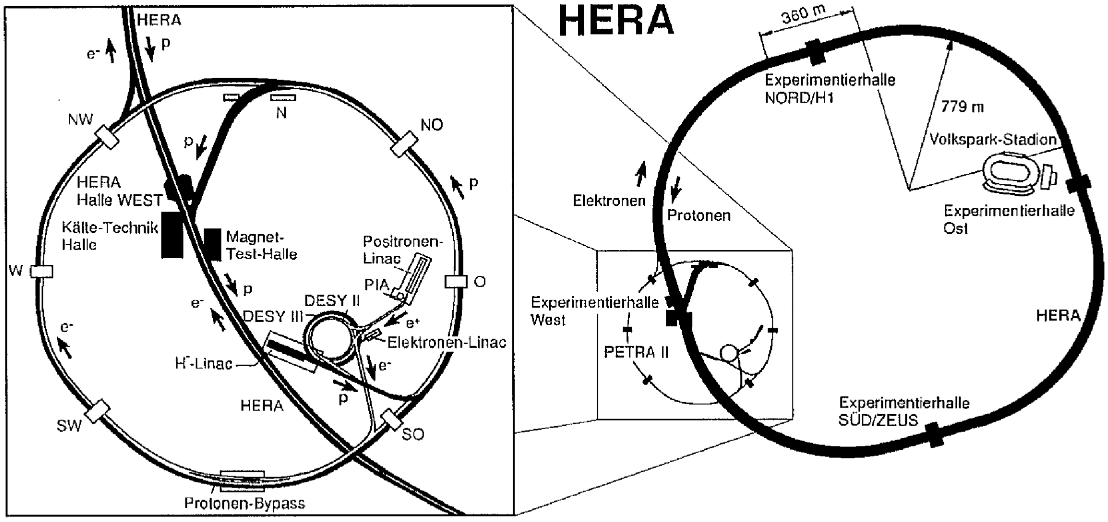

Figure 2.1: The layout of the HERA storage rings.

96 ns. In 1994, the period of data taking considered in this analysis, both electron-proton and positron-proton collisions were performed, the bulk of which being the latter. HERA operated with 153 colliding electron and proton bunches. To facilitate the study of non-collisions backgrounds 32 'pilot' bunches (15 lepton and 17 proton), which have no colliding partner, were also produced. An electron beam energy of 27.5 GeV was achieved for this run period.

2.2 Overview of the H1 Detector

Situated around the northern interaction point at HERA, the H1 detector is designed to identify and measure the direction and energy of particles produced by the $e^{\pm}p$ collisions. The angular coverage is almost 4π, limited only by the space taken up by the beam pipe, the cooling systems and the power readout cabling. A right-handed Cartesian coordinate system (x, y, z) is used to define the position of all points within the detector, with the origin lying at the nominal interaction point and the positive z direction defined by the incoming proton beam. A spherical coordinate system is also defined such that $\theta = 180°$ corresponds to the direction of the incoming electron beam and $\theta = 0°$ to that of the proton.

Two principle methods of particle detection are employed: calorimetry and tracking. Tracking detectors are used to reconstruct the path of charged particles, which, in most cases, are bent by an applied magnetic field allowing momentum measurements to be made. The identification of uncharged particles is impossible for most of the trackers at H1.

Nearly all of the particles incident on the calorimeters are absorbed and their energy converted to a measurable signal. The calorimeters have a finely segmented structure, but not to the extent that individual particles can be resolved. Instead the shape of the energy deposition can be established from groups of particles, or *clusters*, or from an isolated particle, such as a scattered lepton.

The calorimeters act in a complimentary fashion to the trackers: they facilitate the detection of neutral particles and of high energy straight-tracked particles. Low energy particles, poorly measured by the calorimeters, have small radii of curvature thus allowing precise momentum determination by the trackers.

The asymmetric design of H1 is a reflection of the asymmetry of *ep* collisions. The forward region consists of a considerably larger number of detecting systems than the backward, which is devoted almost entirely to the identification and measurement of the scattered electron. The detector also requires a high level of hermeticity and excellent energy resolution in order to measure the missing transverse energy produced in Charged Current DIS events.

A cutaway view of the H1 detector is shown in figure 2.2. The arrangement is cylindrical, with the tracking detectors surrounding the beam pipe, which are in turn surrounded by a layer of calorimeters. A superconducting coil, of radius 3 m, situated around the calorimeters provides a magnetic field of $\sim$ 1.15 Tesla over the central region with $\frac{\Delta B}{B} < 2\%$. The detector is enclosed by an instrumented iron barrel and forward and backward endcaps, which act as the return yoke for the magnetic field. A forward muon spectrometer is located in the forward region. The luminosity system consists of a small angle electron tagger and a very forward situated proton remnant tagger.

The individual detector components are described below.

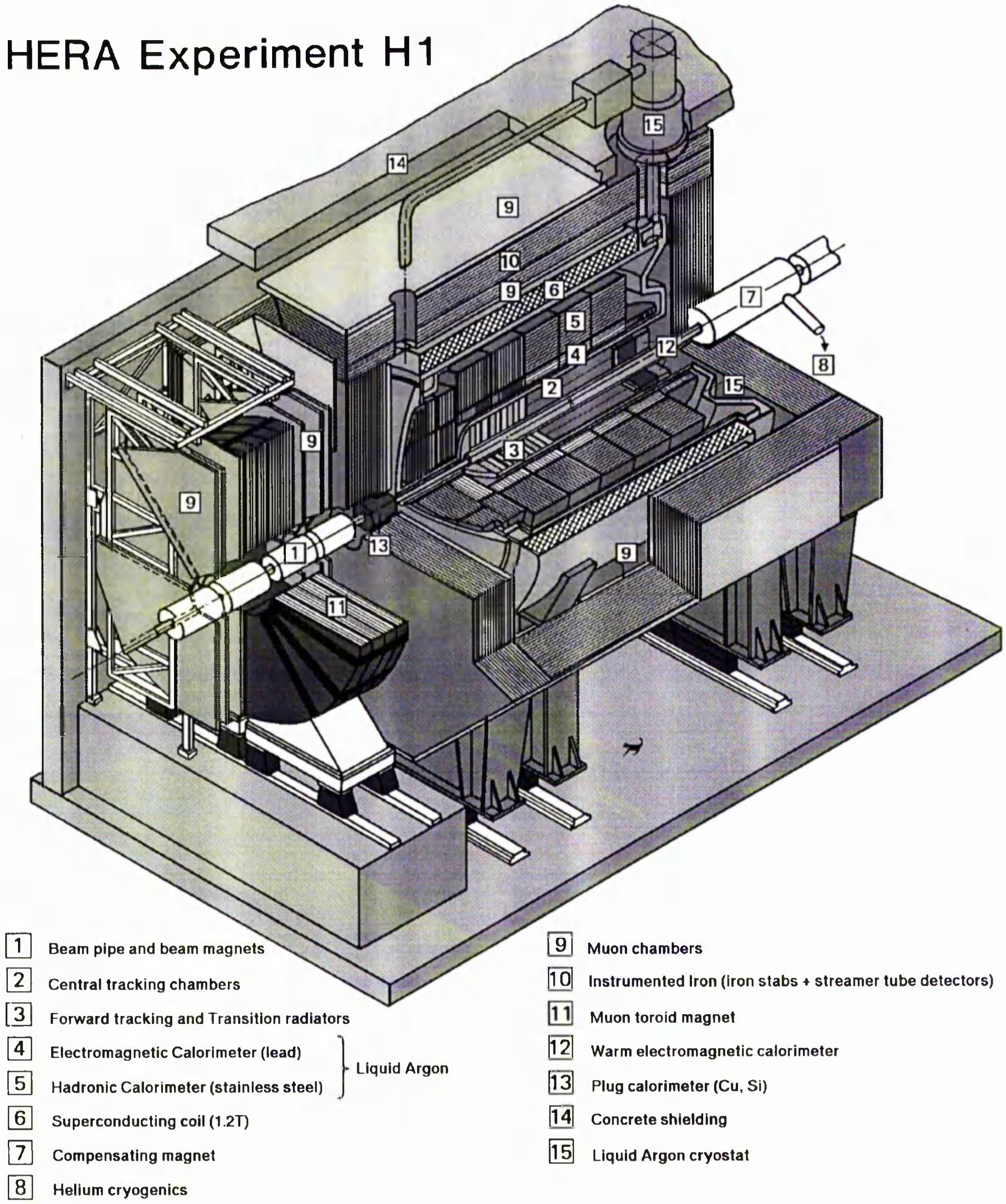

Figure 2.2: Cutaway View of the H1 Detector.

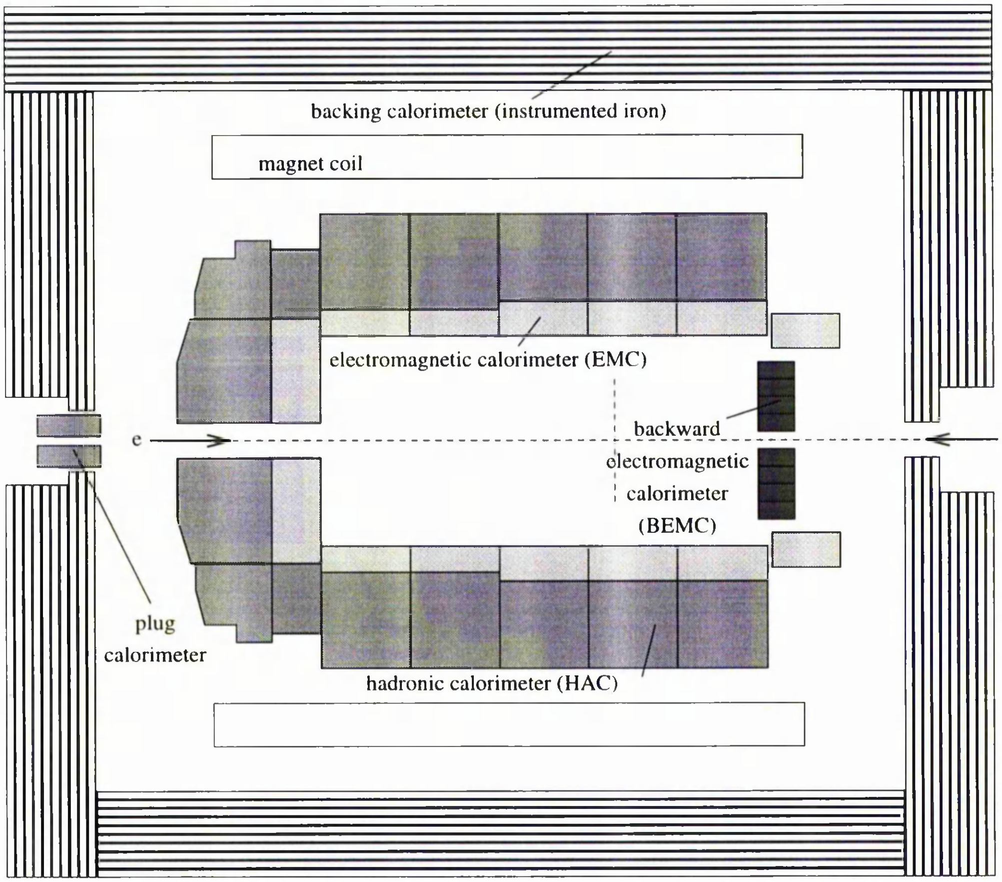

Figure 2.3: The H1 Calorimetry System.

2.3 Calorimetry

The H1 calorimetry system is composed of four separate units: the Liquid Argon (LAr) Calorimeter, the Backward Electromagnetic Calorimeter (BEMC), the Plug Calorimeter and the Tail Catcher, which is situated in the Iron return yoke. The system is shown in figure 2.3.

The H1 calorimeters are all based on the same principle. Layers of passive absorption material are interleaved with gaps containing a sampling component. Particles passing through the absorbing material undergo multiple collisions with the atom contained therein. The secondary particles thus produced interact in the same manner producing yet more particles, eventually resulting in a cascading particle shower. Electromagnetic particles, photons and electrons, lose energy from their collisions with the atoms of the absorber via the processes of bremsstrahlung and pair-production. The resulting shower development is characterised by the radiation length, X_0, the mean distance over which the electron'senergy drops to 1/e of its incident energy. X_0 is approximately proportional to A/Z^2, where A is the atomic mass and Z the atomic number of the absorbing material. For lead $X_0 = 6.37$ g cm^{-2}. Effective containment of the shower within the calorimeter results in a level of ionisation proportional to the incident particle's energy.

Strongly interacting particles undergo both elastic and inelastic collisions when they traverse the absorber. Secondary hadrons are produced and a shower develops. Hadronic showers develop over much longer distances than electromagnetic, the longitudinal development characterised by the nuclear interaction or absorption length, λ, for which $\lambda \sim 20X_0$ in lead. Two factors considerably complicate measurement of the incident hadron energy. In a hadron shower, a significant fraction (between 20 and 30 %) of the incident hadron energy is lost through processes which do not produce an observable signal, such as the excitation and breakup of nucleons. Secondly, since the hadronic shower will typically contain neutral and charged pions, it has both hadronic and electromagnetic components, with the neutral pions decaying into photons and initiating electromagnetic showering. Compensation for the different response of the calorimeters to electromagnetic and hadronic particles is thus required, further complicated by the large fluctuations in the relative contributions from the respective processes, in order to make meaningful energy measurements.

2.3.1 The LAr Calorimeter

The LAr calorimeter [1] covers the range $4^\circ < \theta < 153^\circ$ and $0^\circ < \phi < 360^\circ$ and is the principle calorimeter used in the detection of the hadronic final state and the scattered electron from high Q^2 events. It is divided into two parts: the Electromagnetic and the Hadronic calorimeter. Both are constructed of layers of metal absorber and employ liquid argon as the sampling medium. The most backward part of the calorimeter is the BBE, a smaller electromagnetic calorimeter covering the polar angle range $146^\circ < \theta < 155^\circ$.

The shower initiated by a particle's path through the calorimeter is periodically sampled by the layers of liquid argon, through ionisation. A high voltage is placed across each gap, and the liberated electrons and argon ions move towards the electrodes producing a measurable signal. Each electrode is rectangular and a few cm^2 in size. These define an active volume or 'cell', each of which give an independent energy measurement. Liquid argon is chosen because of its high atomic density, resulting in a high degree of ionisation and because it is a noble gas, ensuring that liberated charged particles will not undergo further inelastic collisions. The signal is produced from this ionisation over a very small period of time, which is essential for triggering.

The two component structure of the LAr calorimeter allows separation between electromagnetic and hadronic particles. The inner electromagnetic calorimeter is constructed of thin (2.4 mm) lead absorption plates and has a depth varying between $\sim 20X_0$ in the backward direction to $\sim 30X_0$ in the forward, reflecting the asymmetry of the *ep* collisions. The hadronic calorimeter has much thicker steel absorbing sheets (19 mm), with a depth varying similarly between 5λ and 7λ. Iso-lines of X_0 and λ within the two components are shown in figure 2.4. The processes which result in energy loss for electromagnetic particles are far larger than those for hadronic. With most of the incident hadrons passing through the thin sheets of the electromagnetic calorimeter, there is a good chance that any cluster well contained in this region is due to a electron or photon and those in the hadronic part are due to hadrons.

An eight fold ϕ-segmentation with highly non-projective cracks in the hadronic part is used to minimise energy leakage through the cracks. The fine granularity of the calorimeter, with a total of $\sim$ 65000 readout channel facilitates the treatment of electronic noise: only those cells associated with significant energy depositions are retained, isolated cells consistent with noise can be rejected. The non-compensating nature of the LAr calorimeter (its response is $\sim 30\%$ less for hadrons than for electrons) requires a software re-weighting technique [2]. Separation of jet and shower components into hadronic and electromagnetic parts, based on the more localised nature of electromagnetic showers, is performed and the non-compensation is statistically corrected for with the application of a scale factor.

The energy resolution of the LAr calorimeter was measured in test beams

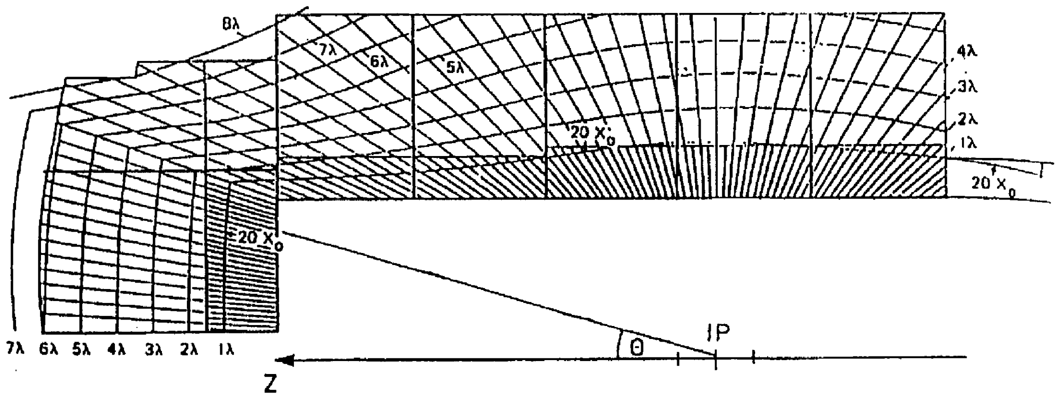

Figure 2.4: Iso-lines of X_0 and λ in the LAr Calorimeter.

to be $\frac{\sigma_E}{E} = \frac{12\%}{\sqrt{E}} \oplus 0.01$ for electrons and $\frac{\sigma_E}{E} = \frac{50\%}{\sqrt{E}} \oplus 0.02$ for charged pions [1, 3]. The absolute scale of the hadronic response has been calculation from studies of the transverse momentum imbalance in DIS events to an accuracy of 5%. The electromagnetic energy scale is presently known to 3% [4].

2.3.2 The Backward Electromagnetic Calorimeter

The BEMC covers the angular range of $151° < \theta < 177°$. Its primary purpose is to measure the energy and position of electrons scattered in the backward direction by low Q^2 (5 GeV $< Q^2 <$100 GeV) Neutral Current DIS events. A secondary aim is the detection of hadrons produced by photoproduction and low x hadronic final states.

The BEMC is a lead scintillator sandwich calorimeter, comprised of 88 stacks, the majority of which are square in cross-section with a size of 159 mm × 159 mm. A simplified transverse view is shown in figure 2.5. Each stack is constructed of 50 sampling layers of 4 mm thick scintillator interleaved with 2.5 mm lead sheets which act as the absorbers. The calorimeter has a depth of $22.5X_0$, or

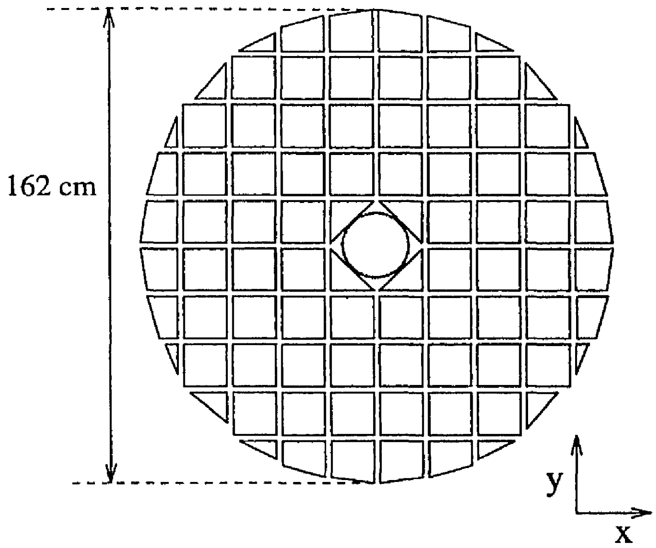

Figure 2.5: Transverse View of the BEMC

0.97λ.

The energy of any shower, initiated in the lead absorption layers, is converted into photons within the scintillator through the process of atomic excitation. Photodiodes connected to wavelength shifters, which run along the length of each stack, convert the photons produced into an electrical signal. Each wavelength shifter is assigned to a separate read-out channel, the total number of which is 472.

From test beam studies with electrons in the energy range 1 GeV $< E_e <$ 80 GeV, the electromagnetic energy resolution is assessed to be $\frac{\sigma_E}{E} = \frac{10\%}{\sqrt{E}} \oplus 0.01$ [5]. The uncertainty in the electromagnetic energy scale is estimated to be 1.5% [6]. The BEMC response to hadrons is significantly poorer, with a containment of only about 30% of the incident hadronic energy. If combined with information provided by the Tail Catcher immediately behind the BEMC (see below) a hadronic energy resolution of $\frac{\sigma_E}{E} = \frac{80\%}{\sqrt{E}}$ is possible [5].

2.3.3 The Plug Calorimeter

The Plug is designed to fill the gap between the edge of the LAr Calorimeter and the beam pipe, so minimising the loss of transverse hadronic momentum in the forward region. Situated at 476 cm $< z <$ 545 cm, the Plug covers the angular range $0.7^\circ < \theta < 3.3^\circ$. It comprises of nine layers of 7.5 cm copper absorber interspersed with eight silicon sampling layers, and has a depth of $44.6X_0$ or 4.25λ. The incomplete containment of showers and coarse sampling limit the Plug resolution to $\frac{\sigma_E}{E} \approx \frac{150\%}{\sqrt{E}}$ [5].

2.3.4 The Tail Catcher

The Iron return yoke is instrumented with layers of Limited Streamer Tube (LST) chambers. In addition to their purpose as muon detectors, described in section 2.5, some of the LST layers have calorimetric capabilities and constitute the Tail Catcher. The Tail Catcher is designed to measure the hadronic energy leakage from the LAr Calorimeter and the BEMC.

The LST's are positioned on the outer and inner sides of gaps formed by ten iron laminations. There are a total of 16, of which eleven are connected to readout pads, from which signals are taken. The pads vary in size from 50cm × 40 cm in the barrel region to 30 cm × 30 cm in the forward and backward endcaps. With the iron acting as the absorber, signals are produced from streamers initiated by showering caused by the passage of incident hadrons. The Tail Catcher covers the range $66^\circ < \theta < 172^\circ$ and has a depth of about 4.5λ. Studies performed with μ and π test beams have placed the energy resolution at $\frac{\sigma_E}{E} \approx \frac{100\%}{\sqrt{E}}$ [5].

2.4 Tracking Detectors

The tracking detector system is divided into three physically separate components: the central tracking detector (CTD), the forward tracking detector (FTD), both of which contain drift chambers for precise particle trajectory reconstruction and Multi Wire Proportional Chambers (MWPC's) for rapid triggering, and the

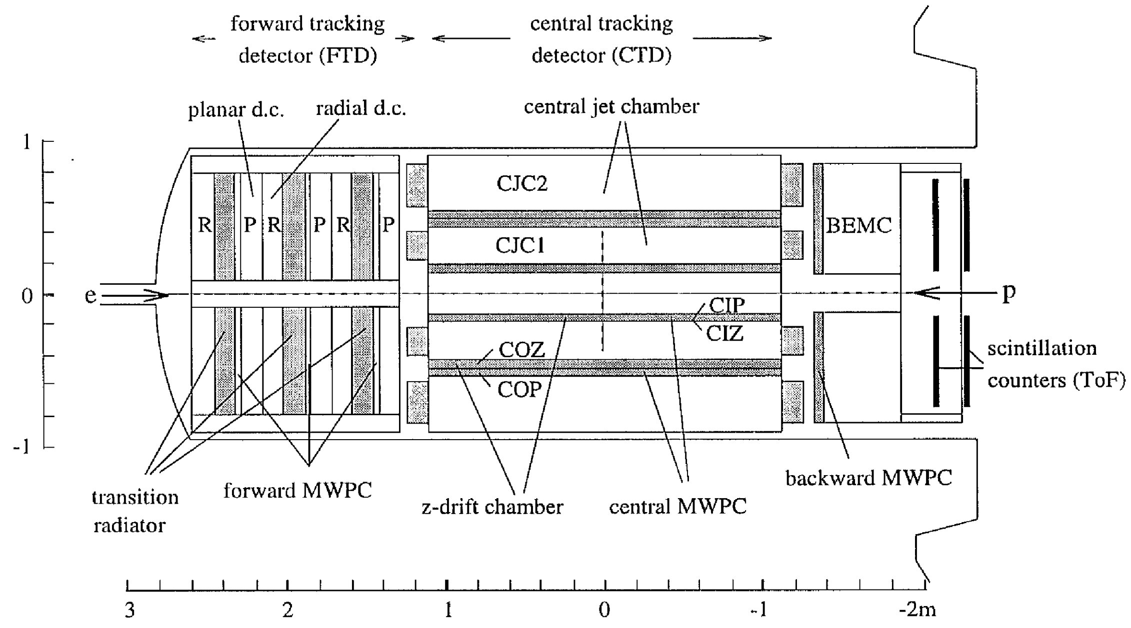

Figure 2.6: An $r-z$ of the H1 Tracking Detectors.

backward MWPC (BPC). As with the LAr Calorimeter the asymmetry of HERA events dictates that the bulk of the instrumentation is in the forward region. The CTD has an angular coverage of $22^\circ < \theta < 165^\circ$, with $7^\circ < \theta < 30^\circ$ covered by the FTD and $155.5^\circ < \theta < 174.5^\circ$ by the BPC. The system is shown in figure 2.6.

Each drift chamber contains a gas which is ionised by a charged particle traversing its volume, and one or more anode sense wires. A moderate electric field is applied across the chamber. Electrons liberated by ionisation drift towards the sense wire until they reach its immediate vicinity (within < 1 mm) where the field increases rapidly in strength. Secondary ionisation then occurs, with the electrons thus produced undergoing further collisions, resulting in an avalanche of electron-ion pairs. The movement of ions away from the sense wire produces an induced current, which passes along the wire to the readout system where it is recorded as a pulse. The time at which the pulse is produced depends on the distance which must be covered by the electrons to reach the region of high field. From the measurement of this time then, the distance of the ionising particle to the wire can determined, usually to an accuracy of a few microns. Comparison of the pulse size received at each end of the wire leads to an estimation of the particles position along the wire, typically with a resolution of a few cm. By combining different orientations of sense wire, the *track* of the particle can be reconstructed with its momentum determined from the degree of curvature caused by the magnetic field. With bunch crossings occurring every 96 ns, the drift distance must be restricted to less than $\sim$ 10 cm (for a typical drift velocity of 50 μm ns^{-1}) to prevent charge deposition from too many collisions occurring simultaneously in the same chamber.

MWPCs employ the same principles as drift chambers, but exclude the drift regions. Closely spaced anode sense wires are arranged such that any incident particle must pass through a region of high field where multiplication can occur. The sense wires or cathode pads placed on the chamber walls can be sampled for pulses. With a very short drift time, there is rapid production of a signal in response to any detected particle making MWPCs very useful for triggering. The position resolution, limited by the separation of the wires, is rather coarse, typically of the order of several mm.

The tracking system is designed to provide an angular resolution of $\sigma_\theta \approx 1$ mradian and a momentum resolution of $\frac{\sigma_P}{P} \approx 0.3\%$ [5].

2.4.1 The Central Tracking Detector

The CTD consists of six cylindrical, co-axial volumes located around the beam pipe. In order of increasing radius the components are: the Inner MWPC (CI P), the Inner z Chamber (CIZ), Inner Central Jet Chamber (CJC1), the Outer z Chamber (COZ), the Outer MWPC (COP) and the Outer Central Jet Chamber (CJC2), as shown in figure 2.7.

The CJC chambers are designed to provide accurate $r - \phi$ track measurement from drift timing. Both are built of cells running the full chamber length parallel to the axis, each containing a plane of parallel sense wires. CJC1 is split into 30 cells containing 24 sense wires, CJC2 contains 60 cells with 32 sense wires. The plane of the wires is tilted at an angle of $\sim 30^\circ$ with respect to the radial coordinate. The reasons for this are twofold. Firstly, the combined effect of the electric field in the cell and of the H1 magnetic field force the secondary electrons produced by stiff (high momentum) tracks to drift at $\sim 90^\circ$ to the track, optimising

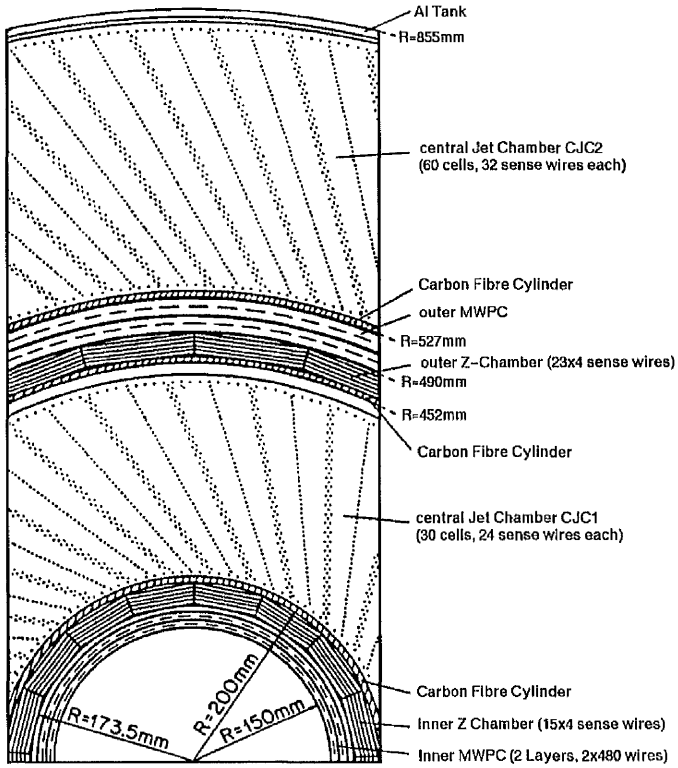

Figure 2.7: An $r - \phi$ cross-section through the Central Tracking Detector.

resolution. Secondly, the tilt ensures that stiff tracks cross wires in both CJC1 and CJC2 and will be detected in more than one cell, so allowing for ambiguities in the $r - \phi$ position of the particle arising from each sense wire measurement.

The z drift chambers provide measurement of the track z position, with a resolution of $\sigma_z \approx 250\mu$mm [5], and a rough determination of $r - \phi$. CIZ is divided into 15 cells, COZ 23, each containing 4 sense wires separated in r. The wires are arranged around the beam pipe to form polygons, 16 sided for CIZ and 24 sided for COZ.

The MWPCs consist of two concentric chamber layers. The output is read from cathode pads, which in the case of CIP, are 36.6 mm long in z and cover 45° in azimuth, giving an eightfold segmentation in ϕ. COP has pads 120 mm in length each with an angular coverage of 22.5°.

2.4.2 The Forward Tracking Detector

The high track density in the forward region makes pattern recognition particularly difficult, so a special set of trackers comprising the FWD was designed instead of simply extending the CTD in z. The FWD consists of three identical *supermodules* each comprising, in order of increasing z: planar chambers, a MWPC, a transition radiator and a radial drift chamber.

Each planar module has three layers of parallel wires orientated at 60° in ϕ to each other. Combination of the drift time measurements from each layer facilitates precise determination of the track $x-y$ coordinates. The MWPCs are similar to those employed in the CTD, and serve the same purpose of rapid signal production with coarse position resolution for triggering. The cathode pads are ring-shaped, with an azimuthal angle coverage of 45° or 22.5° and radial width between 18 mm and 37 mm. The transition radiator consists of a passive array of polypropylene sheets. A charged particle crossing the boundaries of these layers causes the production of soft X-rays (transition radiation) which are subsequently detected in the radial drift chambers. The intensity of the X-rays depends on the Lorentz factor $\gamma = \frac{Energy}{Mass}$, allowing discrimination between electrons and heavier particles. Each of the radial chambers are divided into 48 drift cells covering 7.5° in azimuth. The cells contain 12 sense wires separated in z by 10 mm.

2.4.3 The Backward MWPC

The trackers described above do not efficiently reconstruct tracks produced at polar angles greater than $\sim 155°$. The BPC is designed to fulfill this requirement, giving accurate space-point measurement up to $\theta \sim 175°$, with an angular resolution of ~ 0.5 mradians [5], as well as giving prompt track information for the trigger. Situated behind the CTD, the BPC consists of four wire planes, with each wire separated by a distance of 2.5 mm, orientated at 45° with respect to its neighbours.

2.5 The Muon Detectors

Muon detection is important for heavy flavour studies and to preserve the hermeticity of energy flow measurements.

Besides the hadronic Tail Catcher capabilities discussed in section 2.3.4, the LST system provides the bulk of the muon detection at H1. Each LST has a square cross-section of 1 cm^2 and a contains a single wire running along the length of the tube. Three of the four walls of each tube have a low surface resistivity onto which a high voltage is placed. The wire is earthed. Signals can be read directly from the wire, or from pads or 4 mm wide aluminium strips mounted on the high resistance covers of the tubes. Five of the 16 LST's are fitted with strips, which run perpendicular to the wires, the remaining eleven possessing pads. From the wire signals, the position of an incident muon can be determined with a resolution of 3-4 mm, compared to 10-15 mm from strip signals and 10 cm from the pads [5]. A momentum measurement is possible using the field of the Iron return yoke, but this better achieved with the identification of the muon track in the CTD from reconstruction of the track in the Iron. An energy of approximately 1.2 GeV is required for the muon to reach the Iron in the barrel region, and $\approx$ 2.5 GeV for penetration in the forward region.

In response to the high density of tracks in the forward region of H1 and the fact that the Iron is not sufficient for accurate measurement of the momenta of muons at $\theta < 17°$, muon detection is supplemented by a separate spectrometer, the Forward Muon Detector (FMD) [7]. Situated forward of the forward Iron endcap, the FMD consists of three octagonal double planes of drift chambers situated either side of an iron toroidal magnet which produces a field of $\sim$ 1.5 Tesla. The system is independent of the H1 solenoidal magnet. On each side of the magnet the central chamber layer is designed to measure the azimuthal angle ϕ, the two on either side measuring the polar angle. The entire system contains a total of 1520 cells, all with a rectangular cross-section of 2 cm $\times$ 12 cm and lengths varying between 40 cm and 240 cm.

Muons with momenta greater than 5 GeV in the angular range $3° < \theta < 17°$ can be detected and an independent momentum measurement made up to 200 GeV. The momentum resolution is $\frac{\sigma_P}{P} = 24\%$ for 5 GeV tracks deteriorating gradually at higher momenta [7]. The FMD is preferably used, however, to identify the track left by the muon in the forward tracker from which a more precise determination of the momentum is possible.

2.6 Scintillator Walls

Two scintillator wall systems are used in H1, the Time of Flight (ToF) system and the Veto Walls. Both employ the same principles in order to distinguish between proton induced background and genuine *ep* collisions. The ToF consists of two walls of scintillators situated between the BEMC and the backward Iron endcap ($z = -2$ m). The inner and outer Veto Walls are situated outside the Iron yoke at $z = -6.5$ m and $z = -8.1$ m respectively.

The scintillator detectors work on the principle that particles resulting from *ep* collisions arrive at the scintillator at a different time to those from background interactions. If a proton upstream of H1 interacts with a gas particle or part of the beam pipe, then the products of that interaction will reach the scintillators at about the same time as the proton bunch, from which the proton originated. Particles produced in *ep* collisions will arrive some time later, in fact at about the same time as the electron bunch. The time difference is $\sim$ 13 ns with a variation due to the length of the proton bunch (2-3 ns).

The two plastic scintillator planes of the ToF cover an area roughly equivalent to that of the BEMC and are mounted perpendicular to the beam pipe. The more forward plane is segmented into 16 separate counters, with an eight-fold segmentation being employed in the backward plane, approximating the BEMC granularity. The scintillators are protected from the effects of synchrotron radiation by 6.5 mm thick lead plates. PM tubes are situated at the rear of the planes. For a hit to be recorded a coincidence between each of the ToF planes is required, so as to reduce the effects of electronic noise in the PM tubes. Three time-windows are defined with respect to the beam crossing time:

- *Global* - designed to include all hits associated with a particular beam crossing, with a width of 96 ns.

- *Background* - defined around the time at which the particles produced from upstream proton background events are expected, with a width of 25 ns.
- *Interaction* - this begins at the end of the background window and has a width of 13 ns.

The inner Veto wall extends to 1 m from the beam pipe and has a time resolution of $\sim$ 3 ns. The outer Veto Wall is far larger, covering a cross-sectional area similar to that of the LAr calorimeter and provides a resolution of $\sim$ 8 ns. With all scintillator detectors working in a complementary fashion a reduction in the background rate of $\sim 99\%$ is achieved.

2.7 The Proton Tagger

The forward proton remnant tagger consists of two layers of scintillator sheets sandwiched by lead shielding. Placed at $z = 24$ m, the sheets have an area of 3600 cm^2 around and perpendicular to the beam pipe, resulting in an angular coverage of $0.35^\circ > \theta > 0.04^\circ$ $(5.8 < \eta < 8)$.

2.8 The Luminosity System

Designed as a multipurpose device, the luminosity system consists of the electron tagger and the photon detector, two Čerenkov calorimeters, situated close to the beam pipe at $z = -33$m and $z = -103$m respectively. Their main task is to provide accurate relative and absolute luminosity measurements.

The process used for this calculation is the bremsstrahlung interaction $ep \rightarrow ep\gamma$, with the two detectors required to locate the outgoing electron and photon in coincidence. The cross-section, $\sigma(ep \rightarrow ep\gamma)$ is large and precisely known so, when combined with the measured acceptances of the detectors the luminosity can be found.

The photon tagger consists of a 5×5 array of square-shaped crystals with a depth of 200 mm and a combined transverse size of 100 mm$\times$100 mm. The electron

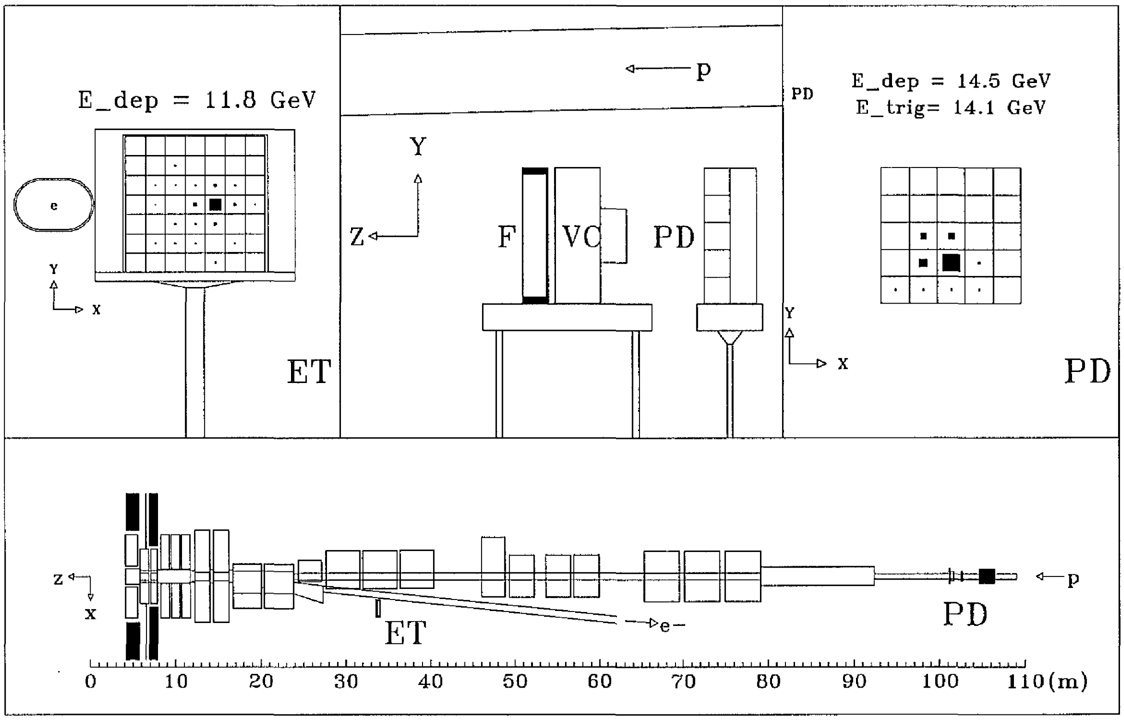

Figure 2.8: The Luminosity System.

tagger uses identical crystals in a 7 × 7 array with a size of 154 mm×154 mm. The energy resolution is $\frac{\sigma_E}{E} = \frac{10\%}{\sqrt{E}} \oplus 0.01$ and the spatial resolution is less than 1 mm.

The principal backgrounds to the monitor are proton beam halo, electron bremsstrahlung off residual beam gas particles and electron synchrotron radiation. Protection from the proton beam background is provided by a lead wall, 2 m in thickness placed upstream from the photon detector along the beam line. A additional lead sheet of thickness $\sim 2X_0$, is used to protect against synchrotron radiation. The remaining background is measured experimentally using electron pilot bunches. The luminosity system is shown in figure 2.8.

The electron tagger is also used for the detection of the low angle scattered electron from photoproduction events.

2.9 Triggering

The purpose of the H1 trigger is to select interesting *ep* collisions and to reject non-collision background. The combined background rate at H1 is $\sim$ 10 kHz. This must be compared with the rate of the dominant physics process, photoproduction, at the design luminosity, of $\sim$ 100 Hz. To deal with the low physics cross-section large proton and electron accelerator beam currents are required, with design values of $I_p = 16$ mA and $I_e = 60$ mA. Such currents are only achievable with HERA running in *multi-bunch* mode, circulating an intended 210 p and e bunches.

A multilevel trigger is used to allow decisions of increasing complexity. At each level rejection of background is made and the volume of data consequently reduced. Two levels of on-line triggering are currently implemented, L1 and L4, ordered in increasing event reconstruction sophistication and decreasing speed of decision making[2].

The L1 trigger represents the first level of triggering and consists of nine different trigger systems each based on the information from a certain subdetector. The signals from these systems are called trigger elements, simple binary conditions which record whether or not a particular physics criterion has been fulfilled. Analysis of these elements leads to a decision as to whether the event is consistent with an *ep* collision or a background process.

The triggering is considerably complicated by the short beam crossing time of 96 ns, as the time taken for the output of signals from the relevant detector systems can be an order of magnitude greater. A 'pipe-lined front end' system is employed to overcome this problem. Here, the information from the last 24 bunch crossings is stored, whilst the initial trigger decision is made and the delays of all incoming signals are adjusted to the proper bunch crossing. During this period only simple reconstruction tasks can take place and only those trigger elements which can retrieve and process information and assign it to the correct bunch crossing within this time can be included. At a rate of one per bunch crossing, the trigger elements are fed to the central trigger. If there is any combination of elements which would indicate a true *ep* interaction a signal is sent to each subdetector and the event is read out. It is not possible for the readout channels to input new information whilst

---

[2] The intermediate levels L2 and L3 are not yet implemented

this output occurs, resulting in a detector 'dead-time' of several ms.

Events passed by the L1 trigger are then sent onto the L4 filter farm. This is a software trigger which acts asynchronously to the rest of the data acquisition system, enabling data taking to continue. The full data of the event is now available. Partial event reconstruction is performed (tracks and clusters are found) in order to reach a more sophisticated decision on the nature of the event.

The data from those events which survive this stage along with $\sim 1\%$ from those which have been rejected (included for monitoring purposes) is compressed and stored on cartridge. These raw data cartridges are far too unwieldy for individual physics analysis. An additional stage in the processing chain has therefore been developed, the L5 Event Classification Scheme, which produces a series of output data sets according to specific physics requirements.

The events undergo full reconstruction using the H1REC reconstruction package and the data is then classified using routines developed by the individual physics working groups. Events can be flagged as belonging to one or more 'classes'. All the classified events are stored permanently on POT (Physics On Tape) cartridges and represent the lowest level of data on which it is possible to perform any detailed physics analysis. The POT selection criteria are sufficiently broad to ensure that the need to return to the raw data is extremely unlikely.

The increase in the data associated with each event obtained from the full reconstruction means that very little reduction in the total data volume is achieved with the POT selections. For this reason a further selection with more stringent criteria is used to produce DSTs (Data Summary Tapes). This facilitates faster access for analysis. For physics processes for which the statistics are relatively low, such as charged current interactions, the DST production can be by-passed and and the first stage of specific physics analysis can be performed directly from the POTs, the results of which can be conveniently stored on tape as a miniPOT.

Chapter 3

Deep Inelastic Scattering at HERA

3.1 Introduction

Electron-proton collisions play a vital role in the determination of the structure of the proton. Such interactions are understood in terms of the quark-parton and standard models. The electron can be seen as a source of mediating bosons: photons, Z^0 and $W^{\pm}$, which interact with the constituents of the proton (quarks and gluons) thus probing its structure. The centre of mass energy which can be reached at HERA is an order of 10 greater than that possible at other, fixed-target, electron-proton scattering experiments. This permits measurements in previously unaccessed kinematic regimes revealing much about the nature of the proton. With information available on the hadronic final state the structure of the pomeron, the entity responsible for the diffractive mechanism, can also be investigated for the first time.

3.2 Deep Inelastic Scattering

Electron-proton scattering can be divided into two classes: Deep Inelastic Scattering (DIS) and photoproduction. The division is governed by the virtuality, Q^2, of the exchange boson, where $Q^2 = -q.q$, with q representing the 4-momentum transfer between the electron and the proton. DIS events are defined as those for which $Q^2 \gg 1$ GeV^2. Here the wavelength of the virtual boson is less than the size of the proton and it interacts with the constituent partons. Events for which the exchange boson is almost on mass shell ($Q^2 \ll 1$ GeV^2) are defined as photoproduction.

The distinction arises from the different treatment required for the interactions within the framework of Quantum Chromodynamics (QCD), used to describe the strong force which binds the constituents of the proton. This predicts that as Q^2 increases the strength of the partonic coupling, represented by the strong coupling constant, α_s, decreases. At the values of Q^2 for which DIS is defined, the strong coupling force becomes sufficiently weak that the quarks within the proton appear to be free, a property known as asymptotic freedom. In this regime perturbative expansion of α_s can be used for precise calculations and Feynman diagram techniques can be applied. At virtuality scales of ~ 1 GeV^2 such a treatment is no longer valid as the perturbative expansions diverge. Phenomenological and non-perturbative models are required.

At HERA energies DIS is dominated by the Neutral Current (NC) process [1]:

$$e^{\pm} + p \rightarrow e^{\pm} + X \tag{3.1}$$

involving the exchange of a virtual photon, or occasionally a Z^0. X represents the hadronic final state recoiling against the electron. Interactions involving the exchange of the charged $W^{\pm}$ bosons are known as Charged Current (CC):

$$e^{+} + p \rightarrow \overline{\nu}_e + X \tag{3.2}$$

where a W^+ is exchanged; and

$$e^{-} + p \rightarrow \nu_e + X \tag{3.3}$$

---

[1] Throughout the later chapters in this work the term DIS refers solely to the NC DIS case.

involving a W^-. These processes and the NC case involving Z^0 exchange contribute significantly only at very high values of Q^2 ($\sim M^2_{W^\pm,Z^0} > 5000$ GeV^2) [8].

3.3 The Kinematics of DIS

An example DIS event is shown schematically in figure 3.1. The kinematics of such an event are usually expressed in terms of the following Lorentz invariant variables:

$$Q^2 = -q^2 = -(k - k')^2 \tag{3.4}$$

the virtuality of the mediating boson;

$$x = \frac{Q^2}{2P.q} \tag{3.5}$$

the Bjorken scaling variable;

$$y = \frac{P.q}{P.k} \tag{3.6}$$

and

$$W^2 = (q + P)^2 = P'^2 \tag{3.7}$$

the total invariant mass of the hadronic final state.

In the infinite momentum frame x can be viewed as the fraction of the proton's momentum carried by the struck parton. The variable y represents the fraction of the incident electron's energy taken by the mediating boson in the proton rest frame i.e. equivalent to a fixed target collision.

The variables are not independent, with x, y and Q^2 related by:

$$Q^2 = xys \tag{3.8}$$

where s is the square of the centre of mass energy of the electron-proton system:

$$s = (P + k)^2 \simeq 2.P.k \simeq 4E_eE_p \tag{3.9}$$

where E_e and E_p are the incident energies of the electron and proton respectively. For data collected during 1994 $s = 90200$ GeV^2 and since the scaling variables x and y are restricted to values between 0 and 1 this represents the maximum value of Q^2 which can be attained. W^2 is related to x and Q^2 by:

$$x = \frac{Q^2}{Q^2 + W^2} \tag{3.10}$$

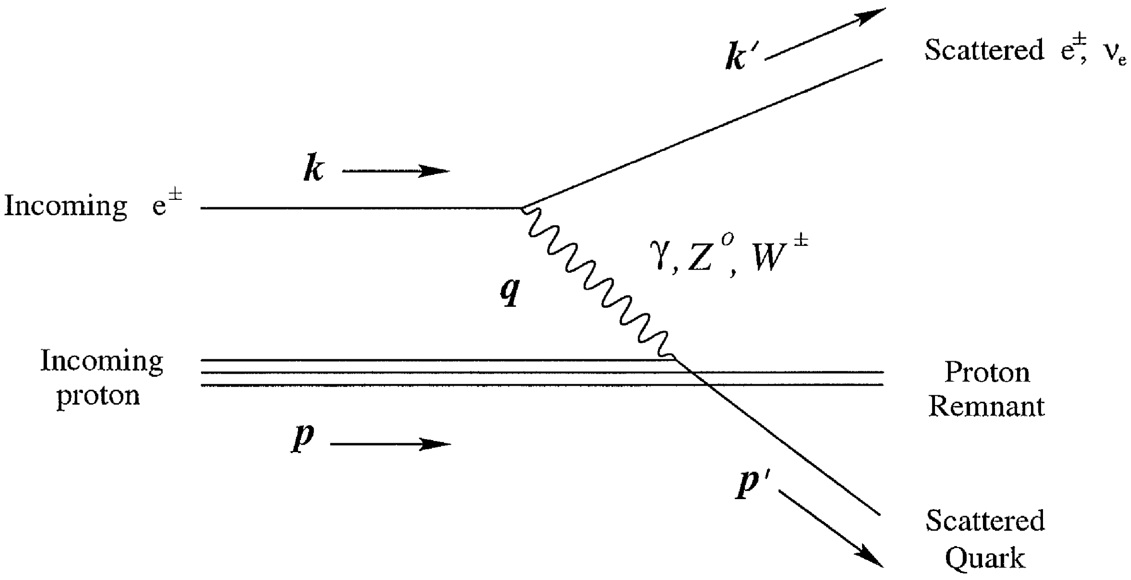

Figure 3.1: The Kinematics of Deep Inelastic *ep* Scattering.

3.4 The DIS Cross Section

The generalised cross section for DIS $e^{\pm}p$ scattering can be expressed as:

$$\frac{d^2\sigma(e^{\pm}p)}{dxdQ^2} = \frac{4\pi\alpha^2}{xQ^4}\left(y^2xF_1(x,Q^2) + (1-y)F_2(x,Q^2) \mp (y - \frac{y^2}{2})F_3(x,Q^2)\right) \quad (3.11)$$

where $\alpha = \frac{e^2}{4\pi}$ is the fine structure constant. The proton structure is represented by the three independent structure functions: F_1, F_2 and F_3. The function F_3 contributes significantly only when $Q^2 \sim M^2_{Z^0,W^{\pm}}$ and is zero by parity invariance for the majority of events which involve photon exchange. It is, however, pertinent to the analysis of CC events, where parity is not conserved.

3.4.1 Scaling and the Quark Parton Model

Quark freedom lies at the heart of the naive parton, or quark parton model (QPM), in which the constituent elements of the proton are non-interacting point-like fermions, called quarks. DIS can then be viewed simply as a two stage process in which the virtual boson interacts with one of the free quarks within the proton and the partons so produced hadronise producing a current jet and leave a proton remnant.

The quarks are assumed to account for all the momentum of the proton, each quarks momentum distribution being described by a parton density function $f_i(x, Q^2)$. Summing over all quark flavours, i, leads to the momentum sum rule:

$$\sum_i \int_0^1 dx x f_i(x) = 1 \tag{3.12}$$

Writing the generalised cross-section (equation 3.11) in terms of the parton density functions leads to the relationships:

$$F_2 \equiv \sum_i e_i^2 x f_i(x) \tag{3.13}$$

and

$$2xF_1 = F_2 \tag{3.14}$$

Equation 3.14 is known as the Callan-Gross relationship and is a direct consequence of the spin-$\frac{1}{2}$ nature of the quarks. Therefore, due to the point-like nature of the protons constituent particles, the structure function F_2 is only dependent on x, not on Q^2, i.e. it is *scale invariant*. This is known as Bjorken Scaling [9]. Indeed, the observation of scaling in DIS at SLAC [10] lead to the formulation of the QPM. Measurements of the ratio $\frac{2xF_1}{F_2}$ at the same institution also confirmed the spin-$\frac{1}{2}$ nature of the quarks.

3.4.2 QCD and Scaling Violations

The QPM prediction that the momentum sum rule would hold (equation 3.12) was contradicted by the experimental results from e^-p and e^-n scattering. The quark constituents of the proton were found to carry $\sim 50\%$ of the total momentum [11]. Scaling was seen to be approximately true in DIS for $x \approx 0.15$, but significant violations were observed at other x values. Such deviations can be accounted for with the theory of QCD.

QCD incorporates the concept of mediating bosons called gluons, which interact through strong interactions with the quarks, which are thus not totally free. The quarks radiate gluons which can subsequently split into $q\overline{q}$ pairs. That the gluons can interact with themselves leads to the decrease in α_s with increasing Q^2 and thus to the concept of asymptotic freedom within QCD described above.

Scaling violations can be viewed qualitatively within the QCD framework: At low Q^2 the structure of the proton cannot be resolved. As the virtuality of the probing boson is increased the quarks are observed to be surrounded by virtual partons arising from the effects of the gluons. Since higher momentum quarks will lose energy through the emission of gluons there is an increased probability of observing a parton at low x and conversely a reduced probability of locating a parton with a high value of x. Therefore at high x values F_2 is expected to decrease with increasing Q^2, contrasting with an increase in F_2 with Q^2 at low values of x.

Another result of taking into account the gluonic content of the proton is that the Callan-Gross relationship no longer holds: $|F_2 - 2xF_1| > 0$ and is often referred to as the *longitudinal* structure function, F_L. The generalised DIS cross section can then be written in terms of $F_{2,3}$ and F_L:

$$\frac{d^2\sigma(e^{\pm}p)}{dxdQ^2} = \frac{4\pi\alpha^2}{xQ^4}\left((1-y+\frac{y^2}{2})F_2(x,Q^2) - \frac{y^2}{2}F_L(x,Q^2) \mp (y-\frac{y^2}{2})F_3(x,Q^2)\right) \tag{3.15}$$

F_L can be seen as the contribution to the cross section due to longitudinally polarised photons and at high values of Q^2 is expected to be small [8].

Formulation of scaling violations can be provided within QCD with the Altarelli-Parisi evolution equations [12], where the quark distribution functions, $f_i(x,Q^2)$, and the gluon distribution function, $g(x,Q^2)$, evolve with Q^2 according to:

$$\frac{df_i(x,Q^2)}{dlogQ^2} = \frac{\alpha_s}{2\pi}\int_x^1 \frac{dy}{y}\left(f_i(y,Q^2)P_{qq}(\frac{x}{y}) + g(y,Q^2)P_{qg}(\frac{x}{y})\right) \tag{3.16}$$

and

$$\frac{dg(x,Q^2)}{dlogQ^2} = \frac{\alpha_s}{2\pi}\int_x^1 \frac{dy}{y}\left(\sum_i f_i(y,Q^2)P_{gq}(\frac{x}{y}) + g(y,Q^2)P_{gg}(\frac{x}{y})\right) \tag{3.17}$$

The splitting function $P_{qq}(\frac{x}{y})$ represents the probability of a quark reducing its momentum by a fraction $(\frac{x}{y})$ through the emission of a gluon. Similarly P_{qg}, P_{gq} and P_{gg} are the splitting functions corresponding to a gluon splitting into a $q\overline{q}$ pair, a quark radiating a gluon (of momentum fraction $(\frac{x}{y})$) and a gluon splitting into a gluon pair ($g \rightarrow g+g$) respectively. The parton density functions at a starting value of Q_0^2 are solved, where Q_0^2 is large enough to allow perturbative calculations and at this scale the quark and gluon content of the proton is constrained by experimental information. The complete set of evolution equations are then used to predict the structure for $Q^2 > Q_0^2$ and for all x.

Certain approximations are required however to facilitate these calculations. The Altarelli-Parisi formulation assumes a strict ordering in decreasing transverse momentum of the gluon branching chain. It is unclear if this is sufficient to fully describe the gluon density in the proton at very low values of x ($\mathcal{O}$ 10^{-4}). An alternative formulation, the Balitsky, Fadin, Kuraev, Lipatov (BFKL) evolution equations [13] incorporates a relaxation of this ordering and can be used to predict the evolution with x at very low x of the gluon density function over small ranges in Q^2.

3.4.3 Recent $F_2(x, Q^2)$ Measurements at H1

Structure function measurements have so far concentrated on $F_2(x, Q^2)$ derived from the one photon exchange cross section:

$$\frac{d^2\sigma(e^{\pm}p)}{dxdQ^2} = \frac{4\pi\alpha^2}{xQ^4}\left(1 - y + \frac{y^2}{2(1 + R(x, Q^2))}\right) F_2(x, Q^2) \qquad (3.18)$$

where the function $R = \frac{F_2}{2xF_1} - 1$ has yet to be measured and is predicted following QCD calculations [14]. A 20% error on R results in an uncertainty of 2% in F_2.

The 1994 statistics facilitated measurements of $F_2(x, Q^2)$ in the extended ranges of $1.5 \leq Q^2 \leq 5000$ GeV^2 and $1.8 \times 10^{-4} \leq x \leq 0.32$ [14]. See figure 3.2.

The Q^2 dependence of the total CC cross section along with that of a kinematically compatible NC sample (transverse energy $>$ 25 GeV) is shown for e^+p collisions in figure 3.3 along with standard model (F_2 and F_3) and photon exchange only (for the NC data) predictions. The effects of the inclusion of F_3 are well within the uncertainties in the data even at the highest values of Q^2 [8].

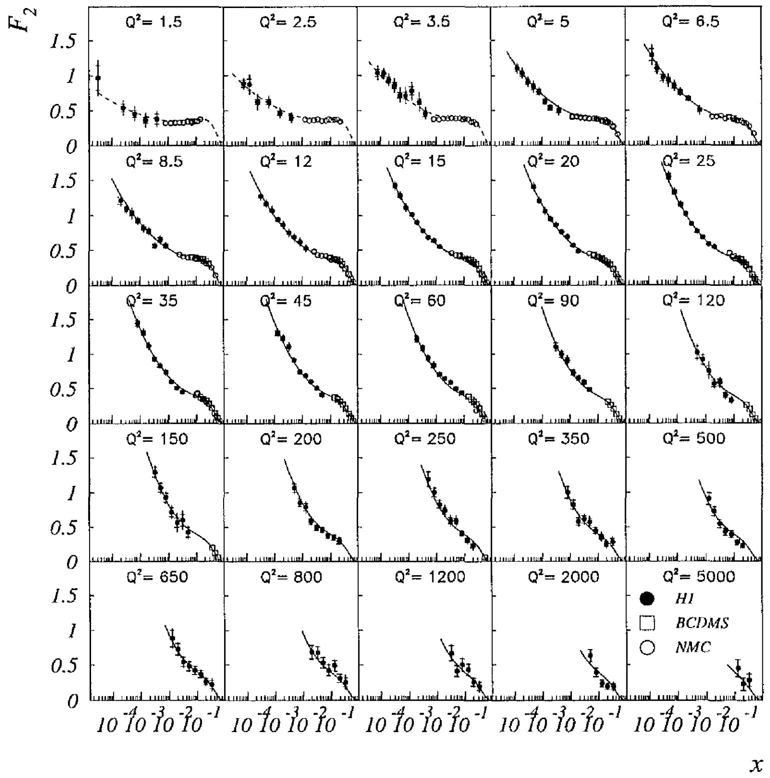

Figure 3.2: The H1 measurement of $F_2(x, Q^2)$ as a function of x. The open squares and circles represent the BCDMS and NMC data respectively. The curves a the result of a fit based on QCD evolution extended to include heavy quark contributions.

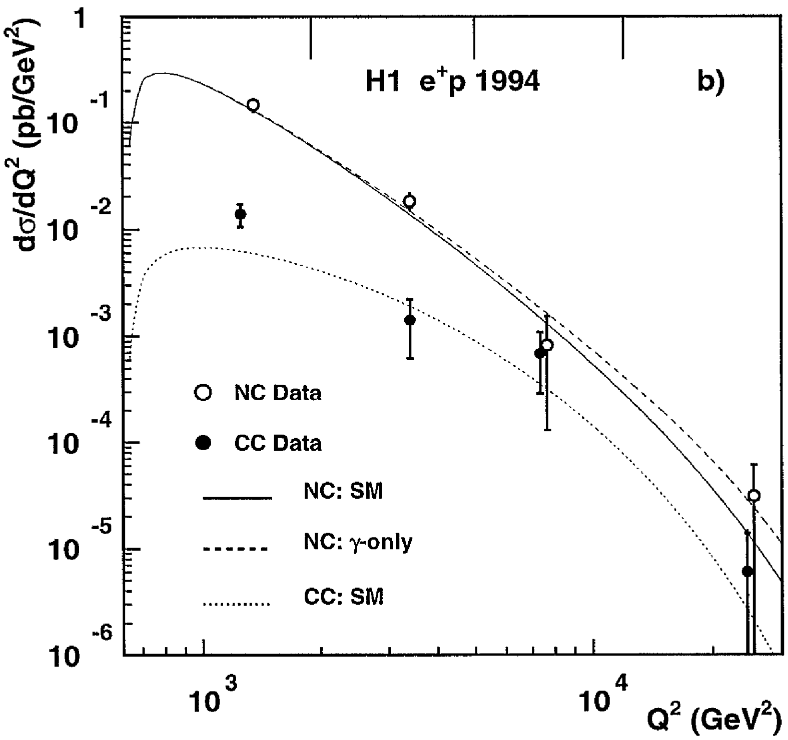

Figure 3.3: Differential cross sections for e^+p CC and NC DIS interactions with $P_t > 25$ GeV. Standard Model predictions for NC and CC samples are shown along with NC photon only exchange.

3.4.4 Radiative Corrections

The DIS cross section so far discussed is the Born cross section in which only single boson exchange is considered. Higher order QED processes, however, affect the kinematics as determined from the scattered electron such that the total *measured* cross section corresponds to:

$$\frac{d^2\sigma_{tot}}{dxdQ^2} = \frac{d^2\sigma_B}{dxdQ^2} + \frac{\alpha}{2\pi}\frac{d^2\sigma_1}{dxdQ^2} + \mathcal{O}(\alpha^2) \tag{3.19}$$

where the first term is the born cross section and the second and third refer to the radiative corrections.

The largest contribution to the these corrections is due to initial state radiation, in which the incident electron emits a real photon prior to interaction. This results in a reduction of the true centre of mass energy and a consequent increase in the reconstructed value of y from that expected given the nominal beam energies. Final state radiation, the emission of a real photon by the scattered electron, does not have such a significant effect. Generally collinear with the path of the scattered electron, the photon cannot be resolved as a separate entity by the detector.

Such radiative corrections are calculable and can be reduced by avoiding the kinematic regimes where their effects are most pronounced e.g. at very high y.

3.5 Photoproduction

Photoproduction is the dominant process in $e^{\pm}p$ scattering at HERA. In this case the scattered electron is deflected by only a small angle by the interaction. No exact boundary in Q^2 exists to discriminate between DIS and photoproduction, although photoproduction can be identified with the presence of the scattered electron in the electron tagger (see section 2.8), constraining Q^2 to be less than $\sim 10^{-2}$ GeV^2.

Division of photoproduction into two distinct classes is made according to the transverse momentum of the hadronic final state. 'Hard' processes, with high transverse momentum ($>\sim$ 1 GeV) may be treated within the perturbative QCD framework. 'Soft' processes can only be described in terms of phenomenological models, such as the Vector Meson Dominance model (VMD) [15]. Here, the photon becomes an off-shell vector meson, typically ρ, ω or ϕ, which is put on shell by a small momentum transfer from the proton.

The relevance of photoproduction to this analysis is due to its potential as a significant background source to DIS. Although suppressed at high Q^2 its high rate results in the possibility of a significant number of events migrating into the DIS sample through misidentification in the detector.

3.6 Monte Carlo Models

Monte Carlo modelling is essential for any physics analysis at HERA. Study of the effects of finite acceptance, resolution and solid angle coverage of the many components of the H1 detector requires simulation which reproduces the characteristics of the data as closely as possible.

3.6.1 DIS Models

In this analysis NC and CC DIS processes are simulated with the DJANGO [16] generator. This program is based on HERACLES [17] which simulates the electroweak interaction and LEPTO [18] which deals with the hadronic final state. HERACLES calculates the cross-section and includes first order radiative corrections and the simulation of bremsstrahlung photons. LEPTO uses the the Colour Dipole Model (CDM) as implemented in ARIADNE [19]. LEPTO offers an alternative treatment of higher order QCD corrections with MEPS (Matrix Element + Matched Parton Showers), in which all QCD corrections of $\mathcal{O}(\alpha_s)$ are included.

3.6.2 Photoproduction Models

Event samples containing hard and soft photoproduction processes are generated using the PYTHIA [20] code. This is based on leading order matrix element calculations, including parton showers and initial state radiation. The simulation is used to assess the photoproduction background levels to the DIS processes of interest in this work.

Chapter 4

Diffractive Physics at HERA

4.1 Introduction

Diffractive phenomena have been observed since the very early days of high energy collision experiments, the term arising from the similarities between the resulting patterns of particle scattering and those from optical diffraction. Successful interpretation of such events has been provided within the framework of Regge Theory, with the interaction being modelled by the exchange of a vacuum state Regge pole, the pomeron ($\mathbb{P}$).

DIS events exhibiting a significant rapidity gap in the final state, one of the characteristics of the diffractive process, were first reported at HERA in 1993 [21, 22]. Since then considerable progress has been made in the study and understanding of these events, with the confirmation of their diffractive origin and subsequent measurements of the structure of the mediating $\mathbb{P}$.

This chapter attempts to give a brief overview of the diffractive phenomenology as it pertains to DIS at HERA, with a review of the recent experimental results upon which it is largely based.

4.2 Regge Theory and the Pomeron

As discussed in the previous chapter, a perturbative treatment of long range strong forces, such as those involved in the elastic scattering of hadrons or photoproduction, is not appropriate. In such regimes, however, the phenomenological predictions of Regge Theory have proved successful.

Simple scattering processes are modelled in Regge Theory [23, 24] with the virtual exchange of bound state hadrons, which can be seen as an extension of the early scattering models developed by Yukawa. Interpretation of the characteristics of an s channel process, such as $A + B \rightarrow A + B$, is made via consideration of the mass and spin of all possible intermediate hadron states in the equivalent t channel process, $A + \overline{A} \rightarrow B + \overline{B}$ (see for example [25]). The set of these resonance states, or Regge Poles (all of which must allow the relevant quantum numbers to be conserved) are linked in spin-mass space by a 'path' known as a Regge trajectory. The energy dependence of a particular process is then ascertained from the extrapolation of this trajectory from the t channel to the s channel ($+t \rightarrow -t$). At high s and in the limit $-t \rightarrow 0$ the cross section can then be written in terms of the intercept of the Regge trajectory, $\alpha(t)$, at $t = 0$ and s:

$$\frac{d\sigma}{dt} \propto s^{2\alpha(0)-2} \tag{4.1}$$

where $\alpha(0) < 1$ for the trajectories formed by all known hadrons. This relation then implies that the cross section of an elastic process falls with increasing centre of mass energy. This prediction is contradicted, however, by experimental findings, where a slight rise in the cross section is observed at high s. This can be explained by the introduction of a Regge trajectory with an intercept of $\alpha(0) = 1 + \epsilon$, where ($1 \gg \epsilon > 0$), the poles of which have quantum numbers of the vacuum i.e. zero values. Within the Regge Theory framework the lowest mass pole which satisfies these requirements is the $\mathbb{P}$ or Pomerančuk pole.

Diffractive interactions are defined as those processes which involve $\mathbb{P}$ exchange.

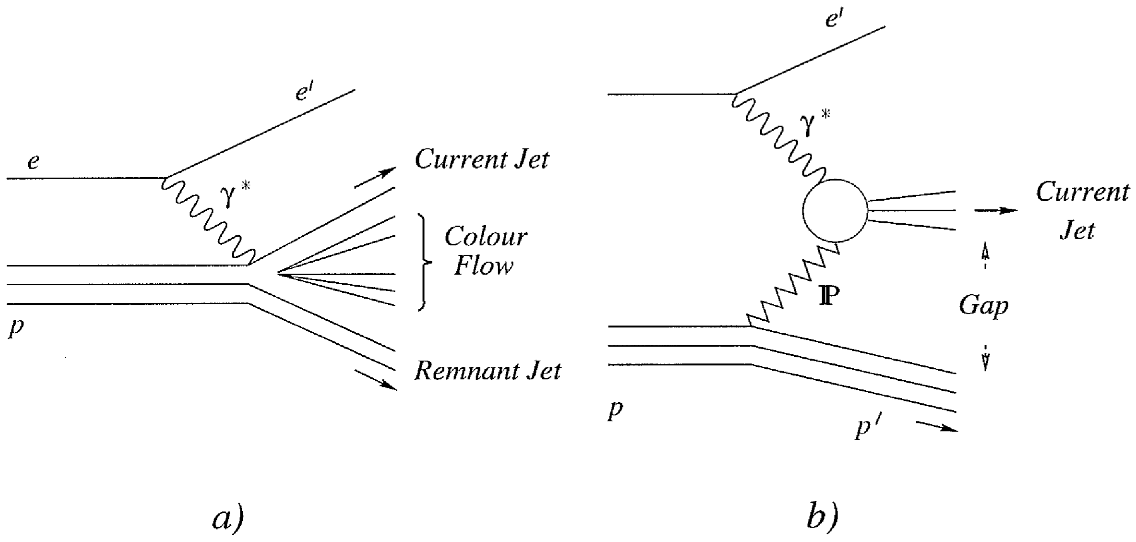

Figure 4.1: a) Standard DIS, with hadronic flow between the current and remnant jets. b) Diffractive DIS, exhibiting a *rapidity gap*.

4.3 Rapidity Gaps in Diffractive DIS

Diffractive processes are characterised by *rapidity gaps*, large regions in pseudo-rapidity, η, where there is no hadronic flow in the final state, where η is defined by:

$$\eta = -\ln \tan\left(\frac{\theta}{2}\right) \tag{4.2}$$

where θ is the polar angle of the particle in question.

Figure 4.1 (a) shows a non-diffractive, *standard*, DIS interaction. In this process the virtual photon couples to one of the coloured components of the proton, a valence quark. The colour of the proton is then *opened up* and a colour string exists between the resulting remnant and current jet. To fulfill the requirement of colour confinement condensation of the colour field must occur to fill the intervening region between the jets with hadrons. Although random fluctuations in the hadronisation process may produce regions in pseudo-rapidity devoid of particles, the production of large rapidity gaps by this mechanism is expected to be considerably suppressed.

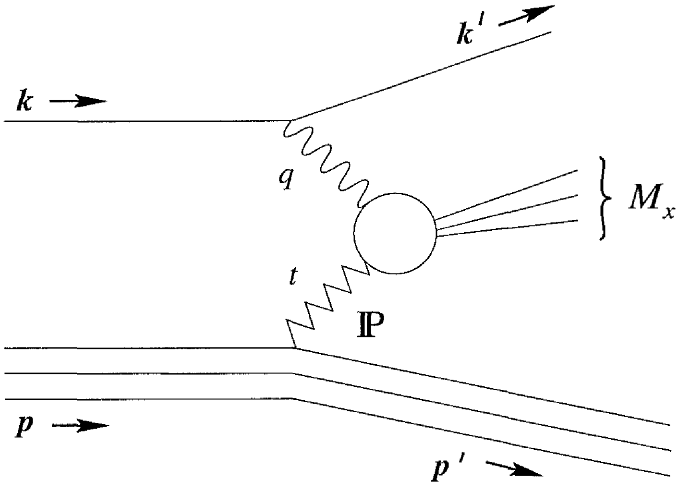

Figure 4.2: The Kinematics of Diffractive DIS

In the diffractive process, the virtual photon does not interact directly with the proton, but with the colourless $\mathbb{P}$. The proton then remains intact, or in a low-mass excited state after interaction. As there is no colour field between the current jet and the scattered proton, there is no requirement for the production of hadrons in this region resulting in a significant gap in η in which there is little or no hadronic flow. The colourless proton remnant is then either a proton of an isospin $\frac{1}{2}$ baryon excitation e.g. N^* or $N^*\pi$.

4.4 The Kinematics Of Diffractive DIS

Figure 4.2 shows the 4-vectors relevant to diffractive DIS. The presence of the rapidity gap leads to two further degrees of freedom: the energy loss and scattering angle of the proton. This means that along with the usual quantities for standard DIS, x, y, Q^2 and W, the following diffractive variables can be defined:

$$t = (P - P')^2 \tag{4.3}$$

the 4-momentum transfer at the pomeron-proton vertex;

$$x_{\mathbb{P}} = \frac{q.(P - P')}{q.P} = \frac{Q^2 + M_x^2 - t}{Q^2 + W^2 - m_p^2} \tag{4.4}$$

and

$$\beta = \frac{Q^2}{Q^2 + M_x^2 - t} \tag{4.5}$$

where M_x is the invariant mass of the hadronic final state, excluding the proton remnant. If Q^2 is large ($\gtrsim$ 1 GeV^2) and $|t|$ is small, then

$$x_{\mathbb{P}} \approx \frac{Q^2 + M_x^2}{Q^2 + W^2} \tag{4.6}$$

and

$$\beta \approx \frac{Q^2}{Q^2 + M_x^2} \tag{4.7}$$

so,

$$x_{\mathbb{P}} = \frac{x}{\beta} \tag{4.8}$$

In this regime $x_{\mathbb{P}}$ and β can be interpreted as the fraction of the proton's momentum carried by the $\mathbb{P}$ and the fraction of the $\mathbb{P}$'s momentum which enters the interaction respectively. Berger et al. [26] argue that the rapidity of any particle with mass m in the hadronic system X must obey the the following constraint:

$$\eta \geq \frac{1}{2} ln\left(\frac{m^2}{s}\right) + ln\left(\frac{1}{x_{\mathbb{P}}}\right) \tag{4.9}$$

where $\frac{1}{2} ln\left(\frac{m^2}{s}\right) = \eta_{min}$, the minimum rapidity for a particle produced in a standard DIS event. As such, the size of the rapidity gap $(\eta - \eta_{min})$ is constrained to be:

$$\Delta\eta \geq ln\left(\frac{1}{x_{\mathbb{P}}}\right) \tag{4.10}$$

4.5 The Diffractive Structure Function

Quantitative study of the structure of the diffractive mechanism in DIS is facilitated by the expression of the diffractive cross section in terms of a structure function. The *diffractive* proton structure function, a function of four variables, is defined in analogy to the standard proton structure function as:

$$\frac{d^4(ep \to epX)}{dx dQ^2 dx_{\mathbb{P}} dt} = \frac{4\pi\alpha^2}{xQ^4}\left(1 - y + \frac{y^2}{2(1+R^D)}\right) F_2^D(x, Q^2, x_{\mathbb{P}}, t) \tag{4.11}$$

where the contribution from F_3 is neglected. This definition is valid for all high Q^2 studies at the present time, with the lack of significant statistics making measurement of the diffractive cross section impossible above $Q^2 \approx 400$ GeV^2 ($\ll M_{Z^0}^2$). The parameter R^D is as yet uncalculated and is set to 0 for the remainder of this analysis.

Much of the theoretical work conducted on diffractive DIS suggests that it is possible to factorise the diffractive structure function [27, 28] into the product of two independent terms:

$$F_2^D(x, Q^2, x_{\mathbb{P}}, t) = f_{\mathbb{P}/p}(x_{\mathbb{P}}, t).F_2^{\mathbb{P}}(\beta, Q^2) \tag{4.12}$$

where $f_{\mathbb{P}/p}(x_{\mathbb{P}}, t)$ describes the flux of the $\mathbb{P}$ within the proton and $F_2^{\mathbb{P}}(\beta, Q^2)$ is the $\mathbb{P}$ structure function. The emission of the $\mathbb{P}$ from the proton and its interaction with the virtual photon can then be seen as two separate processes. The motivation behind factorisation lies in the difference between the virtuality scales governing each of the processes: the momentum scale at the proton-$\mathbb{P}$ vertex, t, is typically small ($t \ll 1$ GeV^2), rendering perturbative treatment inappropriate, in contrast the the photon-$\mathbb{P}$ vertex for which $Q^2 > 1$ GeV^2.

In the Regge picture the double differential cross section for the diffractive process $ep \to epX$ can be expressed, following 4.1, as:

$$\frac{d^2\sigma(ep \to epX)}{dM_x^2 dt} = f(M_x^2, t).(W^2)^{2\alpha(t)-2} \tag{4.13}$$

in the limit: $t/W^2 \to 0$, $M_x^2/W^2 \to 0$ and $x_{\mathbb{P}} \to 0$. The function $f(M_x^2, t)$ depends on the phase space and the t dependence, which is typically peripheral [29]. At fixed Q^2 and M_x^2, this cross section is equivalent to:

$$\frac{d^2\sigma(ep \to epX)}{dx_{\mathbb{P}}} \propto \frac{1}{x_{\mathbb{P}}^{2\alpha(t)-1}} \tag{4.14}$$

and therefore

$$f_{\mathbb{P}/p}(x_{\mathbb{P}}, t) \propto \frac{1}{x_{\mathbb{P}}^{2\alpha(t)-1}} \tag{4.15}$$

4.6 The Two Pomerons

Theoretical and experimental studies suggest that the pomeron may not be a single entity. There seem to be two pomerons:

- **The Soft Pomeron**: non-perturbative, but with well established properties based upon experimental data.
- **The Hard Pomeron**: described by the perturbative BFKL evolution equations, but is as yet supported by little data.

4.6.1 Soft Pomeron Models

Factorisation is assumed by most diffractive DIS models, which parameterise the non-perturbative component of the structure function, $f_{\mathbb{P}/p}(x_{\mathbb{P}}, t)$, with Regge fits to photoproduction and $p\overline{p}$ data.

The model proposed by Donnachie and Landshoff [30] is based upon Regge Theory with an isoscalar form factor for the proton as measured from eN scattering [31], from which they obtain:

$$f_{\mathbb{P}/p}(x_{\mathbb{P}}, t) = \left(3.5\frac{9}{4\pi^2}\right) \cdot \left(\frac{4m_p^2 - 2.8t}{4m_p^2 - t}\right) \cdot \left(\frac{1}{(1-\frac{t}{0.7})^2}\right) \cdot \left(\frac{1}{x_{\mathbb{P}}^{2\alpha(t)-1}}\right) \tag{4.16}$$

where $\alpha(t) = \alpha(0) + \alpha' t = 1 + \epsilon + 0.25t$ with $\epsilon = 0.085$. ϵ is obtained from fits to the gradually rising cross section in $p\overline{p}$ and a value of $\lesssim 0.1$ is the signature for soft $\mathbb{P}$ exchange [31]. Berger et al. [26] and Streng [28] suggest:

$$f_{\mathbb{P}/p}(x_{\mathbb{P}}, t) = \frac{100}{16\pi} . e^{4.7/2|t|} . \left(\frac{1}{x_{\mathbb{P}}^{2\alpha(t)-1}}\right) \tag{4.17}$$

Taking fits from data in order to obtain the $x_{\mathbb{P}}$ and t dependencies and applying Regge Theory only to obtain the normalisation factors Ingelman and Schlein [32] propose a similar dependency of $f_{\mathbb{P}/p}(x_{\mathbb{P}}, t) \propto x_{\mathbb{P}}^{\sim -1}$.

4.6.2 The Hard BFKL Pomeron

The BFKL equations are solved by considering the branching chain of a two gluon system [13], which when considered in the framework of colourless diffractive exchanges, constitutes an object with similar properties to the IP (see figure 4.3). This is known as the BFKL or hard IP. BFKL calculations of qq diffraction in which an infinite number of gluon branches are considered, yield a Regge asymptotic form with $\alpha(0) = 1 + N$, where N is described by:

$$N = \frac{12\alpha_s}{\pi} log2 \approx 0.5 \tag{4.18}$$

Details of this evaluation can be found in [31, 33, 34]. Indication of a contribution from hard IP exchange would thus be provided by an increase in the intercept from that expected for the soft IP. How both pomerons relate to each other is, however, far from certain. Collins and Landshoff [35] suggest that the two pomerons should be added, their relative contributions varying with the effective Q^2, but far more experimental data is required for a clear understanding of this process.

4.7 Pomeron Structure Models

A partonic, and more particularly gluonic, structure is assumed by most IP models. Such an interpretation of a factorisable IP implies that $F_2^{\mathbb{P}}(\beta, Q^2)$ is related to the IP parton density functions, $f_i(\beta, Q^2)$ (quarks) and $g_i(\beta, Q^2)$ (gluons), by:

$$F_2^{\mathbb{P}}(\beta, Q^2) = \sum_i^{all\ quarks} e_i^2 \beta f_i(\beta, Q^2) \tag{4.19}$$

It is however far from clear whether the partons in the IP fulfill the momentum sum rule:

$$\int_0^1 zF(z) + \int_0^1 zG(z) = 1 \tag{4.20}$$

where $z = x_{i/\mathbb{P}}$, the momentum fraction of the IP carried by the parton i and $G(z)$ and $F(z)$ are defined as:

$$G(z) = \sum_i^{all\ gluons} g_i(z) \tag{4.21}$$

and

$$F(z) = \sum_i^{all\ quarks} f_i(z) \tag{4.22}$$

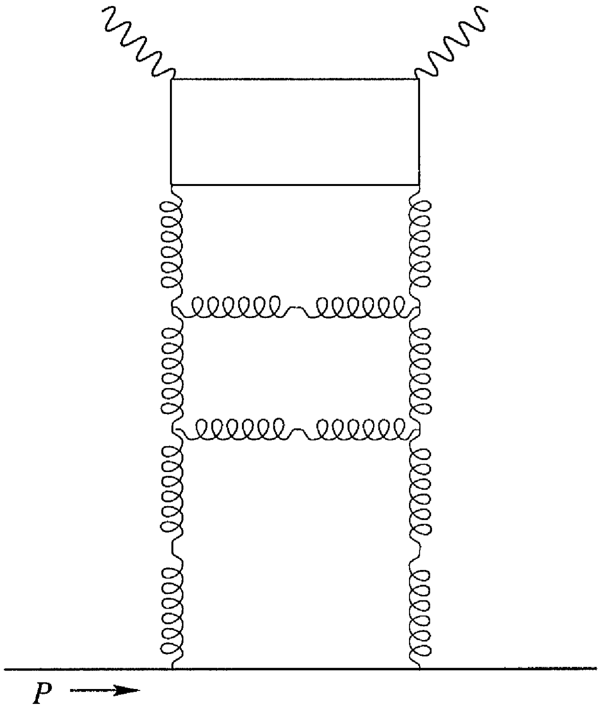

Figure 4.3: The BFKL two gluon ladder.

Having specified the parton density functions at some low value of Q^2 all models use a perturbative QCD treatment to predict the behaviour as Q^2 increases. The hardest possible gluonic distribution which obeys the momentum sum rule is that for a $\mathbb{P}$ containing two gluons, with the form:

$$zG(z) = 6z(1-z) \tag{4.23}$$

The addition of further gluons would produce a softer (lower average gluon momentum) distribution. Streng [28] proposes that this could be as soft as the gluon sea in a nucleon:

$$zG(z) = 6z(1-z)^5 \tag{4.24}$$

Donnachie and Landshoff [30] consider the $\mathbb{P}$ structure to be dominated by quarks, and, with a normalisation obtained from the proton quark densities, propose a distribution of the form:

$$zF(z) = \frac{5}{3}C\pi z(1-z) \tag{4.25}$$

where $C = 0.23$ and the distribution is summed over the first three quark and antiquark flavours, with $s\bar{s}$ contributing only a half that from $u\bar{u}$ and $d\bar{d}$. A further gluonic component is also present, with a dependence on t, resulting in the breaking of factorisation at values of $z \lesssim 0.1$. The possibility of multiple $\mathbb{P}$ exchange is not excluded, and is expected to have an increased contribution as s increases [31]. This also results in a breaking of factorisation, though at present energies the effect is expected to be small.

Genovese et al. [36] also postulate violations of factorisation via consideration of the BFKL $\mathbb{P}$. They suggest that the $\mathbb{P}$ can be approximated by a two-component structure, each endowed with a different flux factor. These correspond to a valence quark component and a component formed from the quark/gluon sea, the flux associated with the latter having a faster rise with $\frac{1}{x_{\mathbb{P}}}$.

4.8 Direct processes

Direct processes involve the diffractive production of light vector mesons: $\rho(770), \omega(783)$ and $\phi(1020)$. This is a diffractive version of the VMD, in which the virtual photon fluctuates into an off-mass shell meson state which subsequently scatters of the $\mathbb{P}$. In such an interaction, the $\mathbb{P}$ interacts as a point-like particle i.e. no inner structure is resolved, resulting in values of $\beta \approx 1$ and $M_x \approx 0$ for the final state. As well as producing a peak in the M_x distribution of diffractive events, VMD processes are also characterised by a scattered electron and only two oppositely charged tracks in the LAr calorimeter resulting from the decay of the meson states.

4.9 Pion Exchange

A schematic view of the pion exchange process is shown in figure 4.4. Such models have proved successful in describing high energy neutron and Δ^{++} production arising from pp collisions [37]. Holtmann et al [38] have extended this framework to include $e^{\pm}p$ DIS collisions and propose that pion exchange will dominate over $\mathbb{P}$ exchange in the region $0.2 \lesssim x_{\mathbb{P}} \lesssim 0.3$. The rapidity gaps produced by such

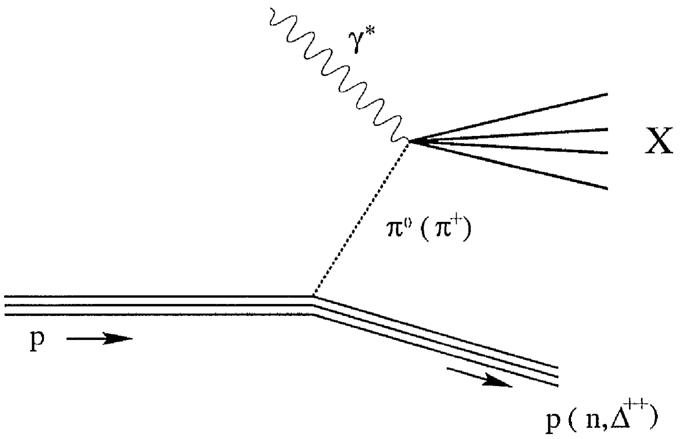

Figure 4.4: Representation of pion exchange

events are expected to be small ($\eta \gtrsim ln(1/x_{\mathbb{P}})$) and thus the majority of events can effectively be discriminated from diffractive $\mathbb{P}$ interactions.

As yet no measurement of the pion exchange cross section has been made at HERA, although the inclusion of a forward neutron tagger in the ZEUS experiment will facilitate future estimates for the rate of this process.

4.10 Measurements of F_2^D at H1

Measurement of the full diffractive structure function, $F_2^D(x, Q^2, x_{\mathbb{P}}, t)$ is not as yet possible at H1, as no measurement of t can be made due to the absence of any apparatus which can detect the elastically scattered proton or its decay products should it undergo dissociation. Inference of the proton's momentum from the hadronic final state and the scattered electron elicits virtually no information about t since the energy loss of the proton is typically far less than the energy resolution of the detector. Therefore the measured cross-section is restricted to:

$$\frac{d^3\sigma(ep \to epX)}{dxdQ^2dx_{\mathbb{P}}} = \int \frac{d^4\sigma(ep \to epX)}{dxdQ^2dx_{\mathbb{P}}dt}dt \tag{4.26}$$

from which the structure function $F_2^D(\beta, x_{\mathbb{P}}, Q^2) \equiv \int F_2^D(x, Q^2, x_{\mathbb{P}}, t)dt$ is obtained, where

$$\frac{d^3\sigma(ep \to epX)}{dxdQ^2dx_{\mathbb{P}}} = \frac{4\pi\alpha^2}{xQ^4}\left(1 - y + \frac{y^2}{2}\right) F_2^D(\beta, x_{\mathbb{P}}, Q^2) \tag{4.27}$$

or, equivalently

$$\frac{d^3\sigma(ep \to epX)}{dxdQ^2d\beta} = \frac{4\pi\alpha^2}{\beta^2Q^4}\left(1 - y + \frac{y^2}{2}\right) F_2^D(\beta, x_{\mathbb{P}}, Q^2) \tag{4.28}$$

A sample of some 1700 putative diffractive events, exhibiting a large rapidity gap[1] were selected from the 1993 data ($\mathcal{L} = 271 \pm 14$ nb^{-1}), representing ~ 10% of the total DIS sample [39]. Measurement of $F_2^D(\beta, x_{\mathbb{P}}, Q^2)$ was made over the range of $3 \times 10^{-4} \leq x_{\mathbb{P}} \leq 0.05$ for which the momentum transfer variable t is constrained to $|t| \lesssim 7$ GeV^2 [29]. A monotonic decrease in $F_2^D(\beta, x_{\mathbb{P}}, Q^2)$ with increasing $x_{\mathbb{P}}$ was observed, irrespective of β or Q^2, in the ranges of $0.065 \leq \beta \leq 0.65$ and $8.5 \leq Q^2 \leq 50$ GeV^2, to which an excellent fit was made with the assumed polynomial dependence of $x_{\mathbb{P}}^{-n}$. The single exponent was calculated to be $n = 1.19 \pm 0.06_{(stat)} \pm 0.07_{(syst)}$.

The universal dependence on $x_{\mathbb{P}}$ corresponds to $\alpha(0) = 1.10 \pm 0.03_{(stat)} \pm 0.04_{(syst)}$, and is therefore consistent with a leading trajectory describing hadronic diffraction with the exchange of a soft $\mathbb{P}$. This excludes the possibility that the rapidity gap events are due to meson exchange: the leading Regge trajectories for processes involving the isospin exchange of a $\rho(770)$ or the exchange of $\omega(783)$ with no isospin are expected to have a Regge intercept at $\alpha(0) \sim 0.5$, giving rise to an almost flat dependence on $x_{\mathbb{P}}$. For the process of pion exchange [38] parameterisations predict $\alpha(0) \sim 0$. Thus, the rapidity gap phenomenon at HERA can be unambiguously attributed to diffractive scattering. The total contribution from VMD diffractive process was estimated to be up to ~ 10% of the diffractive sample.

Combining all statistical and systematic errors the value of $\alpha(0)$ cannot exceed 1.25. If the assumption is made that the t dependence follows that for soft pp collisions ($\propto e^{bt}$, where $b \gg 1$) then the effects of its inclusion in the F_2^D calculation could raise this upper limit by no more than 0.05. This does not then rule out the possibility of a contribution from the hard BFKL $\mathbb{P}$. Cleaner signals for the existence of the hard $\mathbb{P}$ have come from diffractive heavy meson (J/ψ)

---

[1] characterised by little or no energy flow in the region of the forward detectors.

production at HERA, where a rise in the cross section with s faster than that from a soft $\mathbb{P}$ prediction has been observed [33, 40].

4.10.1 The Partonic Structure of the Pomeron

With evidence for a simple factorisation of $F_2^D(\beta, Q^2, x_{\mathbb{P}})$ its dependence on β and Q^2 can be seen as a measure of the deep-inelastic structure of the $\mathbb{P}$. This can be expressed as the integral of F_2^D over $x_{\mathbb{P}}$:

$$\tilde{F}_2^D(\beta, Q^2) = \int_{x_{\mathbb{P}}=3\times10^{-4}}^{x_{\mathbb{P}}=0.05} F_2^D(\beta, Q^2, x_{\mathbb{P}})dx_{\mathbb{P}} \tag{4.29}$$

The β and Q^2 dependences of which are shown in figure 4.5. $\tilde{F}_2^D(\beta, Q^2)$ exhibits no substantial dependence on Q^2 for all available β, leading to the conclusion that diffractive interactions are broadly of a scale invariant and, therefore, of a point-like nature. There is also little variation with β, which implies that the structure resolved in a diffractive DIS interaction carries only a fraction of the momentum of the $\mathbb{P}$; providing evidence for the $\mathbb{P}$ having its own, presumably partonic, sub-structure. The data also rules out the soft dependence $(1-\beta)^5$ as described in section 4.7.

Within the accuracy of the 1993 measurements, the possibility of scaling violations cannot be excluded. A good description of $\tilde{F}_2^D(\beta, Q^2)$ is provided by a $logQ^2$ dependence for all β. This is in contrast to the proton case, where F_2 is observed to rise with Q^2 at low x, but to fall at $x \gtrsim 0.015$. The proton dependence is an inevitable consequence of a structure built from the evolution of valence quarks. By contrast, the parton density of the $\mathbb{P}$ is likely to be dominated by a gluonic component.

QCD studies of the $\mathbb{P}$ structure have been performed [41], in which the assumed parton density $z^a(1-z)^b$ at $Q_0^2 = 4$ GeV^2 is evolved following the Altarelli-Parisi equations to higher Q^2. The measurements favoured a high gluonic content, with the suggestion that the majority of the $\mathbb{P}$'s momentum is carried by a single, or *leading* gluon [29].

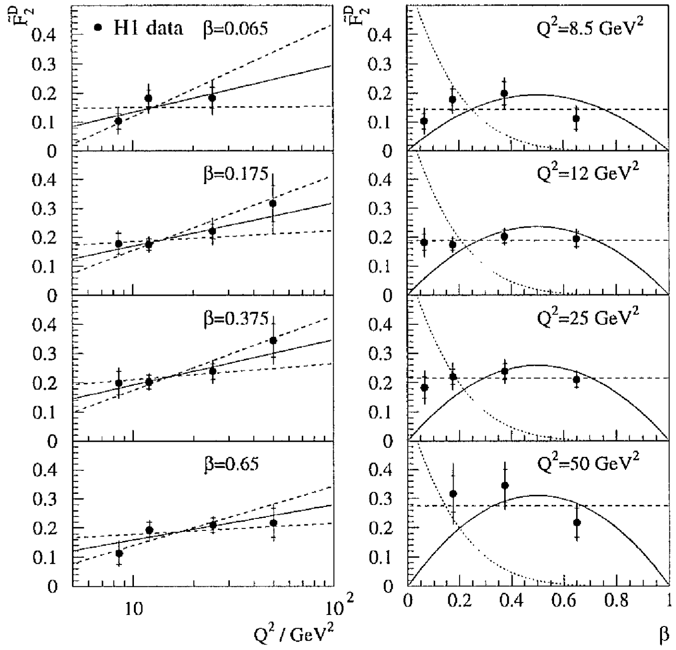

Figure 4.5: Dependence of $\tilde{F}_2^D(\beta, Q^2)$ on β and Q^2 as measured from the 1993 diffractive sample. The continuous curve in the left-hand side plots represents the best fit to the data assuming scaling violations with a $logQ^2$ dependence. The dashed curves correspond to ±1 standard deviation. Superimposed on the β dependence plots are: a hard distribution ($\beta(1-\beta)$), a soft distribution ($(1-\beta)^5$) and a constant dependence, corresponding to the continuous, dotted and dashed lines respectively.

4.11 Diffractive Monte Carlo Models

The RAPGAP program [42] is used to simulate DIS diffractive interactions. Single $\mathbb{P}$ exchange only is considered, with the inclusion of matrix element calculations for both quark and gluon initiated processes. Higher order gluon emission is included with CDM, implemented as for the LEPTO standard DIS program by

ARIADNE [19].

The $\mathbb{P}$ is taken as a partonic object with user a defined structure function and flux factor, here based on fits to the 1994 low Q^2 data [43], with the Streng flux parameterisation (equation 4.17), for which $\alpha(0) = 1 + 0.085$. QCD evolution and the effects of QED radiation are fully considered with the HERACLES program and subsequent hadronisation is performed by JETSET. There is as yet no facility for non-factorisable $\mathbb{P}$ models.

RAPGAP is also used to generate pion exchange processes with full QCD evolution and QED corrections as above.

Direct processes are modelled by the DIFVM program [44]. An admixture of vector meson states, specified by fits to previous $p\bar{p}$ and photoproduction data, is produced which then scatter off a point-like $\mathbb{P}$. Again QCD evolution and QED radiative effects are included.

Chapter 5

Selection of High Q^2 DIS Events

5.1 Introduction

High Q^2 DIS events ($Q^2 \gtrsim 100$ GeV) are defined as those in which the scattered electron is located in the LAr calorimeter, at $\theta < 150°$. Events where the electron is detected in the BEMC belong to the low Q^2 sample. The DIS cross section varies approximately as y/Q^6, resulting in considerably reduced statistics at high Q^2. The regime of intermediate Q^2 is particularly challenging due to the technical aspects of the H1 detector. In this case the electron is scattered in the BEMC-BBE crack region. The Q^2 values for such events range are typically of the order of 100 Gev, but can extend to 200 GeV, making the inclusion of this problematic region important for this analysis.

Only data taken during the running periods when the complete calorimetry system and the BPC, CJC, FMD and ToF were in full operation are considered. A total luminosity of 6 pb^{-1} was delivered by HERA in 1994, corresponding to 5 pb^{-1} during e^+p runs and 1 pb^{-1} during the running with e^-p, 3.9 pb^{-1} of which was used by H1 for physics analysis. After on and off-line selection this corresponds to an integrated luminosity of 1.966 pb^{-1}, an order of magnitude greater than that in 1993.

5.2 Background Sources

The location and identification of the electromagnetic cluster produced by the scattered electron in the LAr barrel is central to the selection of the data. Consequently, the rejection of those processes which could produce spurious electron candidates is crucial.

Photoproduction can be such a background source if the scattered electron, which escapes the detector along the beam pipe ($\theta_e \approx 180°$), remains untagged and the energy cluster from the hadronic final state fakes an electron [45]. The exceptionally high cross-section for photoproduction ensures that this is a significant effect [46].

At high Q^2 the main non-*ep* background is due to cosmic ray and beam halo events. Beam halo is a term used to describe the cloud of particles resulting from beam wall interactions. The *halo* consists mainly of muons from the decay of pions, products of the proton wall impact, and concentrates around the beam pipe. The muons travel off axis parallel to the beam with the same velocity as the proton bunch and constitute a major source of false triggers.

It is possible for a proton beam-gas collision to produce an energetic cluster in the LAr calorimeter. As with *ep* beam-beam collisions the dominant mechanism is expected to be photoproduction. However, as the collision involves an effectively stationary proton, the available centre of mass energy is considerably less and as such so is the rate and its significance as a background source.

5.3 Reconstruction of Kinematic Variables

At H1, unlike fixed target experiments, both the scattered electron vector (k') and the hadronic final state (P') are well measured. This allows the kinematic variables of the inclusive scattering process $ep \rightarrow eX$ to be reconstructed in different ways: from the hadronic system, the electron or a combination of both. The choice of reconstruction method for x, y and Q^2 determines the size of the systematic errors, the acceptance and the radiative corrections.

Four methods are described here: the electron only, the hadronic only, the Σ and the Double-Angle (DA) methods.

For the electron method conversion of equations 3.4, 3.5 and 3.6 into the laboratory frame leads to:

$$y_e = 1 - \frac{E'}{E}\sin^2\frac{\theta_e}{2} \tag{5.1}$$

$$Q_e^2 = 4E'E\cos^2\frac{\theta_e}{2} = \frac{E'^2\sin^2\theta_e}{1-y_e} \tag{5.2}$$

and

$$x_e = \frac{Q_e^2}{sy_e} \tag{5.3}$$

where E is the energy of the incident electron, E' that of the scattered electron and θ_e the scattered electron angle.

The resolution in Q^2 is $\sim 5\%$. The precision of the y_e measurement falls as $1/y_e$:

$$\frac{\sigma(y_e)}{y_e} \approx \frac{d\sigma(E')}{E'y_e} \tag{5.4}$$

This limits the use of the electron method to $y_e > 0.05$. At high y_e the effects of large initial state radiation make measurements difficult imposing an upper limit on y_e of 0.6. [47].

It is possible, however, to reconstruct the kinematics in the low y region using the hadronic or *Jacquet-Blondel* method [48]. The variables are then given as:

$$y_h = \frac{1}{2E}\sum_i(E_i - P_{z,i}) = \frac{\Sigma}{2E} \tag{5.5}$$

$$Q_h^2 = \frac{1}{1-y_h}((\sum_i P_{x,i})^2 + (\sum_i P_{y,i})^2) \tag{5.6}$$

where the summation extends over all hadronic final state particles. The effects due to particle losses in the forward direction are minimised since as θ tends to zero both the transverse momentum and $E - P_z$ are small. However, losses in the backward direction, for which $E - P_z$ is large, result in a considerable deterioration in resolution at high values of y_h. The resolution in Q_h^2 is worse than that for Q_e^2 over the entire Q^2 range.

The Σ method of reconstruction [49], which combines scattered electron information with that from the hadronic final state, provides improved resolution in y at low values and reduces the effects of initial state radiation. In the case of the initial state radiation of a photon collinear with the incident electron the term $2E$ in the denominator of equation 5.5 can be written:

$$2E = \sum_{all}(E - P_z) = \Sigma + E'(1 - \cos\frac{\theta_e}{2}) + 2E_\gamma \tag{5.7}$$

through conservation of energy and longitudinal momentum, where E_γ is the energy of the radiated photon. Generally in this scenario, the photon is lost down the backward beam pipe, so the 'true' energy of the electron just before its interaction with the proton is nearer to the reconstructed quantity E_Σ, where

$$E_\Sigma = \Sigma + E'(1 - \cos\frac{\theta_e}{2}) \tag{5.8}$$

Replacing E by E_Σ the kinematic variables become:

$$y_\Sigma = \frac{\Sigma}{\Sigma + E'(1 - \cos\frac{\theta_e}{2})} \tag{5.9}$$

$$Q^2_\Sigma = \frac{E'^2 \sin^2\theta_e}{1 - y_\Sigma} \tag{5.10}$$

$$x_\Sigma = \frac{E'\cos\frac{\theta_e}{2}}{P y_\Sigma} \tag{5.11}$$

The resolution of y_Σ is good even at low values as it now appears in the numerator of the equation

$$\frac{\sigma(y_e)}{y_e} \approx y_\Sigma \frac{d\sigma(E')}{\Sigma} \tag{5.12}$$

The y range in which reasonable measurements can be made can then be increased to $0.01 < y_\Sigma < 0.7$. The upper limit is imposed to reduce photoproduction background [45]. Also, inclusion of the effects of initial state radiation results in a substantial reduction in radiative corrections from up to $\sim 20\%$ for the electron method to $\sim 3\%$ in the Σ case.

The DA method [50, 51] makes use of only θ_e and angle of the current jet, θ_h, defined in the hadronic formulation as:

$$\tan\frac{\theta_h}{2} = \frac{\Sigma}{P_t^h} \tag{5.13}$$

For this method the kinematic definitions are:

$$y_{DA} = \frac{\tan(\frac{\theta_h}{2})}{\tan(\frac{\theta_e}{2}) + \tan(\frac{\theta_h}{2})} = \frac{\sin\theta_e(1-\cos\theta_h)}{\sin\theta_h + \sin\theta_e - \sin(\theta_e+\theta_h)} \tag{5.14}$$

and,

$$Q^2_{DA} = 4E_e^2 \frac{\cot(\frac{\theta_e}{2})}{\tan(\frac{\theta_e}{2}) + \tan(\frac{\theta_h}{2})} = 4E_e^2 \frac{\sin\theta_h(1+\cos\theta_e)}{\sin\theta_h + \sin\theta_e - \sin(\theta_e+\theta_h)} \tag{5.15}$$

This method provides good resolution at high Q^2 [51] and is largely insensitive to the absolute energy calibration of the detector. At values of $x < 0.001$ the resolution deteriorates making it less suitable for low Q^2 analysis.

5.4 The High Q^2 Selection Procedure

The high Q^2 events are triggered at L1 by an electromagnetic energy cluster in the LAr barrel above a threshold of 6 GeV, which is not vetoed by the ToF system [46]. At L5 reconstructed events with a potential scattered electron in the forward region are placed in the class 9 POT data sample. The details of this selection are given below. The selection criteria used to extract the genuine events from this sample can be divided into 4 categories:

i. Electron identification.

ii. Event vertex requirement.

iii. Kinematic constraints.

iv. Non-*ep* background removal.

These are applied in two steps: a selection to produce a miniPOT data set and a final selection involving either the Σ or DA reconstruction methods.

5.4.1 The Class 9 POT Selection

This class contains events with an electron candidate in the LAr barrel and the forward region. The candidate is defined at this stage as a reconstructed energy cluster, with an electromagnetic fraction > 0.5.

The energy, E, and the transverse energy, E_t, as calculated from the energy sum of the cells in the cluster, must satisfy the requirements of:

$E > 0$ GeV and $E_t > 8$ GeV if the candidate is reconstructed in the region $10^\circ < \theta_e < 45^\circ$,

or

$E > 0$ GeV and $E_t > 5$ GeV if the candidate is reconstructed in the region $45^\circ < \theta_e < 160^\circ$.

In addition the missing transverse momentum, V, calculated from the cells over the entire polar region $4^\circ < \theta < 173^\circ$, is required to be less than 40 GeV.

5.4.2 The MiniPOT Selection

Far tighter criteria are imposed for the identification of the scattered electron in the LAr calorimeter, producing an event sample of manageable size upon which various different analyses can be performed.

An algorithm is used which takes the cluster with the highest electromagnetic transverse energy as the electron candidate. A cylinder of radius 15 cm is then taken around the track or the centre of the cluster and a 4-vector for the candidate is created by summing over the energy deposited in the cells of the electromagnetic calorimeter and the first layer of the hadronic calorimeter which lie within.

The candidate must satisfy the following requirements:

- Isolation - the total energy deposited in the region between the 15cm cylinder and an outer cylinder of radius 30 cm is less than 1.2 GeV.
- The hadronic energy deposited behind the electron candidate cluster within the wider 30 cm cylinder is less than 0.5 GeV.
- The *cluster estimator* EAH4 > 0.5 - where EAH4 is the ratio of the energy in the 4 neighbouring highest energy cells in the cluster to the energy of the cluster as a whole [52].

- The electromagnetic estimator EAEM > 0.8 - where EAEM is the ratio of the energy deposited in the electromagnetic part of the cluster to the total cluster energy.
- EAK0 $\neq 0$ or 1 - where EAK0 is the ratio of the energy of the cluster deposited in the first layer of the electromagnetic part of the calorimeter to the total energy.

No demand on the absolute energy of the electron candidate is made at this stage. These cuts result in a miniPOT sample of approximately 32000 events.

5.5 The Final Selection

A significant contribution from background processes still remains in the miniPOT sample. A final selection is required to ensure that the data sample, upon which physics analysis is to be performed, is as pure as possible.

5.5.1 Event Vertex Requirement

A substantial number of non-*ep* background events are removed by demanding a well reconstructed event vertex. The vertex position is also required for precise measurement of the event kinematics. A restriction on the z position of the vertex of -35 cm $<$ ZVTX $<$ 25 cm from the nominal interaction point is made. This is consistent with the spread in the vertex due to the length of the proton bunch and the asymmetric nature of the cut takes into account the offset shown in figure 5.1.

5.5.2 Kinematic Constraints

To ensure that the reconstructed electron candidate is well within the LAr barrel and away from the problematic BEMC-BBE transition region, a cut is made of $\theta_e < 150^\circ$. A demand on the scattered electron candidate's energy of $E_e' > 8$ GeV,

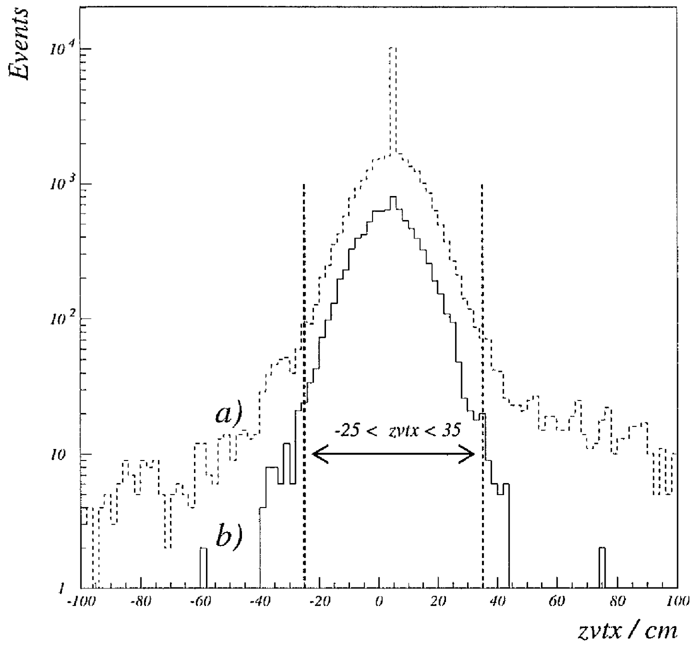

Figure 5.1: The position in z of the reconstructed event vertex for: a) the miniPOT sample and b) the final selection excluding the z vertex requirement. The allowed range in z is indicated by the dashed vertical lines.

is also made to verify the miniPOT selection, reduce photoproduction background and ensure a high trigger efficiency. A vertex constrained track linked to the electron candidate cluster is also required. A link is established with a track extrapolated from the central region which has the shortest Distance of Closest Approach (DCA) to the cluster and which satisfies the following requirements:

- Vertex reconstructed from the CTD:
    - ≥ 4 hits in the CTD.
    - DCA from the nominal $r - \phi$ interaction point < 5 cm.
    - $|Z_{DCA} - Z_0| \leq 5$ cm - the DCA in z of the track to the nominal interaction point [53].

- $TC_{DCA} < 25$ cm - the maximum DCA between the extrapolated track and the c.o.g of the cluster.
- Track Momentum $P_{track} > 4$ GeV

As discussed in section 5.3, the limit $y < 0.7$ is imposed for both reconstruction methods. Such a restriction ensures that the data is in a range where y is well reconstructed and does not suffer from large radiative corrections and photoproduction background.

Energy and momentum conservation ensures that the total $E - P_z$ and the total transverse momentum, P_T, must be conserved in any interaction. A marked difference is seen in the $E - P_z$ distributions of DIS and photoproduction events. With the scattered electron lost along the beam pipe the same conservation rules imply that the longitudinal momentum in the remainder of a photoproduction event is greater than that for DIS. See figures 5.2 and 5.3. The distribution in DIS is affected by radiative events in which a real photon is emitted from the electron before the interaction, as the photon generally escapes detection, resulting in the low energy tail shown in figure 5.3. A cut of $E - P_z > 30$ GeV is thus introduced to reduce the influence of this initial state radiation and to produce further reductions in the level of photoproduction contamination. An upper-limit of $E - P_z < 70$ GeV rejects 'huge' events due to showers occurring outside the detector initiated either by cosmic rays or by lost beam particles.

For P_T measurements the main problem is the loss of hadronic final state particles in the forward beam pipe. This leads to a (relatively loose) cut on the missing transverse momentum: $V < 15$ GeV. This is especially useful in high Q^2 DIS since it rejects much of the non-*ep* background from beam halo and cosmic rays which leave large electromagnetic clusters in only one part of the detector. As will be seen in chapter 6, the demand for a missing transverse momentum signature in the selection of CC events results in considerable background from such non-*ep* sources. This cut retains > 99% of the real DIS data [46]. Greater reduction of beam halo events is achieved with a limit imposed on the electron-hadron P_T balance of $P_T^h / E_e' \sin(\theta_e) > 0.4$.

Removal of residual cosmic and beam halo background is facilitated with the application of the cosmic/halo finding algorithms based on topological criteria

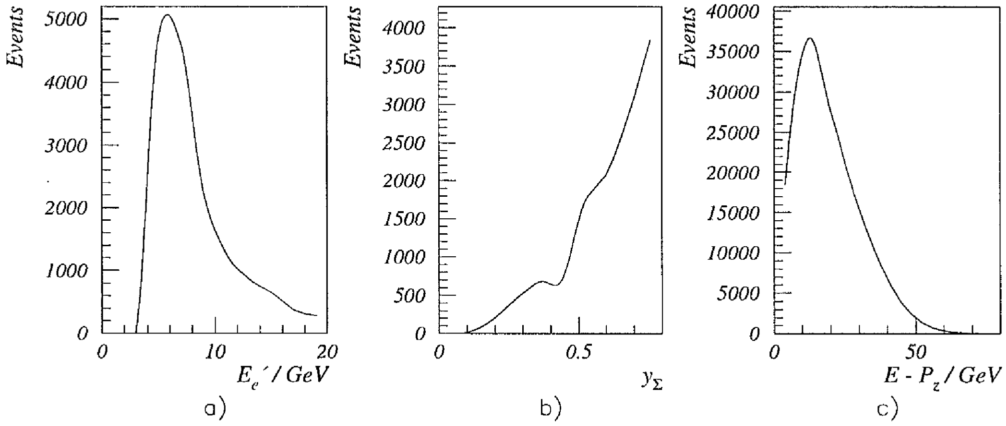

Figure 5.2: Distributions for PYTHIA generated untagged photoproduction events: a) Energy distribution of the 'fake' electron, b) y reconstructed using the Σ method and c) the $E - P_z$ distribution.

described in section 6.3.1. These reject $\sim$ 1.5% and $\sim$ 1.8% of the samples so far selected using the Σ and DA methods respectively. These also allow an estimate of the remaining non-ep contamination to be made of $\lesssim$ 1%. Independent studies with pilot bunch data suggest a similar background fraction from beam related sources [14].

Events due to QED compton scattering, where the radiated photon converts and is misidentified as the scattered electron are also a source of contamination. These are effectively removed with a constraint placed on the number of objects used to calculate the invariant mass of the event, M_x (excluding the electron and proton remnant) of $N^+_{track} + N^-_{track} + N_{clusters} > 2$ - where $N_{clusters}$ represents the number of clusters contributing to the total M_x and $N^{\pm}_{track}$ represents the number of positive or negative tracks associated with the clusters. This cut also has the effect of reducing photoproduction events.

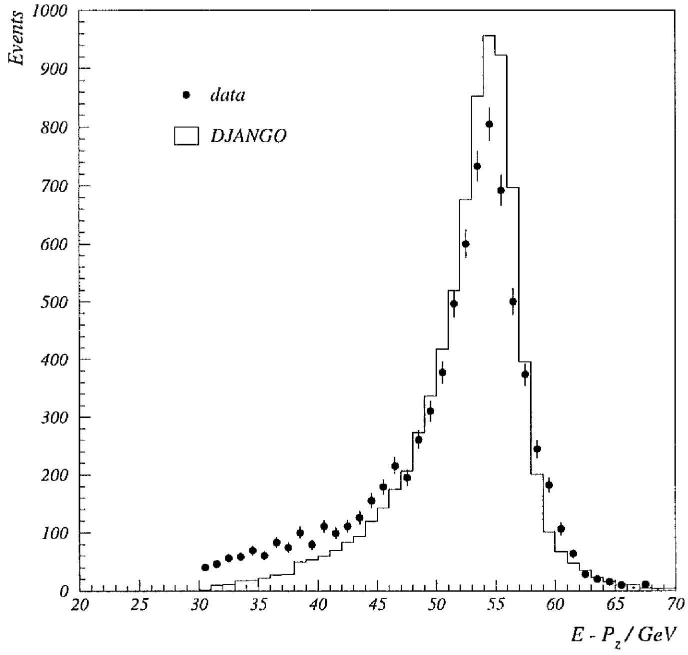

Figure 5.3: Distribution of $E - P_z$ for the final DIS sample.

5.5.3 Estimation of the Remaining Photoproduction Background

The presence of an energy deposit in the electron tagger does not automatically signify a photoproduction event. This can also result from the time-overlay of a genuine DIS event with a Bethe-Heitler process, with the electron from the latter being tagged. For such an event it is expected that a photon would be detected by the photon tagger and that the value of $E - P_z$ is consistent with two *ep*-collisions [45]. The following criteria are thus used to anti-select tagged photoproduction events:

- $E_{etag} > 8$ GeV
- $E_{\gamma tag} < 2$ GeV

- $E - P_z < 60$ GeV

To estimate the remainder, tagged and untagged photoproduction events were simulated using the PYTHIA program. Both hard and soft photoproduction processes are included in the simulation and the events are normalised to the luminosity of the data. After inclusion of all the cuts detailed above, no further tagged events were predicted and the remaining contribution from untagged photoproduction in the data selected using both the Σ and DA methods is estimated to be as little as $0.1 \pm 0.1\%$. The 100% error is attributable to the uncertainty in the ratio of tagged to untagged events [45, 54].

A total number of 5756 (6059) events reconstructed with the Σ (DA) methods survive the selection cuts. The kinematic spectra along with expectations from the DJANGO Monte Carlo are shown in figures 5.3, 5.4 and 5.5. The effects of initial state radiation can be seen in the data excesses at high y in figure 5.5 b) and at low $E - P_z$ in 5.3.

5.6 Inclusion of BEMC-BBE Transition Region

The BEMC-BBE Transition or crack region covers the angular range of $150^\circ < \theta < 160^\circ$, with complete azimuthal coverage, representing the region in which electrons scattered from intermediate Q^2 events are to be found. The reconstruction of such events is considerably complicated, however, by the fact that the energy deposited by the electron can be split between the two calorimeters (which occurs in $\sim 40\%$ of the events [54]) or a significant fraction of energy can be lost in the dead material between the two detectors.

The reasons for accessing data in this regime are twofold. The cut of $150^\circ < \theta_e$ excludes large parts of the higher x region in the range $100 \lesssim Q^2 \lesssim 150$ GeV^2, inclusion of which is important in order to ensure no distortion of the data distributions occurs. It is also desirable to bridge the gap between the low Q^2 analysis, extending to $Q^2 = 65$ GeV^2, and the high Q^2 to gain a better appreciation of any changes which may occur as Q^2 increases and due to the higher level of statistics this affords.

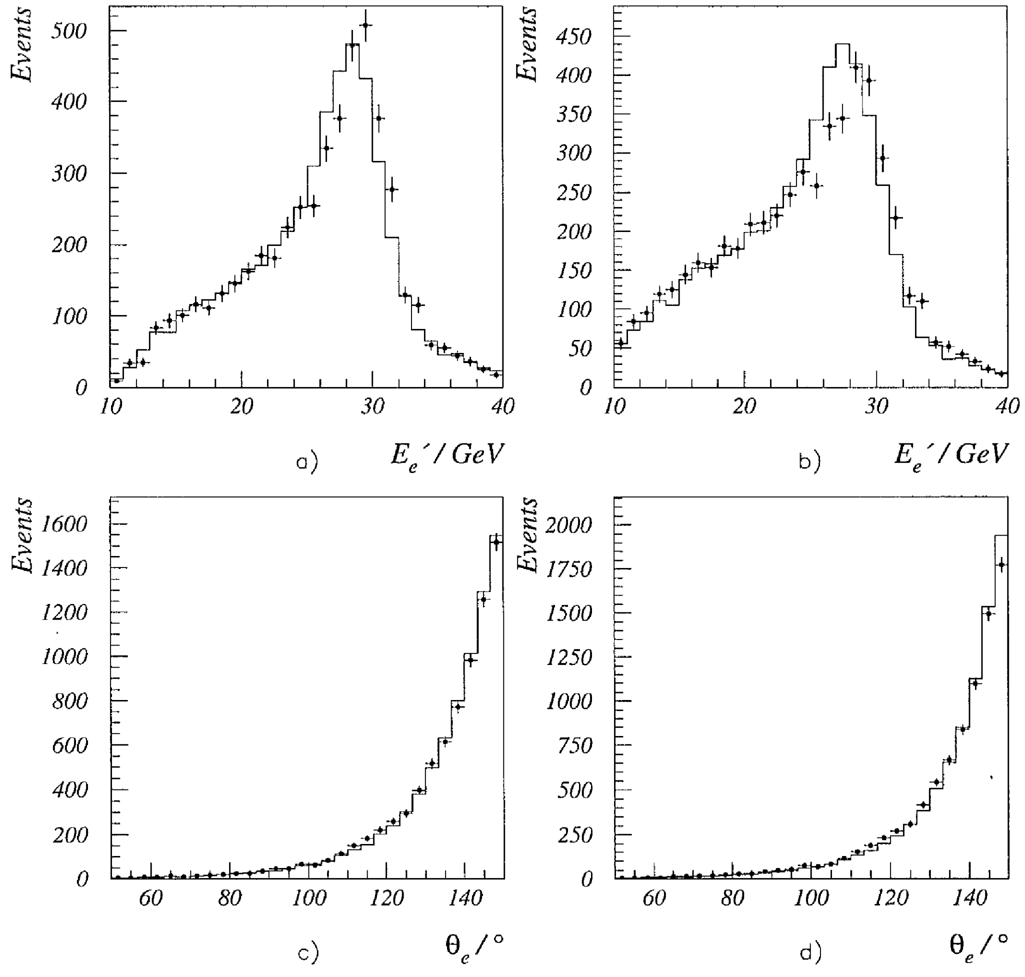

Figure 5.4: Kinematic distributions for the high Q^2 selected DIS events (points) with DJANGO Monte Carlo comparisons (solid line). a) and c) represent data reconstructed using the Σ method, b) and d) the DA method.

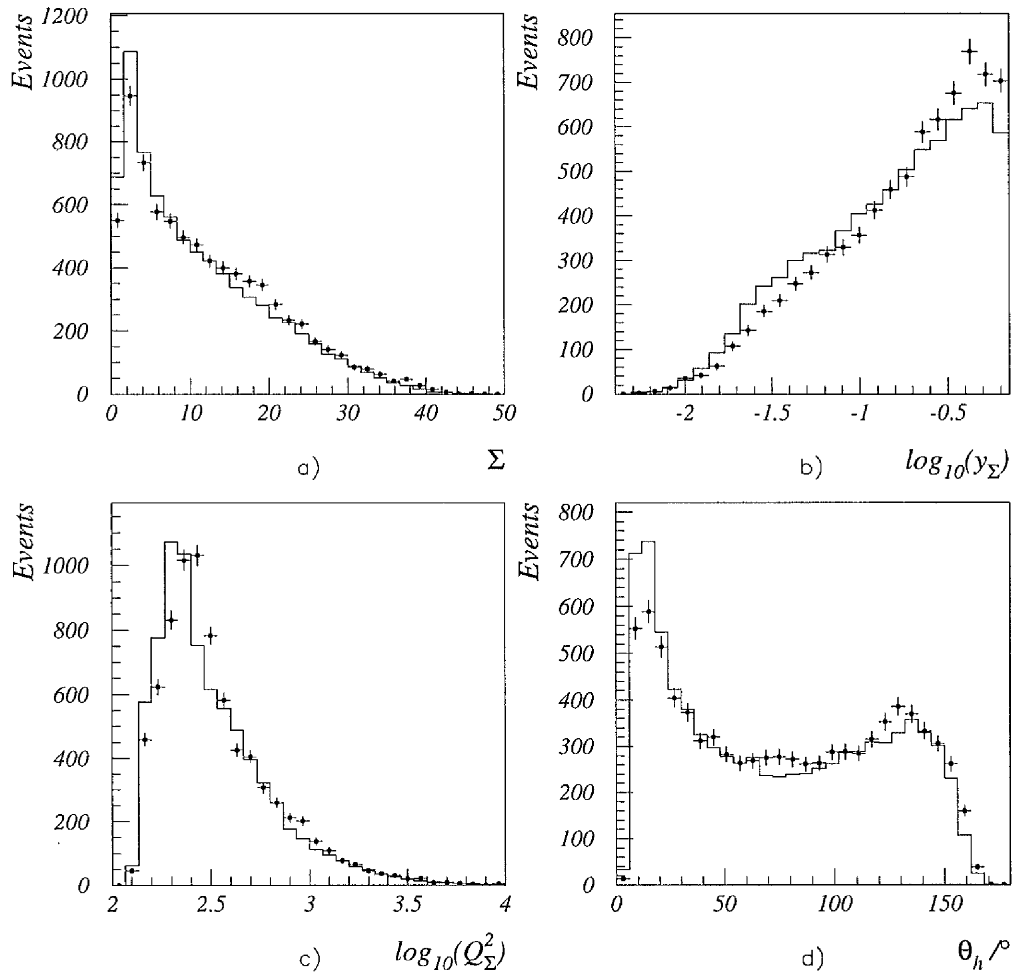

Figure 5.5: Comparison of the kinematic quantities from the selected high Q^2 data with that from the DJANGO Monte Carlo Simulation. Plots a) to c) are from data reconstructed using the Σ method. d) is from data reconstructed using the DA method.

5.6.1 The Selection Procedure

The selection is based on the identification of an electron candidate in either the BBE or the BEMC, taken as the highest energy cluster located in this region with a link to well reconstructed track. This stage is only reached should no electron candidate be found in the LAr barrel or in the BEMC with $\theta_e > 160°$. Since the events of interest span several L5 event classes the selection was made over all 1994 DST's with the run requirements outlined in section 5.1.

In this region the most suitable reconstruction method is the DA method as it makes no assumption on the scattered electron energy, reconstruction being based only on the hadronic final state and the electron direction. The Σ method is still included as a cross-check and to link in with the data so selected in the previous sections. In this case, however, the scattered electron energy is calculated from the DA parameters θ_e and θ_h rather than the energy deposited in the cells of the electron candidate cluster.

5.6.2 Electron Identification

Events are triggered by a global OR of the LAr electron triggers and the BEMC electron subtriggers [54]. The three highest energy clusters located in the BBE or the BEMC are considered. A linked central track is required following the criteria used for track-cluster linking in the LAr barrel. The radial position of the centre of mass of the cluster is restricted to $r > 70$ cm, in order to exclude low Q^2 electrons.

5.6.3 Kinematic Constraints and Background Rejection

The direction of the scattered electron, taken as the angle of the linked track, is restricted to the region of interest: $150° < \theta_e < 160°$. In order to reduce photoproduction contamination events with a current jet in the backward direction are rejected with a cut of $\theta_h < 160°$. The further selection requirements following those of the high Q^2 criteria are summarised below:

- $y_{\Sigma,DA} < 0.7$
- $-25 < \mathrm{ZVTX} < 35$ cm
- $30 < (E - P_z) < 70$ GeV
- $V < 15$ GeV
- $N^{+}_{track} + N^{-}_{track} + N_{clusters} > 2$
- No non-*ep* collisions found by the cosmic/halo finders (section 6.3.1).

The anti-selection of tagged photoproduction events and the estimation of the remaining background is performed in the same way as in section 5.5.3, with tagged and untagged PYTHIA generated events normalised to the data luminosity. The retained photoproduction contamination is estimated to be $0.4 \pm 0.4\%$ for both Σ and DA method selected event samples.

With the Σ and DA methods samples containing 2698 and 2792 events are selected respectively, the kinematic distributions of which are shown in figures 5.6 and 5.7.

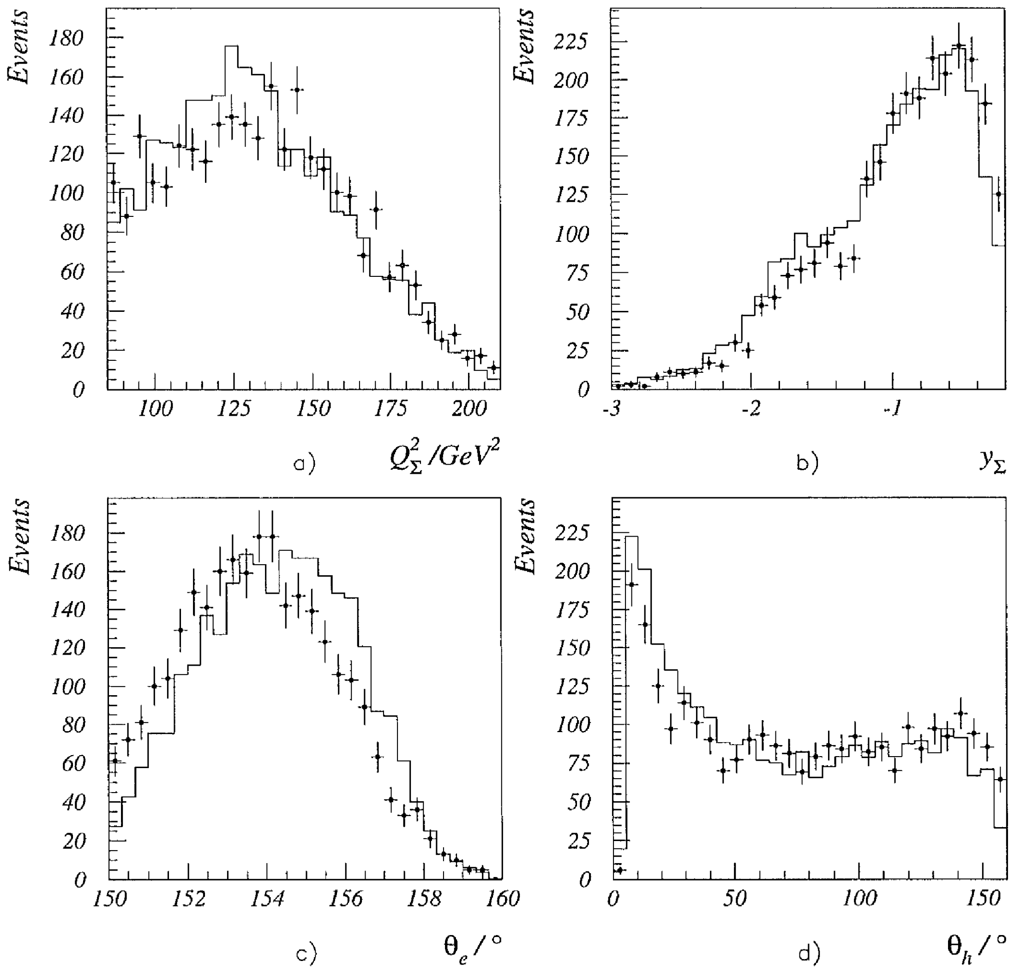

Figure 5.6: Comparison of the 'medium' Q^2 data (points) selected using the Σ Method of reconstruction with a DJANGO Monte Carlo simulation (solid line).

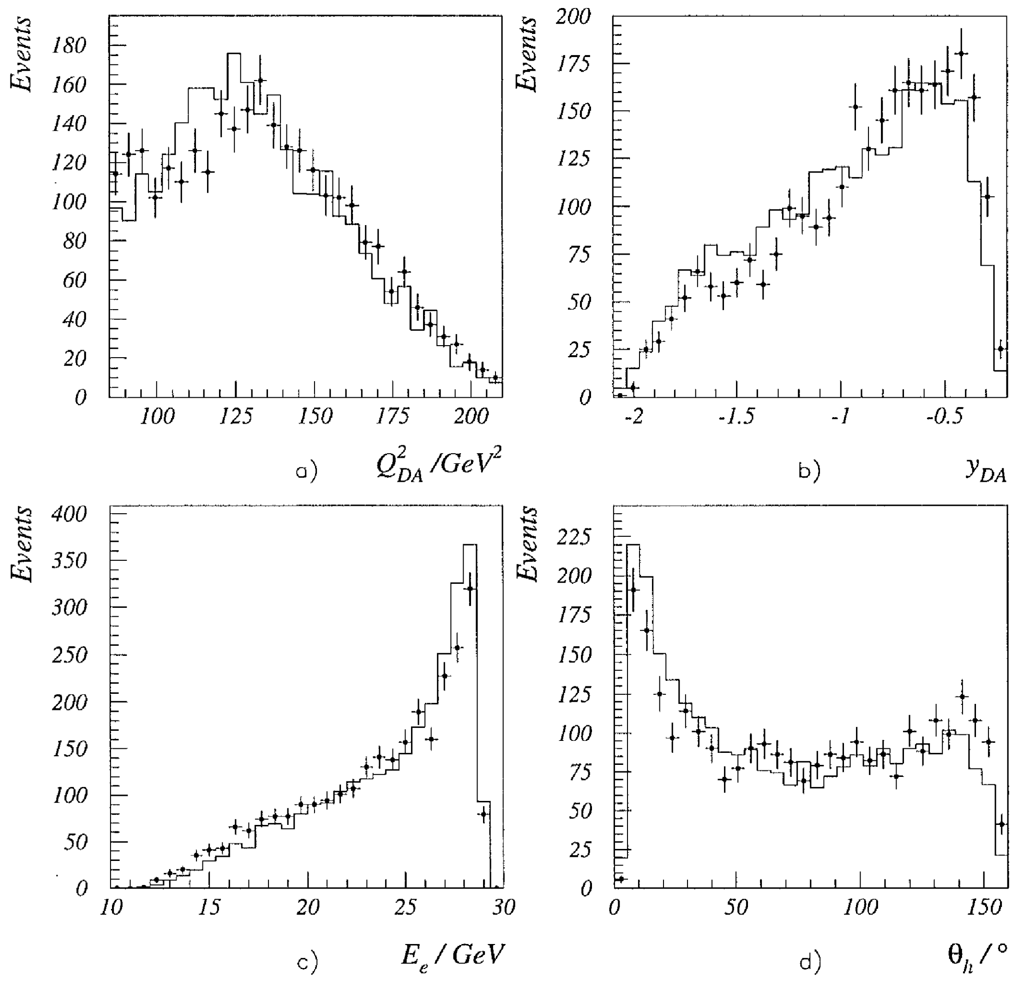

Figure 5.7: Comparison of the 'medium' Q^2 data (points) with a DJANGO Monte Carlo simulation (solid line) reconstructed using the DA method.

5.7 Summary

Combining the two selection procedures results in DIS samples (termed high Q^2 for the remainder of this work) containing a total of 8454 events for the Σ method and 8851 events for the DA method. A negligible background from photoproduction is predicted with non-ep contamination no greater than $\sim 1\%$. The distribution of all events in the $x - Q^2$ plane is shown in figure 5.8.

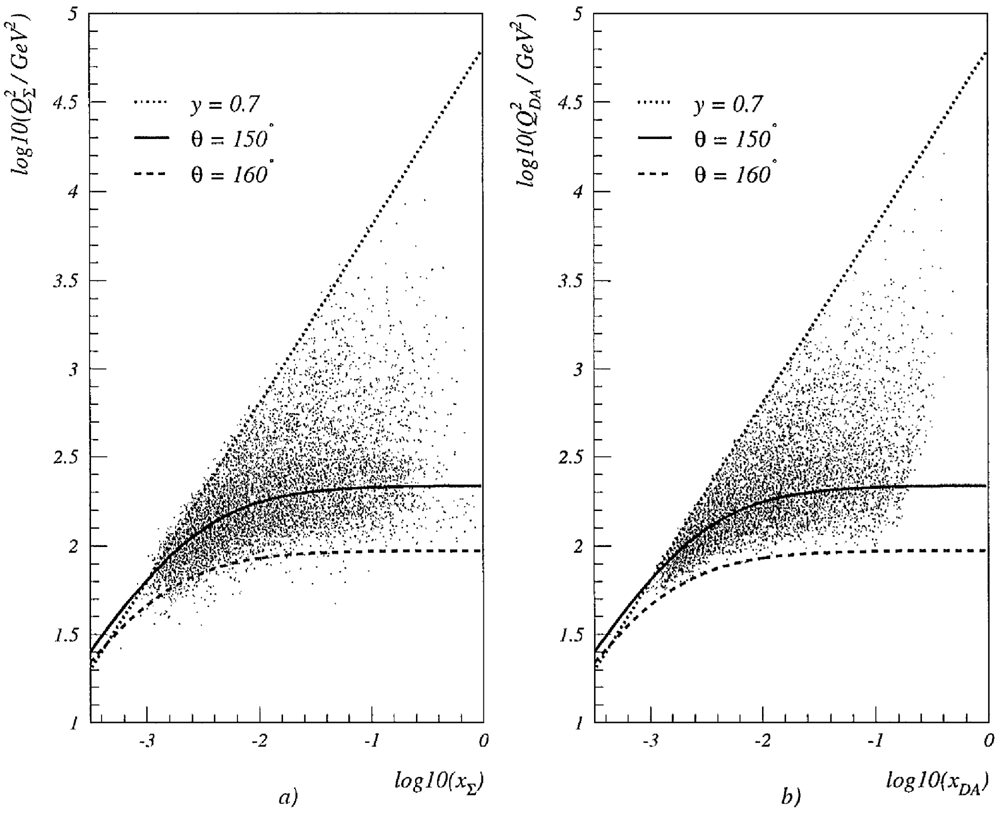

Figure 5.8: The distribution in the $x - Q^2$ plane of the high and medium Q^2 events selected using a) the Σ method of reconstruction and b) the DA method.

Chapter 6

Selection of Charged Current Events

6.1 Introduction

A clear signature for CC events is provided by an unbalanced high transverse momentum hadron system, resulting from the non-detection of the final state neutrino. NC and photoproduction processes are approximately balanced. Selection of CC events is thus based upon the discriminating variable:

$$V \equiv |\sum_i \vec{p}_{\perp_i}| \qquad (6.1)$$

the *vector* transverse momentum sum, which corresponds to the *missing* transverse energy, calculated from the cell energies and positions in the LAr calorimeter. See figure 6.1. The CC process has a very low rate compared to other *ep* interactions and to non-*ep* background sources, necessitating stringent rejection requirements and visual scanning in order to produce a clean sample of signal events.

Events are selected from both the e^-p and e^+p running periods in which the LAr calorimeter, the CTD and the instrumented Iron are fully operational. Runs affected by excessive calorimeter noise are excluded. The corresponding integrated luminosities are 2.70 pb^{-1} for e^+p running and 0.36 pb^{-1} for e^-p.

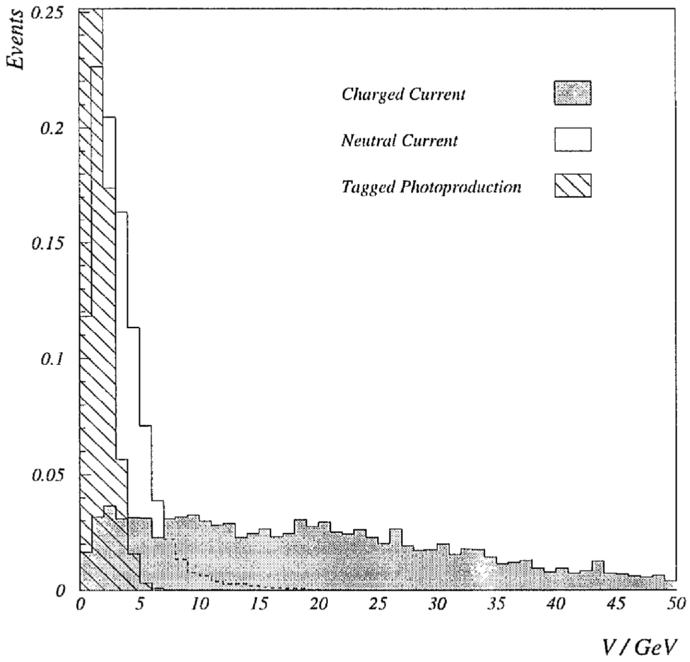

Figure 6.1: The normalised missing transverse energy distributions for CC, photoproduction and NC DIS Monte Carlo samples.

6.2 The Selection Procedure

6.2.1 Trigger Condition

The on-line trigger makes the initial selection. This requires the firing of subtriggers 77 or 66, missing $P_t > 1$ GeV and 2 GeV in the LAr calorimeter respectively, and a z-vertex time signal in anti-coincidence with the Tof-veto signal. The z-vertex time signal identifies the event time and requires at least three of the four CTD MWPC chambers to be hit. After reconstruction at L4, any obvious cosmic, beam halo and beam-gas interactions can be rejected.

6.2.2 POT selection

Events classified at L5 in the event class 8 are considered. The requirements are:

- $V > 10$ GeV
- A good track in the CTD or FTD satisfying the criteria:
  - track length > 10 cm
  - DCA from the nominal $r - \phi$ interaction point < 5 cm

A total of 60754 events are retained.

6.2.3 Kinematic and Vertex Constraints

The vertex is required to lie in the range $-35 < ZVTX < 35$ cm around the nominal interaction point, reconstructed from tracks in the CTD. The slight relaxation in the vertex requirement from that for the NC DIS selection is a consequence of the added uncertainty caused by the absence of an electron candidate with a vertex linked track. In addition there must be at least one CTD track with the primary vertex at its origin. A final cut on the missing transverse momentum of $V > 25$ GeV is imposed. This provides considerable background suppression and limits the data to a region of high trigger efficiency (figure 6.2) whilst retaining reasonably high statistics. The cut sets fiducial limits of $Q^2 > 625$ GeV and $x > 0.03$. In such a region of x large radiative corrections are excluded, so enhancing the reliability of the cross-section measurement.

A total of 1133 events remain in the candidate sample after imposition of the above cuts.

6.3 Muon Induced Background

The remaining sample is dominated by background induced by incoming muons. These arise from two sources: cosmic rays and beam halo interactions. Back-

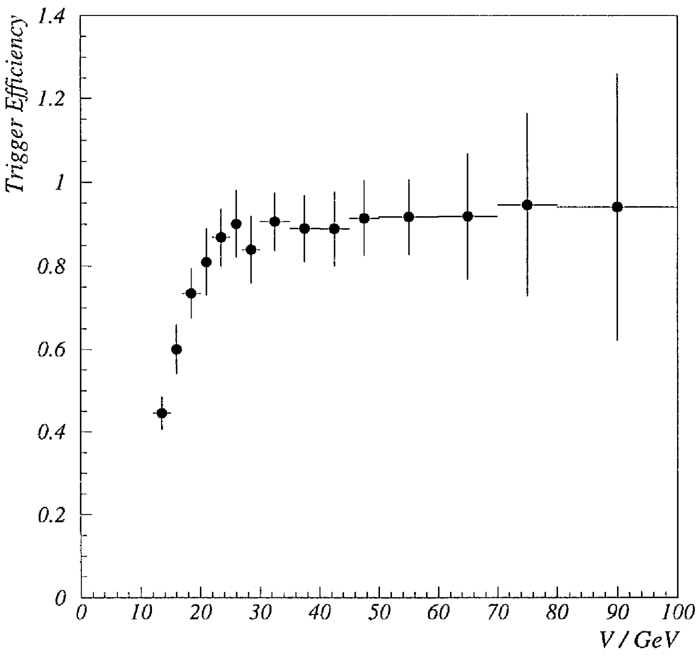

Figure 6.2: Trigger efficiency for CC events as a function of V.

ground from beam-gas interactions is effectively eliminated with the requirement of $V > 25$ GeV [55]. A genuine event can be faked in two ways:

- The muon interacts in the LAr calorimeter, such that sufficient energy is deposited to produce an apparent imbalance in momentum, whilst a charged secondary particle manages to fulfill the vertex requirement.
- A muon is superimposed onto an underlying event which satisfies the vertex requirement.

The background is identified with criteria based on the event topology and the timing of the event in the LAr calorimeter and the CJC.

6.3.1 Identification from Event Topology

A more sophisticated approach is required than for the NC case, as there is no electron with which to discriminate between genuine and background events and the demand for a missing transverse energy is one of the main characteristics of such muon induced background. The various cosmic/beam halo finding routines applied to the data, which employ the differences in the event shape resulting from DIS and the background, are described below.

IRTTL This routine makes use of tracks located in the Iron. A cosmic muon generally produces two tracks on the opposite side of the detector, and an event is classified as such if:

- Two Iron tracks are located.
- The distance between the tracks, R, is greater then 400 cm.
- The scalar product of the track vectors > 0.91.

For events with more than one Iron track the event is identified as being due to a cosmic shower if:

- The scalar product of at least three tracks with another > 0.8.
- $R > 400$ cm , the distance being between at least one track and the others used to calculate the scalar product as above.

IRCTL An Iron energy cluster is matched to an iron track on the opposite side of the detector by demanding that they are separated by a distance $R > 400$ cm and that the scalar product calculated from their respective θ and ϕ's is greater than 0.98. The forward and backward regions of the detector are excluded.

ASCOSM This is a more complex routine with the cosmic muon identification being made via the analysis of large energy deposits in the LAr calorimeter. Six topological variables, $v(i)$, based on the energy weighted coordinates of the event are calculated, combination of which results in a probability value, P, for the origin of the event. It is upon this cosmic/DIS probability that the selection cut is made [56].

The energy moments of all cells active in the event are included from which the vector, $\overline{\vec{x}}$, and tensor, $\overline{X_{i,j}}$ are defined:

$$\overline{\vec{x}} = \frac{\sum_{cell(k)}^{N} E(k)\vec{x}(k)}{\sum_{cell(k)}^{N} E(k)} \tag{6.2}$$

and,

$$\overline{X_{i,j}} = \frac{\sum_{cell(k)}^{N} E(k)x_i(k)x_j(k)}{\sum_{cell(k)}^{N} E(k)} \tag{6.3}$$

where $x_i(k)$ represents the i-th position component of the cell k in the H1 coordinate system. The energy weighted cluster can be modelled by an ellipsoid, the axes of which are given by the eigenvalues (e_1, e_2, e_3) of the above tensor.

The selection variables are:

- $\overline{z}$ - the z component of the centre of gravity of the event, $(\overline{\vec{x}})_z$. For cosmic induced events this is expected to be evenly distributed about the nominal vertex position, whereas for DIS most of the energy, and hence the position of $\overline{z}$, is anticipated to be in the forward region.

- $\overline{r}$ - the radial position of the centre of gravity of the event. In NC interactions this is expected to lie near to the beam pipe, compared to a position in the E.M calorimeter for CC events. In the cosmic case, the frequent presence of energy deposits in the Tail Catcher and electromagnetic showers in the outer regions of the hadronic calorimeter, result in larger values of $\overline{r}$.

- $\overline{r} + \sigma r$ - The sum of the radial distance of and the radial deviation from the centre gravity. This provides an excellent criterion for cosmic recognition. For cosmic events which cross the complete depth of the detector values of $\overline{r} + \sigma r > 200$ cm are possible, far larger than those expected from DIS.

- e_1, θ criterion - For the situation where the major axis of the ellipsoid, e_1, is greater than 0.6 m, the function $v(4)$ is defined as:

$$v(4) = \frac{e_1}{400cm} + \frac{|\theta|}{1.2} \tag{6.4}$$

Large values are a good indication of a cosmic event: the flatter the angle the longer the major axis of the ellipsoid.

- e_1/e_2, θ criterion - The value of e_1/e_2 is a measure of the elongation of the ellipsoid and is generally high for cosmics. The variable $v(5)$ is defined as:

  $$v(5) = \frac{e_1}{e_2} - \frac{4}{|\theta|} \tag{6.5}$$

  this maximises the difference between cosmics (long ellipsoid, mainly high angle) and DIS, where a high value of e_1/e_2 is generally accompanied by a small θ value.

- e_1/e_3, θ criterion - In contrast to the previous criterion the paths of two parallel cosmic muons can be included. The variable $v(6)$ is defined as:

  $$v(6) = \frac{e_1}{e_3} - \frac{10}{|\theta|} \tag{6.6}$$

The final three criteria are only applicable if the *non*-electromagnetic energy deposited in the detector > 1.5 GeV. A total of 10 bins are defined for each variable, each with a corresponding value of a step function $p(i, v(i))$, where $p(i, v(i))$ takes the values 0.001, 0.1, 0.2, ... , 1.0. The bins are optimised for cosmic recognition, with $p(i, v(i)) = 0.001$ for DIS characteristics and $p(i, v(i)) = 1.0$ for cosmics. The overall event probability, P, is then calculated from:

$$P = \left(\prod_{i=1}^{6} p(i, v(i))^{g(i)}\right)^{\frac{1}{\sum_{i=1}^{6} g(i)}} \tag{6.7}$$

where $g(i)$ is a weight introduced for each variable. The classification is then as follows:

- $P > 0.25$: the event is classified as a cosmic, and rejected from any DIS analysis.

- $P > 0.20$: there is a strong likelihood that the event is a cosmic, with a probability of being DIS $\sim 1\%$. The event is retained however for further analysis.

- $P < 0.20$: the events is classified as DIS.

KTR Finder This routine provides further criteria for the identification of cosmics based on the energy weighted topology of LAr clusters and corresponding hits in the Iron. Beam halo events are also classified. Further details are provided by [57].

- *Cosmic Classification*

  To be considered the cluster requires a total energy > 2 GeV with a minimum of four active cells. A major axis as described above is then defined for the cluster and a large cylinder, C, of radius 200 cm is taken around it. The criteria are then as follows:

  - Energy in Iron within C > 2 GeV.
  - Energy in Iron within C on both sides of the Tail Catcher > 0.8 GeV.

  for cosmics with energy deposition on each side of the argon-cluster in the Tail Catcher, and

  - Cluster in same hemisphere as E_t
  - Energy in the Tail Catcher on the opposite side to the cluster and within C > 1 GeV.

  for cosmics with energy in the Tail Catcher only on the opposite side of the cluster.

- *Beam Halo Classification*

  A 'hitmap' is defined in $z - \phi$ space for the LAr calorimeter, with 26 bins in z ($z = -220$ cm to $z = 300$ cm) and 36 in ϕ ($0^\circ < \phi < 360^\circ$). This facilitates recognition of the characteristics of beam halo energy deposits: localised in $r - \phi$ whilst having a wide spread in the z direction consistent with a muon travelling parallel to the beam. Events are classified as beam halo if:

  - The number of hits in z in one bin of $\phi > 17$,

  or,

  - Number of ϕ bins with more than 14 hits in $z = 1$,
  - Number of ϕ bins with less than 7 hits in $z = 35$,

  or,

- Number of ϕ bins with more than 14 hits in $z = 2$,
- Number of ϕ bins with less than 7 hits in $z = 34$,

which locates two halos in one event separated in ϕ, or,

- Number of hits in z in the 'hottest' (highest energy) ϕ bin and both neighbouring bins > 15,
- Number of ϕ bins with (Energy $> E_{total}/4) < 3$.

to identify halo-muons with paths not exactly parallel to the beam, or

- Energy in the Iron within C > 2 GeV.
- Energy in the Iron within C on both sides of the Tail Catcher > 0.8 GeV.
- z component of cluster axis > 0.98.

The Resulting Classification By applying cosmic and halo finders the event sample is categorised into three classes:

- Cosmic class - 596 events
- Halo class - 509 events
- CC class - 88 events remain unclassified by the finders. This contains the genuine CC events along with muon induced background unidentified due to finder inefficiencies.

6.3.2 Identification from Event Timing

Background arising from non-*ep* collision sources and the overlay of such events with genuine *ep* interactions can also be distinguished using the trigger timing in the CJC and in the LAr calorimeter.

The relatively long response time of the LAr calorimeter ($\mathcal{O}$(ms)) renders it sensitive to occasional energy deposits that may pile up shortly before or after those from genuine ep collisions. Such pile ups are typically due to beam halo and cosmic muon showering and beam-wall interactions. The timing information from the LAr calorimeter trigger readout provides a means with which to detect the deposition of energy out of time with tracks or the trigger decision [58].

Triggering in the LAr calorimeter is facilitated by Trigger Towers (TT's), segmentations of the LAr barrel in 23 bins of θ and ≤ 32 bins in ϕ pointing to the nominal vertex [5]. Groups of TT's are combined to form Big Towers (BT's). The number of TT's comprising an individual BT varies between one and four, depending on the region in θ in which they are situated, with a finer granularity provided in the forward region. When the pipeline is stopped by a L1 trigger, the trigger information from each BT is accessed at its nominal maximum (corresponding 14 bunch crossings, taken as the *nominal* T_0 [58, 59]) and also for four bunch crossings around the nominal T_0.

A time estimator is then computed based on the trigger signal over the period $T_0 + 4$ to $T_0 - 4$ bunch crossings and the energy deposits within each BT. Only BT's with cell energies above a noise threshold of 1 GeV are considered. The timing estimator corresponds to:

$$t(BT) = \frac{\sum_{i=-4}^{4} E_i t_i}{\sum_{i=-4}^{4} E_i} \tag{6.8}$$

where E_i represents the digitised cell energies value corresponding to deposition at time t_i. $t(BT)$ is then averaged over all BT's to obtain a mean LAr timing value for each event, T_{LAr}.

Measurement of T_0 is also provided by the CTD. Triggering information from CIP and COP is used to assign the event's T_0 to a particular bunch crossing with more accurate determination within this time interval obtained from the CJC tracking information. It is known that certain hits should lie in a straight line within the CJC. Using this constraint the value of T_0 (T_{CJC}) is taken as that which gives hit coordinates providing the best fit to the required straight lines [60].

A plot of the event timing in the CJC against that in the LAr calorimeter reveals two distinct bands. See figure 6.3 (a). Figures 6.3 (b) and (c) demonstrate how these are attributable to the cosmic and halo muon events.

For the purposes of categorisation, the time bands are defined as:

- I_0 : $T_{CJC} = 0.0 \pm 0.1$ in units of bunch crossing time (1 unit being equal to 96 ns).
- I_1 : $|T_{CJC} - T_{LAr}| < 0.7$. The upper limit allows for the variation in LAr timing within the calorimeter.

Each event can thus be assigned to one of four time *windows*:

Prompt (P) Events 342 events lie in the intersect of I_0 and I_1. This category should contain the genuine CC events.

Superimposed (S) Events 344 non-prompt events in the I_0 band. These are predominantly halo events superimposed onto genuine *ep* interactions. The timing in the CJC is thus correlated with the bunch crossing time but inconsistent with prompt LAr timing.

Uncorrelated (C) Events 414 non-prompt events in the I_1 band. This is dominated by cosmic muon background, the time at which they are detected in the LAr unrelated to the bunch crossing.

Unclassified (U) Events 33 events belong to neither band.

6.4 The Final Sample

The results of the topological and timing classification schemes are summarised in table 6.1.

From the observed number of uncorrelated and superimposed events in the CC class the efficiencies of the cosmic and halo muon finders can be calculated as $\epsilon = 0.98 \pm 0.01$ and 0.97 ± 0.01 respectively.

A total of 272 prompt halo and cosmic class events are observed, along with 18 non-prompt CC class events. 773 events are identified as background by

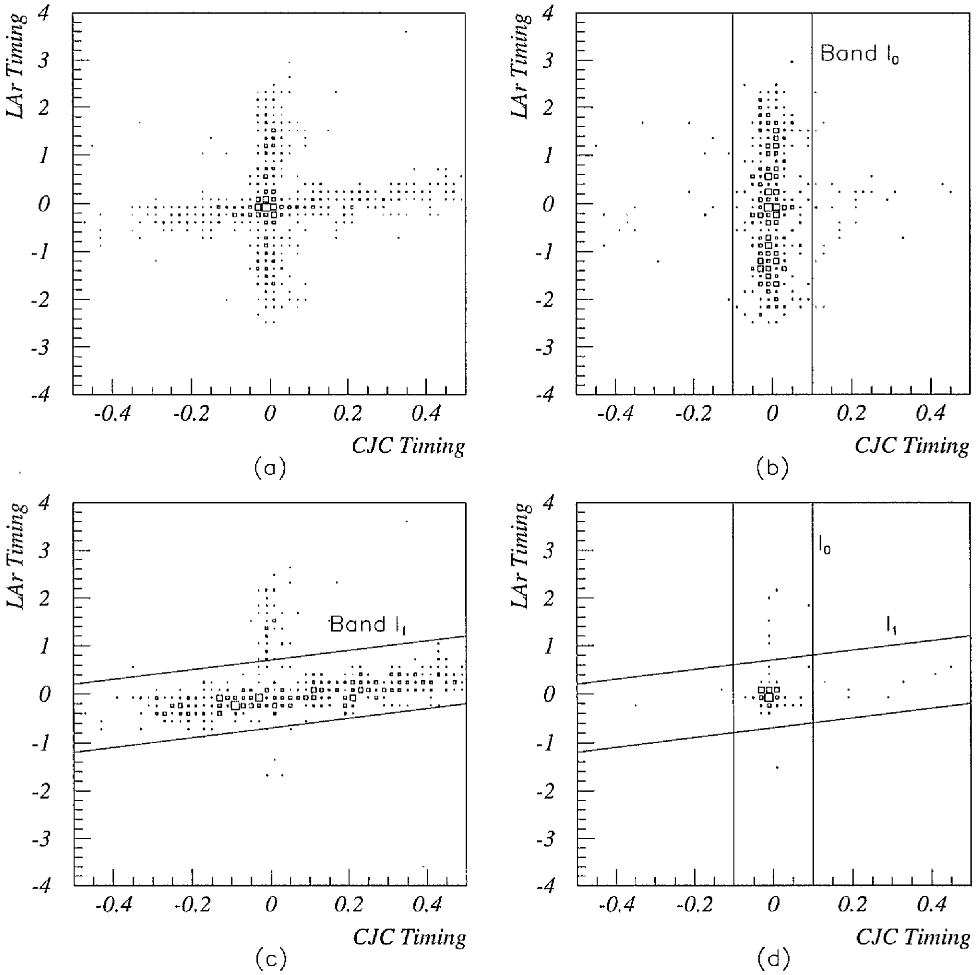

Figure 6.3: LAr timing against CJC timing in units of time for one bunch crossing $\equiv$ 96 ns, for a) all selected events, b) halo class events, c) cosmic class events and d) CC class events, as selected by the topological cosmic and halo muon finders.

Event Classification	All	P	S	C	U
All	1133	342	344	414	33
Halo	509	159	287	38	25
Cosmics	536	113	50	366	7
CC Class	88	70	7	10	1

Table 6.1: Results of the topological and timing classification of the 1133 events passing the CC selection criteria.

both schemes. This implies a further $(272 \times 18)/773 = 6 \pm 2$ muon background events in the sample of 70 prompt CC class events.

Visual Scan

All 88 CC class events are subjected to a visual scan. The 18 non-prompt events are indeed identified as cosmic or halo muon background. The total of prompt muon background events is found to be 8, in good agreement with the above prediction. The rest of the sample is identified as follows:

- 6 NC events where the loss of the final state electron or positron through a crack in the detector has lead to misclassification.
- 1 event due to calorimeter noise.
- 2 events containing an isolated final state lepton with a high P_t. Both of these events are possible W production candidates and are of interest in their own right [61].
- 53 CC events, 41 from positron and 12 from electron runs.

An example of the selected CC events is shown in figure 6.4 clearly demonstrating the absence of an electron and an imbalance in the transverse momentum of the hadronic final state. The distribution for all 53 events in the $x - Q^2$ plane is shown in figure 6.5, where the kinematics are calculated using the hadronic method of reconstruction.

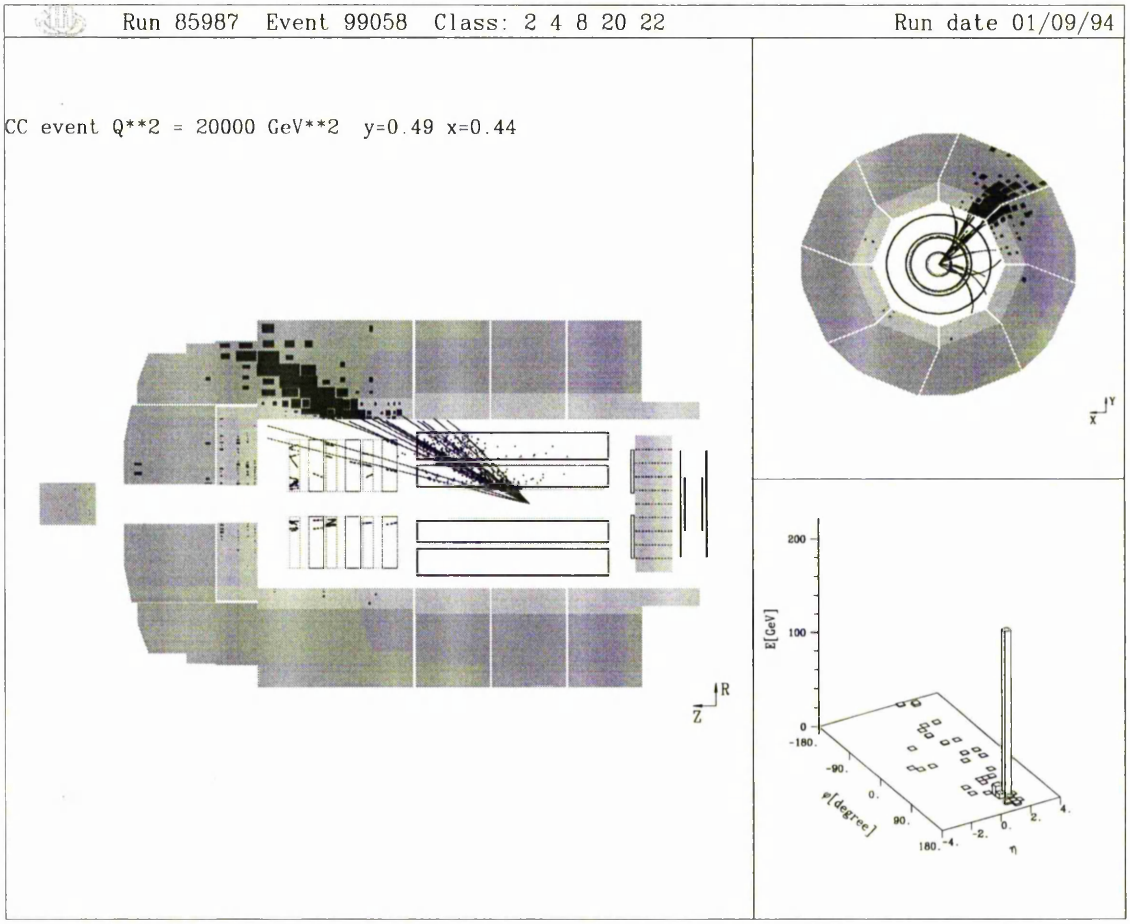

Figure 6.4: Event display of a CC interaction arising during the e^+p running period.

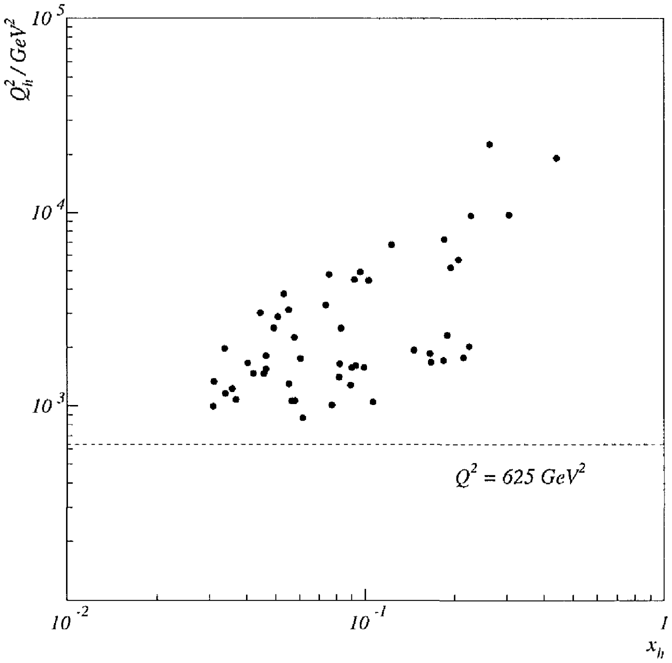

Figure 6.5: Distribution in the $x_h - Q^2_h$ plane for all 53 events in the final CC sample with $V > 25$ GeV.

6.5 *ep* Background

6.5.1 Photoproduction Background

At high values of transverse energy photoproduction interactions generally have the signature of two planar jets, balanced in transverse momentum, with $V \approx 0$ GeV and would not be expected to contaminate the final CC sample. However, a missing transverse momentum can be seen for these events if there are significant particle losses in the beam pipe or if the measurement is affected by poor resolution in the LAr calorimeter. If untagged, such an event could pass the CC selection criteria [62].

A method of extrapolation of the photoproduction V distribution from a *control* region of $V > 10$ GeV to the signal region ($V > 25$ GeV) is employed to quantitively assess this background. This has the advantage of making no assumptions on the resolution of the calorimeter. A cut of $V > 10$ GeV still has a reasonable efficiency for the discrimination of CC events, but it will accept in a substantial number of high transverse momentum photoproduction events; enough to allow a prediction of their behaviour as V approaches 25 GeV to be made.

Modified criteria are used for the selection of the control sample with considerably relaxed trigger requirements. This removes the effect of the reduced trigger efficiency at $V < 25$ GeV, which would result in a flatter line of extrapolation. The electron finding algorithm, outlined in section 5.4.2, is also used to remove unwanted NC DIS interactions. Events for which an electron energy greater than zero is measured are rejected. A total of 5600 events satisfy the control requirements.

Extra halo and cosmic muon finders used to ensure that the sample is as pure in photoproduction and CC events as possible are briefly described below:

- hal1: a cylinder of radius 25 cm is taken around any Iron cluster or track in the forward or backward endcap running parallel to the beam pipe. All LAr cells with energy > 100 MeV are summed.
- hal2: a cone of angle 20° is taken around the most energetic hadronic cluster. The energy distribution in the various calorimeter layers contained within the cone is then checked for extreme cases, such as deposition in the outer 3 hadronic layers only, with no energy towards the event vertex.
- Events are also rejected if no well defined cluster is located in the LAr calorimeter.

These may result in the loss of *ep* interactions, but the sample purity is the primary concern in this instance. After applying these topological cuts 546 events remain.

The LAr and CJC timing categorisation, as described in section 6.3.2, confirms the tightness of these extra cosmic/halo cuts, with none of the 546 CC class events lying in the S (halo) time band (see table 6.2). After rejecting the 36 non-prompt events a control sample of 510 photoproduction and CC interactions is obtained with an estimated cosmic muon background of 16 ± 3 events, i.e. less

Event Classification	All	P	S	C	U
All	5600	2105	1192	1616	687
Halo/Cosmic	5054	1595	1192	1589	678
CC Class	546	510	0	27	9

Table 6.2: Results of topological and timing categorisation for the $V > 10$ GeV control sample.

than 4 %. Within this sample a total of 74 events are identified unambiguously as photoproduction interactions by the electron tagger, figure 6.6.

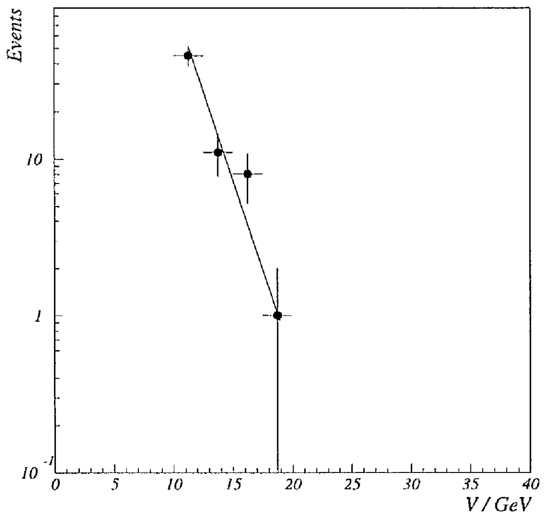

Figure 6.6: The 74 e-tagged events from the $V > 10$ GeV selected sample fitted to an exponential curve.

Parameterisation of the V distributions for both the CC and photoproduction samples is required in order to make a fit to the control data. A quadratic fit is made to the CC Monte Carlo sample with the above selection cuts applied, in the region of $10 < V < 40$ GeV. The χ^2 value for this fit is $1.13/n.d.f.$

For the photoproduction distribution a sample of 10000 PYTHIA generated high P_t untagged events is produced. An exponential fit is made with a χ^2 value of $1.46/n.d.f.$ The functions for both Monte Carlos are shown in figures 6.7 (a) and (b).

The sum of these two parameterisations is then fitted to the data with $\chi^2 = 0.35/n.d.f.$ The exponential slope from the photoproduction contribution is extrapolated into the signal region, integration of which gives a background prediction of 0.4 ± 0.3 events in the final event sample. i.e. $\sim 1\%$. See figure 6.8.

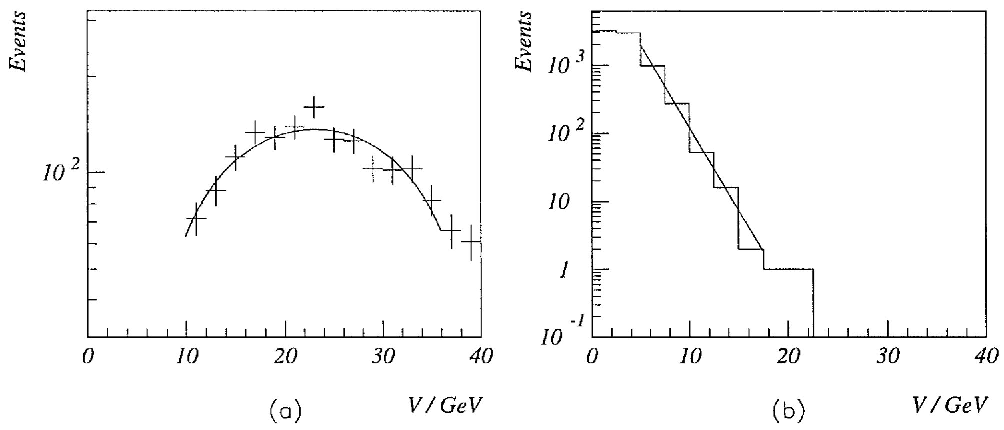

Figure 6.7: Parameterisation of the Monte Carlos used to establish the extent of photoproduction contamination in the CC sample: (a) quadratic fit made to the CC Monte Carlo V distribution and (b) exponential fit to an untagged photoproduction sample.

6.5.2 High Q^2 DIS Background

The CC interaction may be faked if the scattered electron from a high Q^2 NC process remains undetected or if a poor energy measurement gives a false value for the missing transverse momentum. The electron can escape detection in two ways:

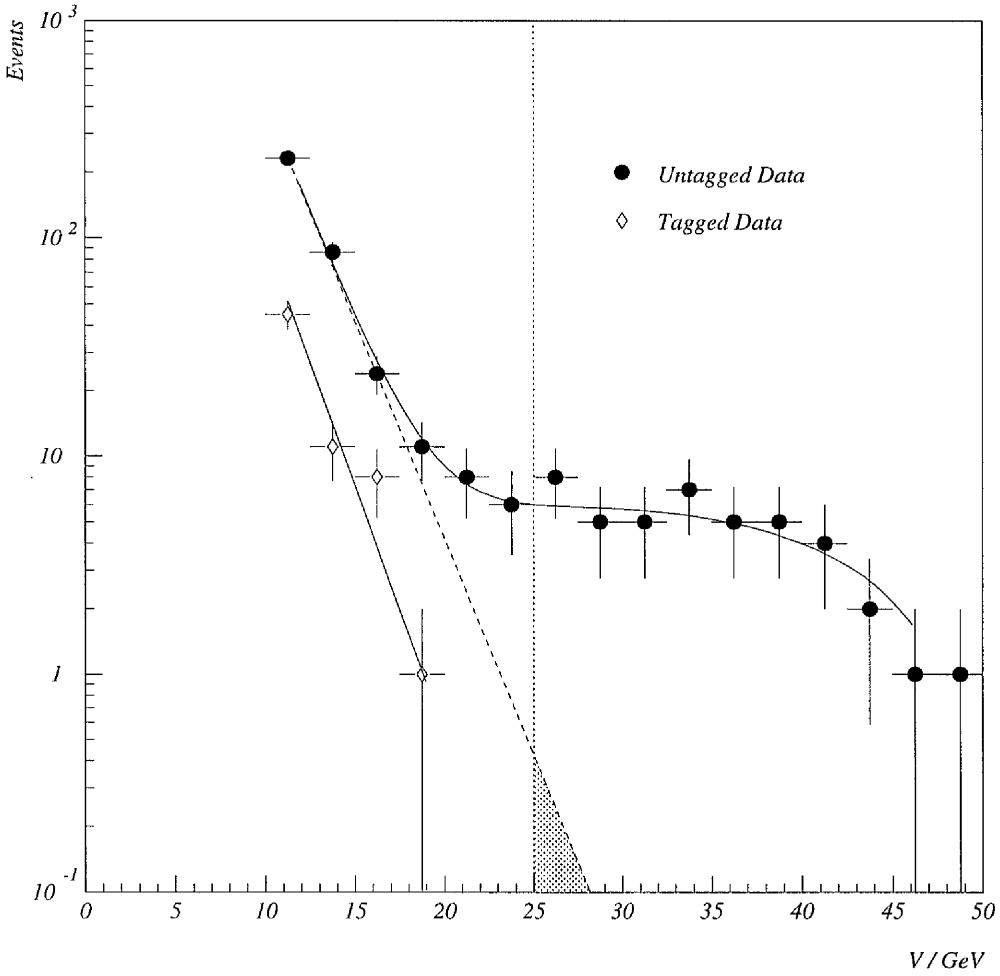

Figure 6.8: V distribution of data selected for photoproduction background studies. The data is represented by the closed circles, the solid line being the result of the fit with a χ^2 value of $0.35/n.d.f.$ The dashed line shows the extrapolation of the photoproduction exponential fit into the region of $V > 25$ GeV and the shaded area represents the expected contamination of the CC sample. E-tagged photoproduction events in the sample are also included as open diamonds.

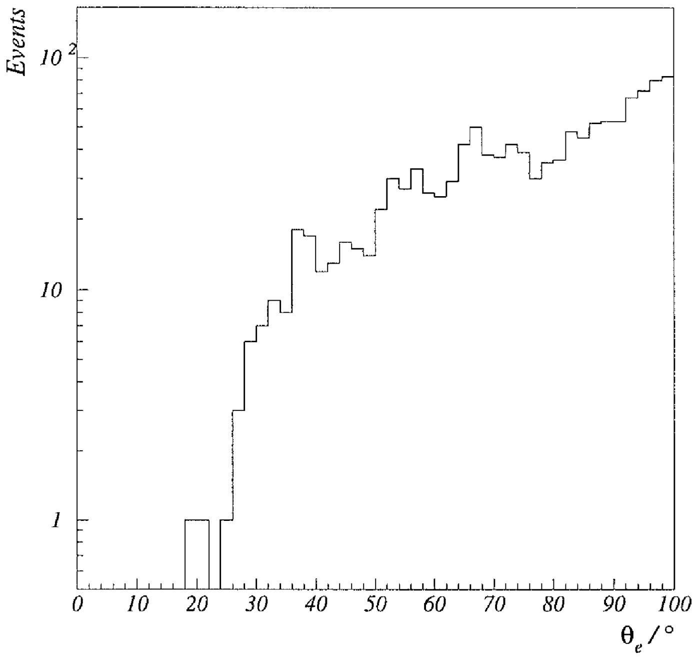

Figure 6.9: Angular distribution of the scattered electron for the high Q^2 class 9 miniPOT sample with $P_t > 10$ GeV.

- the electron is scattered in the extreme forward direction ($\theta_e < 4°$) and is lost down the beam pipe i.e. at ultra-high Q^2 ($Q^2 \gtrsim 30000$ GeV^2).
- the electron strikes a dead region or a crack in the detector.

Events corresponding to the latter scenario and those with an incorrect V measurement are effectively rejected with a visual scan as the electron cluster or isolated track can be easily identified. That the former background is negligible is demonstrated in figure 6.9: a plot of θ_e, the reconstructed angle of the scattered electron, for the entire class 9 miniPOT sample with $P_t > 10$ GeV, for which no electron is located at $\theta_e < 10°$.

Chapter 7

Observation of High Q^2 Diffractive DIS

7.1 Introduction

The lower luminosity received by H1 in 1993 made the study of diffraction impracticable at Q^2 values greater then $\sim$ 80 GeV^2. With an increase of order ten in the level of statistics produced in 1994 sufficient numbers of high Q^2 events exhibiting a rapidity gap are present for meaningful analysis. Even so, the very high Q^2 regime ($\sim$ 1000 GeV^2 and above) remains beyond reach.

7.2 The Selection of Diffractive Events

Identification of a diffractive event requires the detection of the elastically scattered proton or of the forward rapidity gap devoid of hadronic energy. The proton is invariably lost along the beam pipe, so the selection is reliant on the observation of a gap in rapidity larger than that expected from a standard DIS interaction.

The quantity η_{max} characterises the size of the rapidity gap, defined as the rapidity of the most forward detected cluster in the LAr calorimeter with an energy ≥ 0.4 GeV. Figure 7.1 a) shows the η_{max} spectrum of the entire *low* Q^2 DIS sample, where an electron is detected in the BEMC. There is a clear 'tail' extending to smaller values than those expected for standard DIS, attributable to diffractive interactions [39]. That the same tail is visible in the high Q^2 data (figure 7.1 b)), is a strong indication that the diffractive process extends into this region.

The selection of rapidity gap events during the early days of diffractive studies at H1, was based on entirely on a cut of $\eta_{max} < 1.8$ [22]. This ensured a relatively clean sample of events, with a non-diffractive background of $\sim 5\%$. However, as shown in figure 7.2, the selection only identifies a certain fraction of the total diffractive contribution, with a substantial number of events having a rapidity gap too small to allow discrimination from standard DIS events with the calorimeter η_{max} cut alone. This limitation also results in a distortion of the diffractive kinematic distributions in the final sample [63].

A far more embracive selection was developed with the inclusion of the forward detectors: the Plug, FMD and the proton tagger [63]. These cover the regions of $3.65 < \eta_{max} < 5.08$, $5.0 < \eta_{max} < 6.6$ and $5.8 < \eta_{max} < 8.0$ respectively and are of particular importance as they lie in the range in which hadron production is most likely to be depleted by colourless momentum transfer coupling to the proton [29]. For standard DIS there is expected to be significant energy flow in this region with hits reconstructed in the FMD and energy deposition in the Plug and forward Iron endcap. In the case of events exhibiting a large rapidity gap there is a conspicuous absence of any significant activity in the forward detectors inconsistent with detector noise. Details of the problematic reconstruction and calibration techniques required in utilising these detectors can be found in [63].

The range of η_{max} in which diffractive events can be selected is extended to $\eta_{max} = 3.2$, so almost the entire acceptance of the LAr calorimeter ($\eta = 3.65$) is available for subsequent analysis. This has the consequence of increasing the number of selected events with a well defined M_x and the range in which M_x can be measured. The kinematic limit imposed on the value of $x_{\mathbb{P}}$ (equation 4.10) is raised from 0.01 for the η_{max} only selection to 0.05.

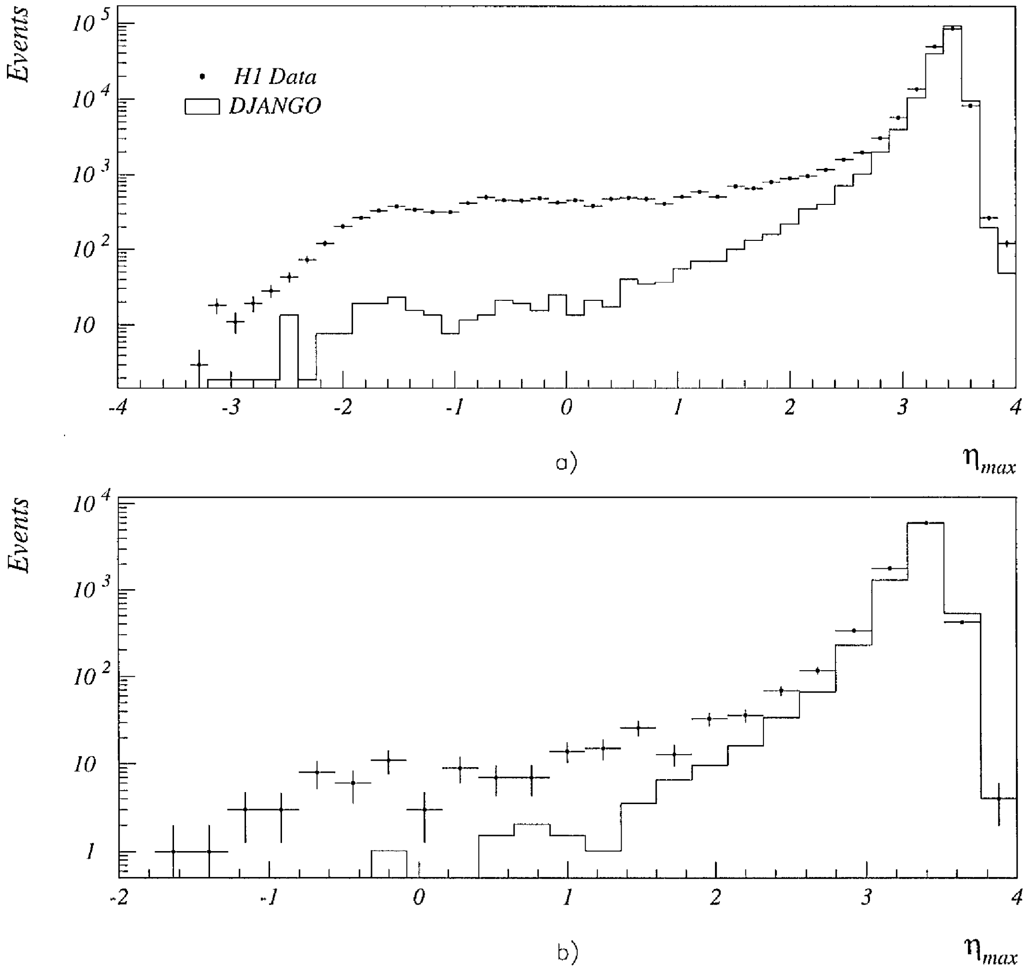

Figure 7.1: Distribution of maximum pseudo-rapidity, η_{max} for a) low Q^2 DIS data and b) high Q^2 data, along with the expectation from the DJANGO Monte Carlo.

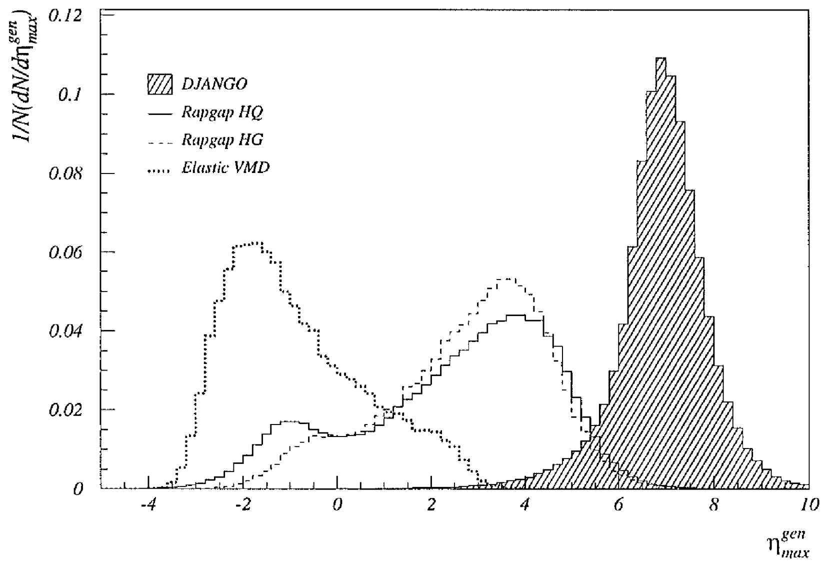

Figure 7.2: Distributions of the generated η_{max} for diffractive and non-diffractive Monte Carlos. HQ and HG refer to hard quark and hard gluon $\mathbb{P}$ structures respectively. The entire Q^2 range is included.

7.2.1 The Selection Criteria

The energy requirements in the forward detectors represent a compromise between the acceptance of energy deposition due entirely to detector noise and the rejection of activity product of genuine ep collisions. The criteria for the selection of diffractive events are as follows:

- $N_{FMD} \leq 1$ - where N_{FMD} is the number of paired hits in the inner three layers of the FMD. Charged particles typically give a hit in both planes of any layer, whereas hits resulting from noise are randomly distributed. A pair is defined as any two hits found in each of the two planes with a separation in the drift coordinate of less than 9 cm. Only one hit per cell is considered and no one hit can be used in more than one pair [7]. The noise level of the FMD is extremely low, with ≈ 0.005 hits per cell per event [63], arising, in the main, from the electronics of the readout system. The outer three detector layers are not utilised in this selection due to there susceptibility to register synchrotron radiation produced by the incoming electron bunch.

- $NPC < 1$ GeV - where NPC is the total number of cells in the Plug with an energy deposition above a noise threshold of 300 MeV. No constraint is placed upon the energy distribution within the Plug. It should be noted that the Monte Carlo energy needs to be scaled by a factor of 0.4 to gain agreement with data.
- $N_{PTAG} = 0$ - representing the total number of scintillators which register a pulse in the proton tagger. The noise level in this device is almost zero.
- $\eta_{max} < 3.2$
- $x_{\mathbb{P}} < 0.05$ - studies using the various diffractive models confirm that the limit imposed on the value of $x_{\mathbb{P}}$ by the selection $\eta_{max} < 1.8$ expected at the parton level still holds true after hadronisation [64]. With no such limit imposed on standard DIS events, the reconstructed $x_{\mathbb{P}}$ is an effective discriminating variable.

From the DIS sample selections described in chapter 5 a total of 234 (253) events are selected for the Σ (DA) reconstruction methods, i.e. $\sim 3\%$ of the events in both cases.

7.3 Background Levels

The main background contribution is due to standard DIS events in which a rapidity gap occurs from statistical fluctuations in the parton hadronisation and $x_{\mathbb{P}}$ values are smeared down into the signal range due to finite detector resolution and the effects of undetected particles. An estimate of this contribution is made using the DJANGO Monte Carlo, the DIS background being defined as those events with a generated value of $x_{\mathbb{P}}$ greater than 0.1 [29]. This definition follows from a reassessment of standard DIS Monte Carlos as containing a poorly described diffractive component at $x_{\mathbb{P}} < 0.1$ [29, 65]. The number of Monte Carlo events are normalised to that resulting from the DIS data selections in the region $\eta_{max} > 3.2$, to suppress diffractive events as far as possible. Approximately 0.5% of the DJANGO sample satisfy all diffractive criteria, from which a prediction for the non-diffractive contamination of $\approx 16\%$ is made.

This non-diffractive component does not, however, fully describe the data of the diffractive sample. A further high $x_{\mathbb{P}}$ component would seem to be required in order to obtain a more faithful representation of the data. This can be provided with the inclusion of a RAPGAP generated pion exchange sample, the generated $x_{\mathbb{P}}$ values of which are shown in figure 7.3. Some contamination from the pion exchange process is to be expected, although the use of the pion exchange Monte Carlo can partly be seen as a convenient tool with which to compensate for the inadequacies in the RAPGAP $\mathbb{P}$ and DJANGO simulations. In this phenomenological approach all events with a generated value of $x_{\mathbb{P}} < 0.05$ are considered to be components of the genuine diffractive signal, irrespective of their source.

The total photoproduction background to the DIS sample is estimated to be $0.2 \pm 0.1\%$. Under the assumption that the degree of smearing into the diffractive region follows that of the DIS case i.e. $\sim 0.5\%$, the possibility of non-diffractive photoproduction contamination in the diffractive sample can be neglected.

7.4 Diffractive Monte Carlo Comparisons

The contribution from direct processes to the data is expected to be negligible. An event sample generated by the DIFVM program is normalised to the maximum 10% expectation in the low Q^2 diffractive data. Extrapolation into the high Q^2 region gives a prediction of ~ 1 event entering the data sample.

Any Monte Carlo mixture used ($\mathbb{P}$/pion/DIS) must provide a good description of the both the diffractive data sample and the DIS sample prior to any diffractive selection. In order to establish the required mixture the RAPGAP $\mathbb{P}$ contribution is first constrained by normalising the number of events in the Monte Carlo surviving all diffractive cuts with$x_{\mathbb{P}} < 0.0075$to that from the data. At such a low value of $x_{\mathbb{P}}$ contamination from high $x_{\mathbb{P}}$ background is expected to be considerably suppressed. With this constraint the remaining pion/standard DIS contributions

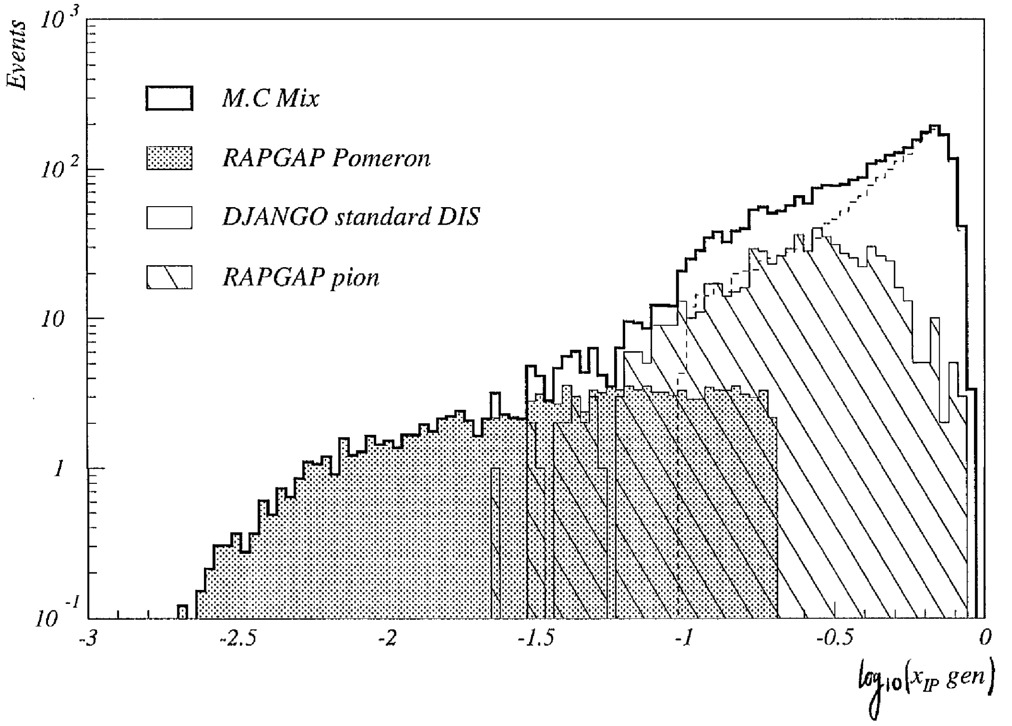

Figure 7.3: Generated values of $x_{\mathbb{P}}$ for the Monte Carlo samples following all DIS cuts. The mixed sample and the normalisations are as described in the text.

are adjusted to produce the best fit to the η_{max} and $x_{\mathbb{P}}$ distributions of the total DIS and the diffractive data, following normalisation to the observed number of DIS events. The fits are performed over 10 bins for the DIS sample and only 3 bins for the diffractive, in order to avoid the effects of large statistical fluctuations. Following this procedure a mixture of 4.9% RAPGAP $\mathbb{P}$, 25.2% RAPGAP pion and 69.9% DJANGO Monte Carlos is obtained as a description of the total DIS data[1]. These proportions correspond to a parameterisation of the diffractive sample with 64.9% RAPGAP $\mathbb{P}$, 22.8% RAPGAP pion and 12.2% DJANGO. As stated above any event with a generated value of $x_{\mathbb{P}} < 0.05$ is considered to be a signal event. As such, the above parameterisation suggests that the background contribution to the diffractive sample is $\approx 23.6\%$ with $\approx 50\%$ of the pion exchange simulation satisfying

---

[1] Figure 7.4 shows the mixed Monte Carlo $x_{\mathbb{P}}$ distribution fitted to all DIS data

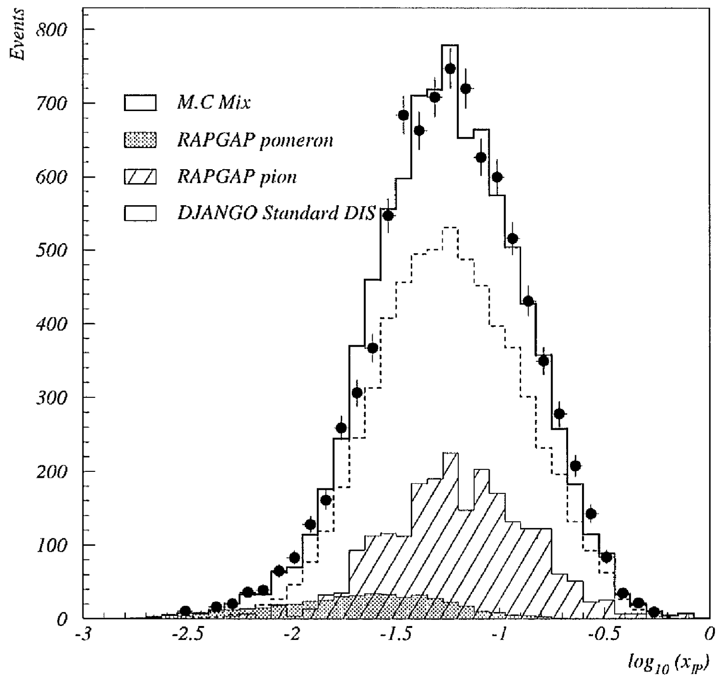

Figure 7.4: The $x_{\mathbb{P}}$ distribution for all DIS data selected using the DA method (prior to diffractive cuts) compared to the spectra of the RAPGAP $\mathbb{P}$/pion, DJANGO standard DIS and the normalised Monte Carlo mix samples.

the diffractive criteria with $x_{\mathbb{P}}^{gen} < 0.05$.

It is clear from the control plots in figures 7.5 and 7.6 that there is some discrepancy between the observed behaviour of the data and that of the Monte Carlo. The failings in the Monte Carlo descriptions of the $x_{\mathbb{P}}$ and the β distributions are, however, somewhat contradictory suggesting the need for increased RAPGAP $\mathbb{P}$ and increased DJANGO components respectively. Such shortfalls are not unexpected with the low level of statistics observed in the data in this regime.

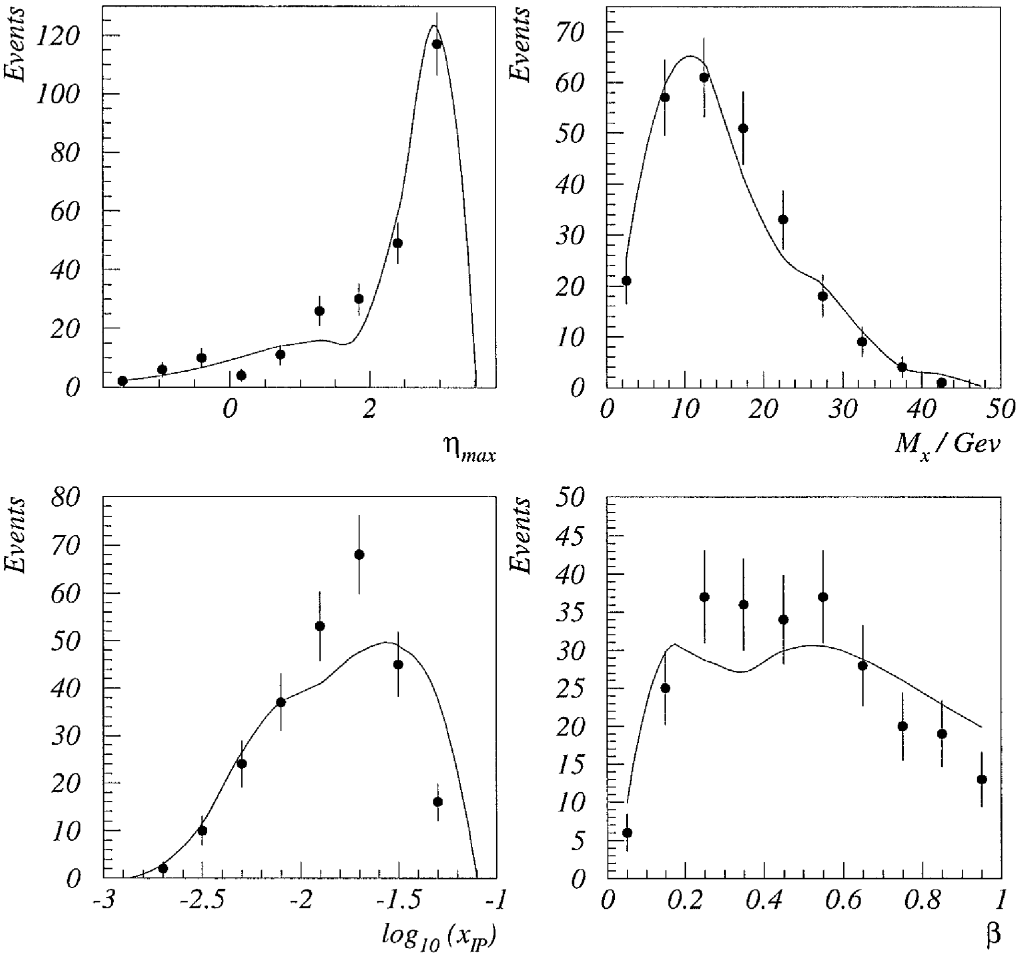

Figure 7.5: Comparison of the mixed Monte Carlo and data following diffractive selection. Statistical errors only are shown. Reconstruction follows the DA method.

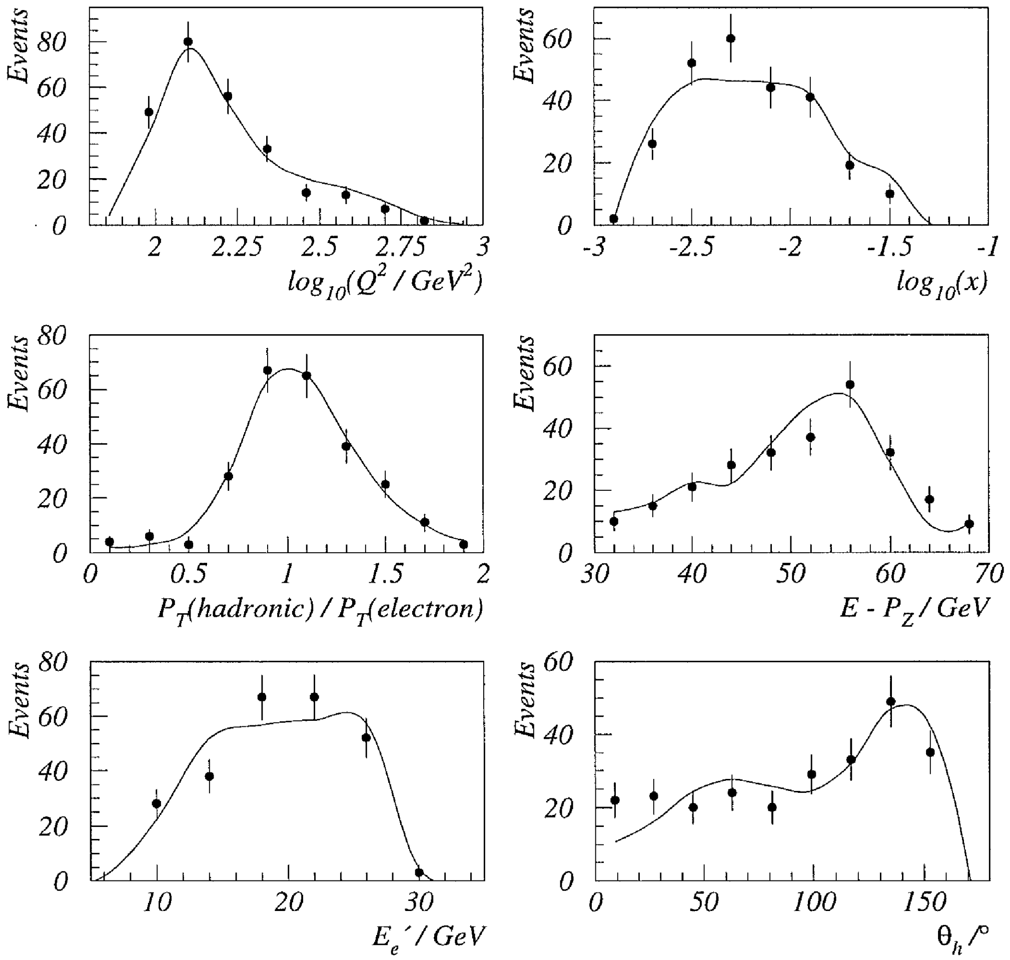

Figure 7.6: Further plots comparing the diffractive data sample with the Monte Carlo description.

Chapter 8

Measurement of the Diffractive Structure Function $F_2^D(\beta, Q^2, x_{\mathbb{P}})$.

8.1 Determination of $F_2^D(\beta, Q^2, x_{\mathbb{P}})$

The diffractive events are selected as described in chapter 7. A bin-by-bin approach is taken in order to determine the diffractive cross-section and hence $F_2^D(\beta, Q^2, x_{\mathbb{P}})$, with the events assigned to bins according to their position in x, Q^2 and β space. The true number of diffractive events in each bin is estimated with the aid of Monte Carlo simulation after all relevant background processes are subtracted or accounted for. Both reconstruction methods, Σ and DA, are utilised, providing mutual cross-checks.

For each bin $F_2^D(\beta, Q^2, x_{\mathbb{P}})$ is determined from the Born cross-section following equations 4.27 and 4.28:

$$F_2^D(\beta, Q^2, x_{\mathbb{P}}) = f(x, \beta, Q^2)\frac{d^3\sigma(ep \to epX)}{dx dQ^2 d\beta} \tag{8.1}$$

The value of the structure function so calculated is quoted at a specific point within the bin, the bin centre. This is taken as the point in the bin where the value of F_2^D, as evaluated from the Monte Carlo mixture, is at its mean value and is approximately equal to the mid-point in the bin.

The evaluation of the cross-section can be summarised with the following equation:

$$\frac{d^3\sigma(ep \to epX)}{dx dQ^2 d\beta} = \frac{N}{A\varepsilon\mathcal{L}} \cdot \left(\frac{\int_{bin} d^3\sigma \, d\beta dQ^2 dx}{d^3\sigma_{centre}} \right)^{-1} \cdot f_{noise} \cdot f_{pdiss} \tag{8.2}$$

the components of which are defined as follows:

N - the number of data events reconstructed in the bin.

A - the smeared acceptance. This is calculated solely from the input Monte Carlo and is defined as:

$$A = \frac{N_{rec}}{N_{gen}} \tag{8.3}$$

where N_{rec} is the number of Monte Carlo events reconstructed in the bin and N_{gen} the number generated. This takes into account the smearing of signal events from one bin to another and the migration of standard DIS or pion exchange background processes from the high $x_{\mathbb{P}}$ region into the signal region.

ε - represents the trigger efficiency. The LAr electron triggers are not simulated by the Monte Carlos and the must be accounted for with this scale factor. The efficiency is found to be $\approx$ 100%, to within errors, for all events with a scattered electron energy, E_e, greater then 12 GeV. The efficiency falls to no less than 92% at $E_e = 8$ GeV.

$\left(\frac{\int_{bin} d^3\sigma \, d\beta dQ^2 dx}{d^3\sigma_{centre}} \right)$ - The corrected bin volume applied so that the differential cross section may be calculated at the bin centre. For a bin in which the events are evenly distributed this is simply equal to the inverse of the bin area. The value is determined from the diffractive Monte Carlo.

$\mathcal{L}$ - the integrated luminosity.

f_{noise} - a factor of 1.08 is applied to account for the losses due to noise in the forward detectors. Full details of the evaluation of this factor can be found in [63].

f_{pdiss} - in order to obtain the *elastic* cross section events in which the proton dissociates must be vetoed. This is done largely by the forward detector and η_{max} cuts, but an additional factor needs to be applied to account for any residual events. This can be estimated from a sample of N diffractive events selected using only the requirement of $\eta_{max} < 1.8$. The resulting sample will contain components of elastic and dissociative events, N_e and N_d respectively. The forward cuts are then applied, with N_1 events passing and N_2 failing, where:

$$\begin{aligned} N_1 &= \varepsilon_e^1 N_e + \varepsilon_d^1 N_d \\ N_2 &= \varepsilon_e^2 N_e + \varepsilon_d^2 N_d \end{aligned} \tag{8.4}$$

with $\varepsilon_i^1 + \varepsilon_i^2 = 1$ for $i = e, d$. The RAPGAP Monte Carlo has, as yet, no facility for the simulation of dissociative processes, so the factors $\varepsilon_{e,d}^{1,2}$ are ascertained with a DIFVM sample. Equations 8.4 can then be solved simultaneously, from which a factor of 0.9 is obtained.

8.1.1 Bin Selection

The divisions in the kinematic volume are chosen to cover the largest possible kinematic region with a reasonable number of events in each whilst minimising the effects of the finite resolution of the measured variables.

Deviations in the measured kinematic variables from their true values can result in the smearing or migration of an event from its true bin to another, thus distorting the distribution. The resolution, therefore, imposes a lower limit on the size of the bin. In the case of x and Q^2 the resolution is $\lesssim 70\%$ of the chosen bin width.

The bins used in the low Q^2 analysis [43] follow closely those employed in the in the 1994 $F_2(x, Q^2)$ analysis [14] including the very low Q^2 region accessed with the shifted event vertex. Only three bins in Q^2 are used for the high Q^2 analysis reflecting the low level of statistics in the diffractive sample (~ 250 events) and the desire to reach as high a Q^2 region as possible in which meaningful measurements can be made. The lower Q^2 bin, centred at 140 Gev^2, extends from the highest bin attainable with the low Q^2 requirement of a fully reconstructed electron in the BEMC. The x and β bins correspond to those in [43] which are kinematically accessible, a factor governed largely by the upper limit placed on the value of the reconstructed y. This choice of binning in β does, however, result in resolutions of approximately the same size as the bin width, but is retained in order to make simple comparisons with previous work. This effect is accounted for in the smeared acceptance calculation. The divisions in the $x - Q^2$ plane are shown in figure 8.1 and the binning in β is listed in table 8.1 .

Bins which only contain one selected event are excluded from the analysis. Bins are also excluded if the smeared acceptance, A, is less then 25% or if the purity, the ratio the number of reconstructed events which originated in the bin to the total number reconstructed, is less than 10%.

β bin centre	β upper limit	β lower limit
0.10	0.14	0.07
0.20	0.30	0.14
0.40	0.50	0.30
0.65	0.80	0.50
0.90	1.20	0.80

Table 8.1: Choice of binning in β.

8.1.2 Systematic Uncertainties

Uncertainties in the Acceptance

The value of the acceptance in each bin is subject to the systematic effects of the limited statistics in the Monte Carlo from which it is calculated and the assumptions under which this description of the data is made. These uncertainties, along with the methods used for their evaluation, are listed below.

- Error due to the limited statistics in the Monte Carlo mixture used to parameterise the data. For each Monte Carlo component used in the parameterisation the number of events generated in each bin, N_g, is known, along with the number reconstructed which originated in that bin, N_s, the number which have migrated in, N_i, and thus the number lost or rejected, N_r, where $N_r = N_g - N_s$.

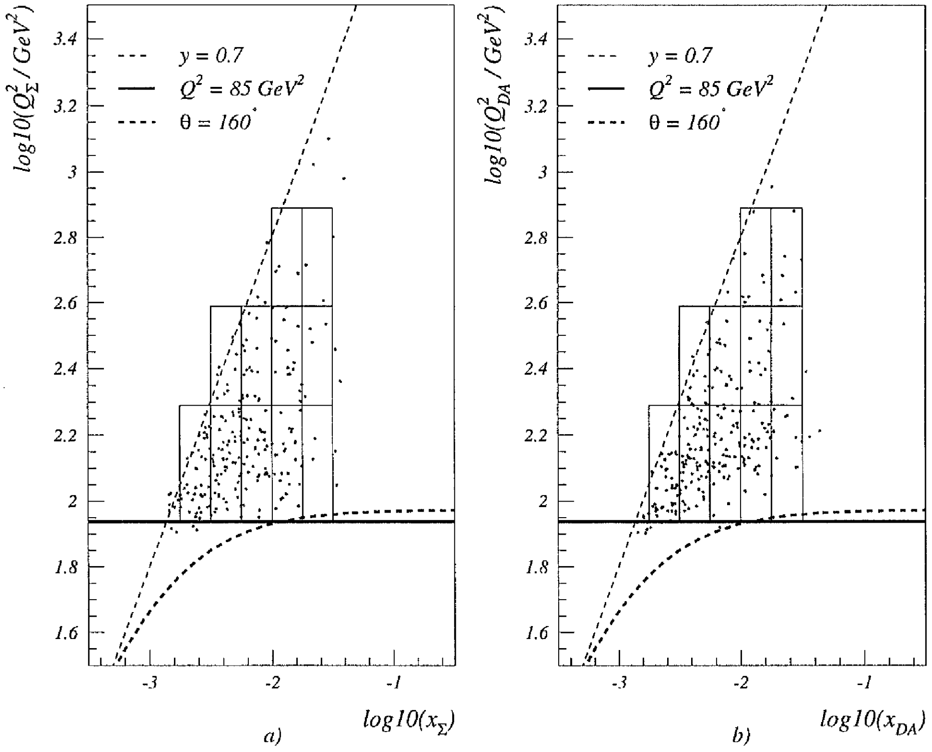

Figure 8.1: Distribution in the $x - Q^2$ plane of the events selected by the diffractive cuts with a) the Σ reconstruction method and b) the DA method. The boxes represent the bins used in the F_2^D analysis.

Each term carries a corresponding Poisson error. The acceptance can then be expressed as:

$$A = \frac{(n^{\mathbb{P}} N_i^{\mathbb{P}} + n^{\pi} N_i^{\pi} + n^D N_i^D) + (n^{\mathbb{P}} N_s^{\mathbb{P}} + n^{\pi} N_s^{\pi})}{(n^{\mathbb{P}} N_r^{\mathbb{P}} + n^{\pi} N_r^{\pi}) + (n^{\mathbb{P}} N_s^{\mathbb{P}} + n^{\pi} N_s^{\pi})} = \frac{N_i^{mix} + N_s^{mix}}{N_r^{mix} + N_s^{mix}} \tag{8.5}$$

where the superscripts $\mathbb{P}$, π, D refer to $\mathbb{P}$ exchange, pion exchange and DJANGO DIS respectively, and the terms $n^{\mathbb{P},\pi,D}$ represent the normalisation factors applied to each component. The statistical uncertainty is then estimated to be:

$$\begin{aligned} \sigma^2(A)^{stat} &= \left(\frac{1}{N_r^{mix} + N_s^{mix}}\right)^2 \sigma^2(N_i^{mix}) + \left(\frac{N_i^{mix} + N_s^{mix}}{(N_r^{mix} + N_s^{mix})^2}\right)^2 \sigma^2(N_r^{mix}) \\ &+ \left(\frac{1}{N_r^{mix} + N_s^{mix}} - \frac{N_i^{mix} + N_s^{mix}}{(N_r^{mix} + N_s^{mix})^2}\right)^2 \sigma^2(N_s^{mix}) \end{aligned} \tag{8.6}$$

It should be noted that this uncertainty is dominated by the effects of the low statistics afforded by the pion exchange sample in this region.

- Error due to the uncertainty in the $\mathbb{P}$ exchange/high $x_{\mathbb{P}}$ process ratio in the data. These proportions are set by the normalisation as described in section 7.4. The uncertainty is estimated as half the difference in the acceptance produced by increasing and decreasing the DJANGO/pion components by 50%. This then incorporates the uncertainty in the $\mathbb{P}$ exchange normalisation due to the statistical error on the data in the region of $x_{\mathbb{P}} < 0.0075$ and the possibility of DJANGO/pion events smearing into this range.

- Error in the ratio of pion exchange/DJANGO DIS chosen to describe the data, due to uncertainties in the fitting described in section 7.4. This uncertainty is predominantly a result of the statistical limitations of the data. It is included as a systematic error, however, as it effects all points. The following contributions are considered:

  - Uncertainty due to the choice of data distribution used for the fit. This is taken as half the difference in the acceptance measured using a pion exchange/DJANGO mixture found from the best fit to the data η_{max} distribution only and that from a fit to the $x_{\mathbb{P}}$ distribution only.

  - The number of bins in the diffractive data samples chosen with which to make the fit is found to effect the results of that fit. The choice of binning for the total DIS distributions has a negligible effect. The pion exchange/DJANGO ratio is found with best fits to 5 bins and only 1 bin in the diffractive spectra. The error is then estimated as half the difference in the acceptance found with these two ratios.

- The error due to the uncertainty in the assumed $x_{\mathbb{P}}$ distribution of the Monte Carlo. This is assessed by re-weighting the input $x_{\mathbb{P}}$ values by $x_{\mathbb{P}}^{\pm 0.2}$ and taking half the difference in the resultant acceptances.

- Error due to the assumed β dependence of the input Monte Carlo. The Monte Carlo cross section is re-weighted by the function:

$$\left(\frac{1}{g} - g\right)\beta + g \tag{8.7}$$

  with the two extreme possibilities within the limits imposed by previous data being obtained with $g = 0.75$ and $g = 1.33$. The nominal dependence is represented by $g = 1$. Again, half the difference between the acceptances calculated for each extreme case is taken as the uncertainty.

- Uncertainty due to the ignored t dependence in the input Monte Carlo. This is evaluated by re-weighting with the function:

$$e^{\pm 2t} \tag{8.8}$$

  following the form of the peripheral t dependency observed in soft pp collisions. As above, half the difference between the two acceptances thus produced is taken as the error.

- Uncertainty due to the assumptions made in the modelling of the $\mathbb{P}$ structure and the radiative corrections. The pattern of hadronisation is dependent upon the identity of the hard sub-process involved in the diffractive interaction. The efficiency of the diffractive selection thus depends upon whether the process was quark or gluon initiated. To estimate this effect the input $\mathbb{P}$ exchange Monte Carlo component (based on a predominantly gluonic $\mathbb{P}$) is replaced by a flat quark + flat gluon model, excluding higher order radiative corrections, representing the extreme possibility within the constraints imposed by previously collected data. The pion exchange/DJANGO proportions are retained.

The error is taken as the change in the acceptance resulting from this substitution. The low level of statistics obtained from the flat quark + flat gluon model in the signal region means, however, that any bin by bin behaviour is obscured due to random fluctuations and it is felt more appropriate to evaluate this effect as a global uncertainty in the normalisation.

Further Uncertainties

The following additional sources of systematic uncertainty are considered:

- Error due to the 5% uncertainty in the LAr hadronic energy scale. This affects the measurements made using the Σ method of reconstruction to a greater extent then those for the DA method, where uncertainty is only introduced in the calculation of M_x and thus $x_{\mathbb{P}}$. For each reconstruction method the resulting systematic error is evaluated bin by bin from the fractional change in the number of reconstructed Monte Carlo events following alteration of the energy scale to the limits of the uncertainty.
- Error due to the 3% uncertainty in the LAr electromagnetic energy scale. Evaluated as for the LAr hadronic uncertainty.
- Error due to the 20% uncertainty in the BEMC hadronic energy scale. Evaluated as above.
- Error due to a 3% uncertainty in the track energy scale. Determined as above.
- Error due to a potential shift of 2 mrad in the measured polar angle of the scattered electron, θ_e.
- Error due to residual non-*ep* background. This is estimated using the LAr and CJC timing criteria described in section 6.3.2 and applied as a global uncertainty in the normalisation.
- Error due to diffractive photoproduction background. The fraction of photoproduction events contaminating the diffractive sample is estimated to be equal to the fraction contaminating the total DIS sample (0.2%) as a diffractive event has no more or less chance of faking an electron then a standard photoproduction process.

Source of Uncertainty	Mean Error Value	
	Σ Method	DA Method
LAr hadronic energy Scale	4%	3%
LAr e.m energy scale	4%	1%
BEMC hadronic energy scale	2%	2%
Track energy scale	4%	3%
θ_e shift	1%	1%
M.C statistics	21%	27%
M.C $\mathbb{P}$/pion+DJANGO ratio	2%	4%
M.C pion/DJANGO ratio	2%	4%
M.C t dependence	5%	6%
M.C $x_{\mathbb{P}}$ dependence	3%	3%
M.C β dependence	3%	3%
M.C Modelling	10%	5%
Non-ep background	1%	1%
Photoproduction Background	0.2%	0.2%
p dissociation factor	2%	2%
Luminosity measurement	2%	2%
Global normalisation uncertainty	10%	6%
Bin-by-bin error	23%	29%
Total systematic error	26%	30%

Table 8.2: Summary table for the estimated systematic error arising from each of the sources listed in the text. Values are quoted for both kinematic reconstruction methods.

- Global error of 2% due to uncertainties in the luminosity measurement. These mainly arise from the limited efficiency of the luminosity system, the photon tagger energy scale and the satellite bunch correction.
- Global error of 2% due to the uncertainty in the value of the proton dissociation factor.

The mean values for the errors arising from each of the above sources are listed in table 8.2.

8.2 Results of the Measurement

The values obtained for $F_2^D(\beta, Q^2, x_{\mathbb{P}})$ are presented in figure 8.2. Excellent agreement is seen between those points evaluated using the DA reconstruction method and those for the Σ method. The highest Q^2 bin (centred at $Q^2 = 580$ GeV^2) elicits no useful information and is thus excluded from further analysis. A greater number of bins, particularly at $Q^2 = 300$ GeV^2, are accessed with the DA method than for the Σ method. As such, further analysis is concentrated on the data reconstructed with the DA method.

In all $\beta - Q^2$ bins the familiar decrease in the structure function with increasing $x_{\mathbb{P}}$ or x is seen. Following [39] the diffractive structure function is parameterised by the function:

$$F_2^D = \frac{f(\beta, Q^2)}{x_{\mathbb{P}}^n} \tag{8.9}$$

Here factorisation is assumed. A global fit is made to the measured values of $F_2^D(\beta, Q^2, x_{\mathbb{P}})$ allowing the intercept, $f(\beta, Q^2)$, to vary as a free parameter. Only those bins in $\beta - Q^2$ which contain more than one reconstructed $x_{\mathbb{P}}$ bin are included in the fit. For the DA method a best fit is achieved with the gradient $n = 1.08 \pm 0.21_{(stat.)} \pm 0.07_{(sys.)}$ ($\chi^2 = 0.82/n.d.f$)[1]. This compares with the value obtained from a similar fit to the Σ method reconstructed data of $1.28 \pm 0.20_{(stat.)} \pm 0.10_{(sys.)}$ ($\chi^2 = 0.38/n.d.f$)[2]. Both values are in agreement with the value of $1.19 \pm 0.06_{(stat.)} \pm 0.07_{(sys.)}$ from the 1993 low Q^2 measurement, described in section 4.10 and [39], in which reconstruction involved a combination of electron only and Σ methods. Within the framework of Regge Theory, such a dependence on $x_{\mathbb{P}}$ can be interpreted as the result of a leading Regge trajectory with an intercept of $\alpha(0) = 1.04 \pm 0.11_{(stat.)} \pm 0.04_{(sys.)}$ (from the DA measurement) or $\alpha(0) = 1.14 \pm 0.10_{(stat.)} \pm 0.05_{(sys.)}$ (from the Σ measurement), both of which are consistent with the leading trajectory which describes phenomenologically soft hadronic diffractive interactions, the soft $\mathbb{P}$, for which $\alpha(0) = 1.085$. The leading Regge trajectories for meson exchange are of the order of 0.5, therefore the majority of rapidity gap events observed in the high Q^2 sample can be interpreted as being due to the exchange of a $\mathbb{P}$ with an, as yet, undetermined contribution from the pion exchange mechanism.

There is, however, strong evidence to suggest that factorisation does not,

---

[1] $n.d.f = 27$

[2] $n.d.f = 20$

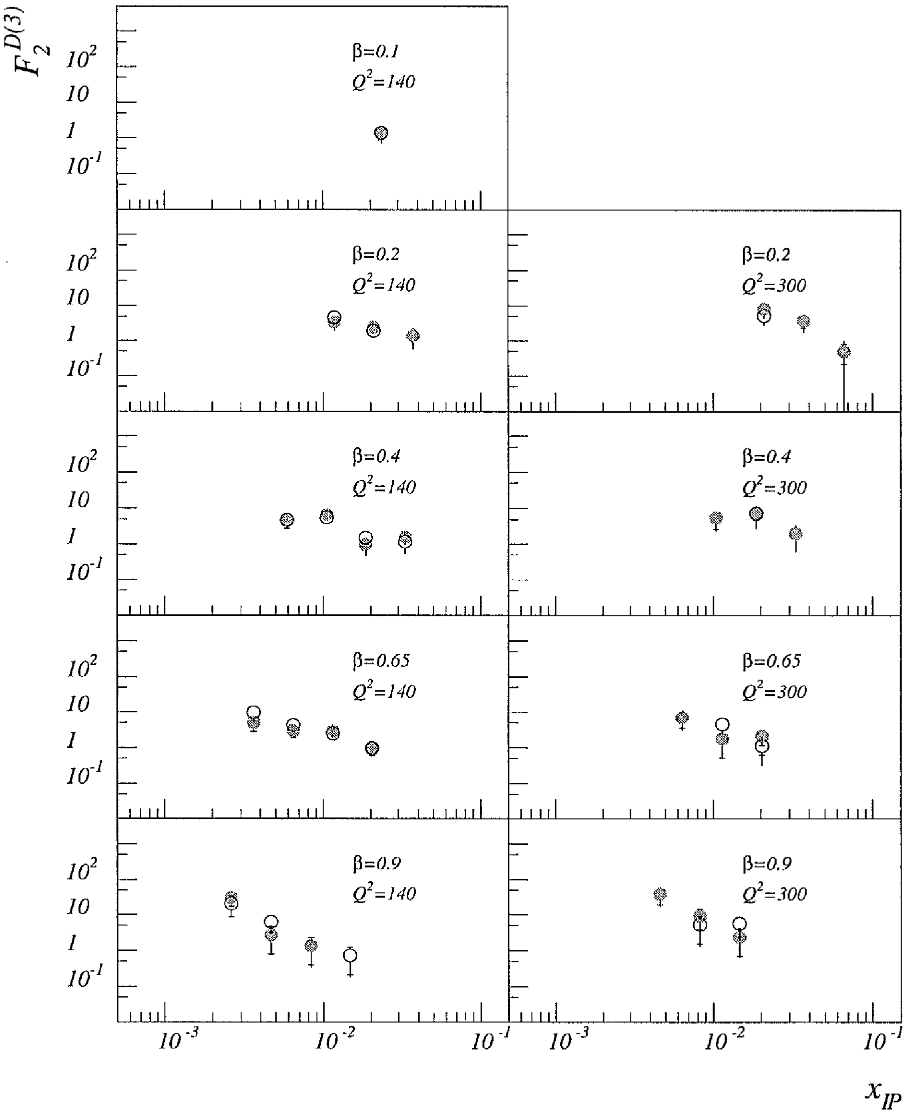

Figure 8.2: The diffractive proton structure function $F_2^D(\beta, Q^2, x_{\mathbb{P}})$ as a function of $x_{\mathbb{P}}$ in bins of β and Q^2. The open and solid circles represent data reconstructed with the Σ and DA methods respectively. The global normalisation uncertainty of 6% (10% for Σ) is not included.

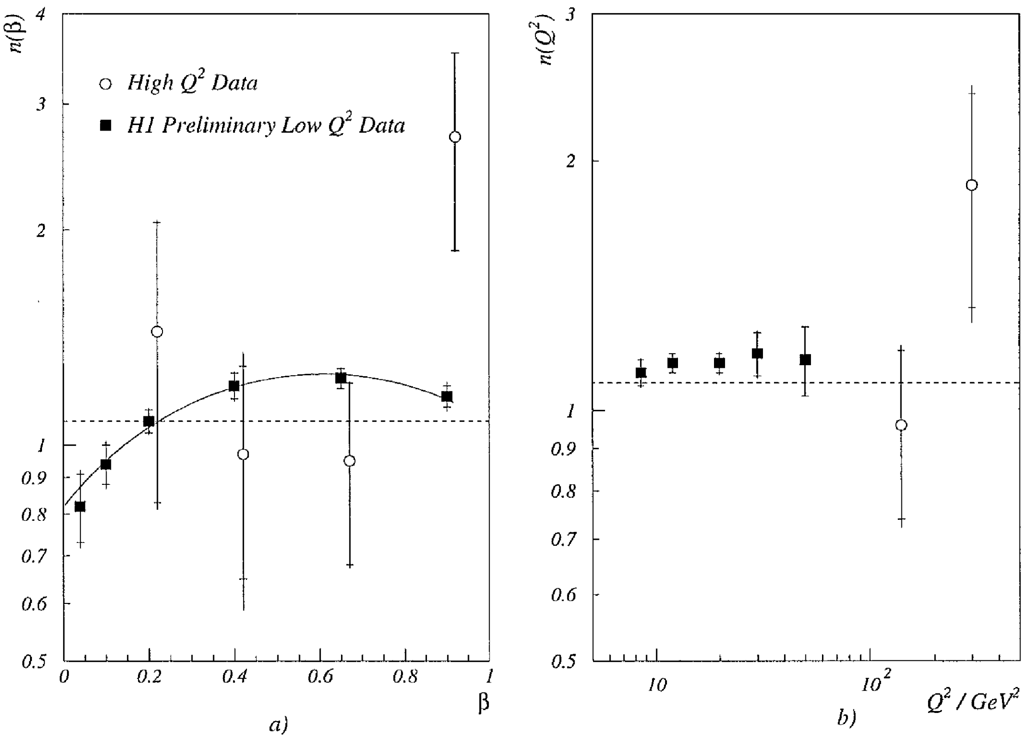

Figure 8.3: Variation of the slope n with a) β and b) Q^2. The low Q^2 data points are reconstructed with the Σ method, the high Q^2 with the DA method. The solid line in figure a) represents the best fit to the low Q^2 data as described in the text. The dashed line is the result of the fit to the high Q^2 data assuming that the ansatz of factorisation holds. The high Q^2 points in figure a) are offset by $\beta = +0.02$ for clarity.

in fact, hold. Figures 8.3 a) and b) show the variation in the gradient n with β and Q^2 respectively, for the high Q^2 diffractive events (DA method) and the H1 preliminary 1994 low Q^2 data (Σ method). A clear dependence on β can be seen in the low Q^2 case, which is parameterised by a quadratic fit of the form $a_1 + a_2\beta + a_3\beta^2$ for which the factors take the values:

$$\begin{aligned} a_1 &= 0.82 \pm 0.07_{(stat.)} \pm 0.05_{(sys.)} \\ a_2 &= 1.44 \pm 0.35_{(stat.)} \pm 0.22_{(sys.)} \\ a_3 &= -1.18 \pm 0.36_{(stat.)} \pm 0.22_{(sys.)} \end{aligned}$$

There would seem to be no significant dependence on Q^2. Such breaking of factorisation may be due to contributions from meson exchange (particularly pion exchange) at lower values of β, higher order $\mathbb{P}$ exchange or the effects of a two component structure as described in [36]. There is no reason to suspect that this dependence is altered as Q^2 increases to greater then 100 GeV^2. The low statistics in the high Q^2 sample, however, obscure any dependence on β with the points in figure 8.3 a) being broadly consistent with a constant n. There is an increase seen in the value of n at $Q^2 = 300$ GeV^2 in figure 8.3 b), but, with only two data points it is impossible to ascertain whether this is a genuine effect, such as an increase in the hard $\mathbb{P}$ contribution with Q^2 [31], or merely due to statistical fluctuation.

The best fits assuming factorisation ($n = 1.08$ for all bins) and assuming the quadratic dependence on β observed in the low Q^2 case are shown with the high Q^2 data in figure 8.4.

It is stressed that whether factorisation is assumed or not, the measured values of n do not exclude the possibility of contribution from the hard (BFKL) $\mathbb{P}$, with $\alpha(0) \sim 1.5$.

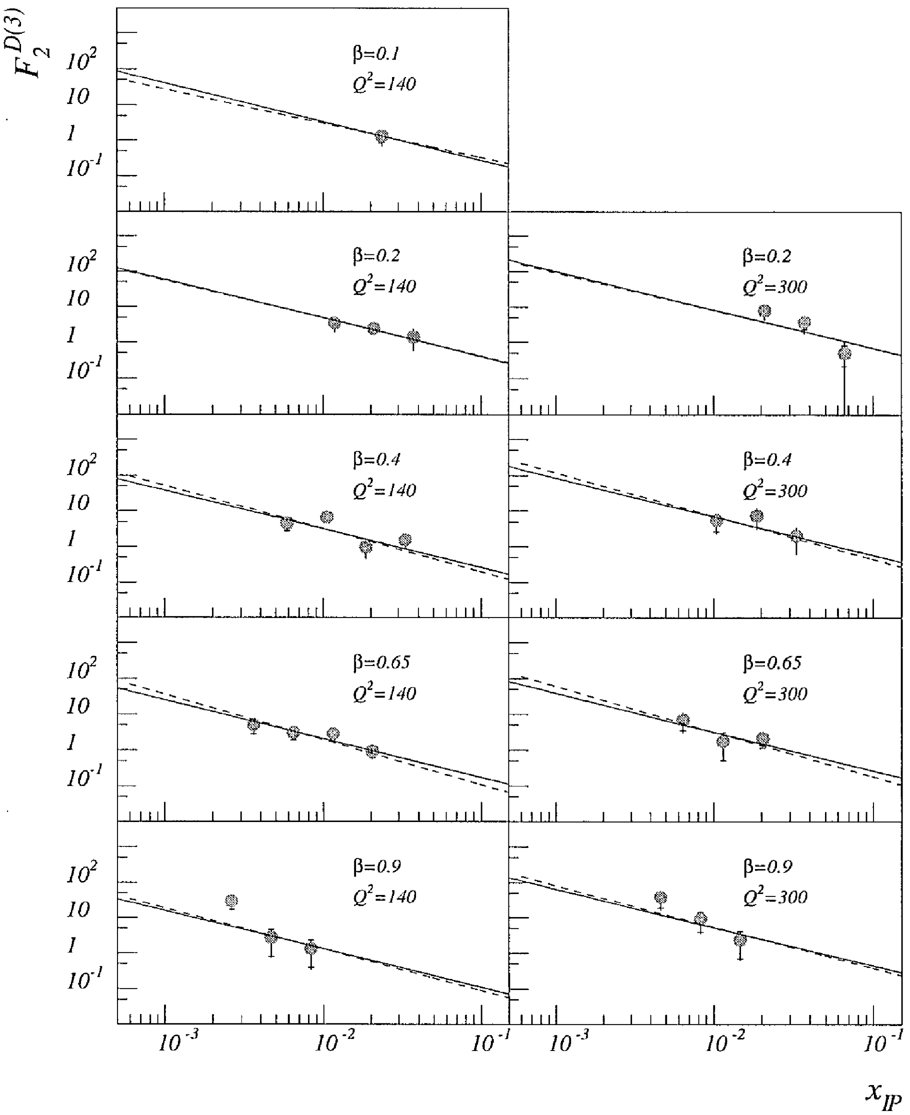

Figure 8.4: Parameterisation of F_2^D with the best fit to data assuming factorisation, represented by the solid line, and the fit obtained from the H1 preliminary low Q^2 data in which the breaking of factorisation is evident, denoted by the dashed line. The normalisation uncertainty of 6% is not shown.

8.3 The Pomeron Structure Function

That the dominant mechanism behind the rapidity gap phenomena is diffractive implies that the β and Q^2 dependence of $F_2^D(\beta, Q^2, x_{\mathbb{P}})$ is a measure of the $\mathbb{P}$ structure function. Under the assumption of factorisation, or at fixed β (assuming $F_2^D \propto x_{\mathbb{P}}^{-n(\beta)}$, as above), the pomeron structure function is then proportional to the integral $\tilde{F}_2^D(\beta, Q^2)$, where:

$$\begin{aligned} \tilde{F}_2^D(\beta, Q^2) &= \int_{x_{\mathbb{P}}^l}^{x_{\mathbb{P}}^h} F_2^D(\beta, Q^2, x_{\mathbb{P}}) dx_{\mathbb{P}} \\ &= \frac{f(\beta, Q^2)}{n(\beta)-1} \left((x_{\mathbb{P}}^l)^{-(n(\beta)-1)} - (x_{\mathbb{P}}^h)^{-(n(\beta)-1)} \right) \end{aligned} \quad (8.10)$$

where $x_{\mathbb{P}}^h = 0.05$ and $x_{\mathbb{P}}^l = 3 \times 10^{-4}$. The values of $\tilde{F}_2^D(\beta, Q^2)$ are obtained from fitting to the measured values of $F_2^D(\beta, Q^2, x_{\mathbb{P}})$ the function:

$$F_2^D(\beta, Q^2, x_{\mathbb{P}}) = \frac{n(\beta)-1}{\left((x_{\mathbb{P}}^l)^{-(n(\beta)-1)} - (x_{\mathbb{P}}^h)^{-(n(\beta)-1)} \right)} \cdot \frac{\tilde{F}_2^D(\beta, Q^2)}{x_{\mathbb{P}}^{n(\beta)}} \quad (8.11)$$

$\tilde{F}_2^D(\beta, Q^2)$ is evaluated for the high Q^2 data with n as a constant assuming factorisation and as a function of β following the form observed in the low Q^2 data. The values so calculated are presented in figures 8.5 and 8.6 along with the H1 preliminary low Q^2 points.

Clear variation of $\tilde{F}_2^D(\beta, Q^2)$ with Q^2 can be seen for all β in figures 8.5 a) and b). As such, violations in scale invariance, symptomatic of QCD, can be identified unambiguously. The low Q^2 data show an increase with $log(Q^2)$ at values of up to $\beta = 0.65$, to which excellent QCD fits based on a leading gluon exchange have been made [43]. In this scenario the gluon carries $\sim 80\%$ of the momentum of the $\mathbb{P}$. Agreement is seen between the form of $\tilde{F}_2^D(\beta, Q^2)$ calculated for the high Q^2 data under the assumption of factorisation and with n varying as a function of β. The high Q^2 points (with factorisation breaking) are consistent with the $log(Q^2)$ dependence of the low Q^2 data in all but the $\beta = 0.9$, $Q^2 = 300$ GeV^2 bin. Again with no further statistics available it is impossible to say if this is a true indication of the form of $\tilde{F}_2^D(\beta, Q^2)$ or not. Nevertheless, the rise observed with Q^2 at high β confirms the prediction of a gluon dominated $\mathbb{P}$.

A relatively flat dependence on β can be seen in figure 8.6 with a slight decrease in $\tilde{F}_2^D(\beta, Q^2)$ at high β, the effect of which becomes more exaggerated as Q^2 increases. A fit to the β dependence based on the expectation from the hard partonic models discussed in section 4.7 ($\propto \beta(1-\beta)$) is also shown. In this case the diffractive process involves the exchange of two or more gluons. Although the fit predicts the fall off at high β it is found to be inadequate for the $\beta \rightarrow 0$ region. Such a flat dependence at low β is to be expected in any QCD interpretation involving soft components of quarks and gluons [39]. The plots then imply a structure containing a hard component with a soft underlying quark/gluon sea as observed at low β, consistent with the leading gluon interpretation.

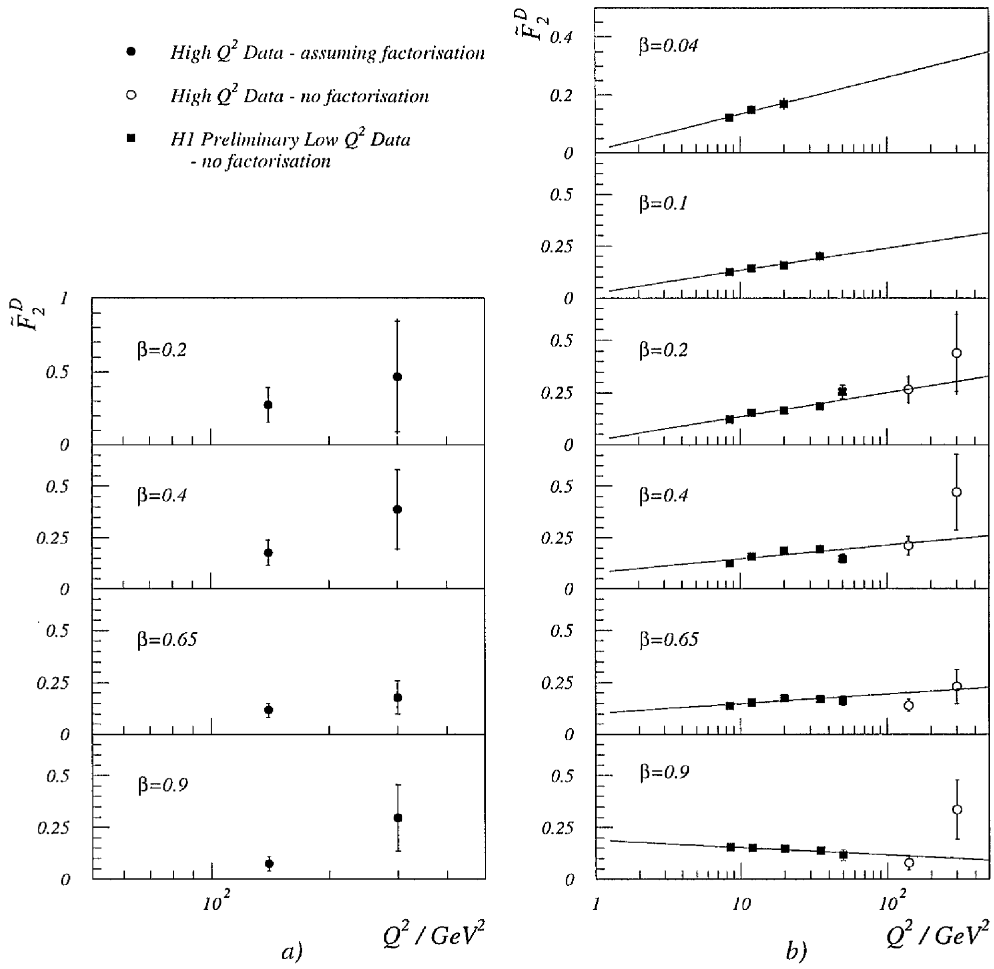

Figure 8.5: Dependence of $\tilde{F}_2^D(\beta, Q^2)$ on Q^2 with a) $\tilde{F}_2^D(\beta, Q^2)$ from the high Q^2 data calculated under the assumption of factorisation and b) from the low and high Q^2 data with n varying as a function of β as described in the text. The solid line represents a fit to a $log(Q^2)$ dependence.

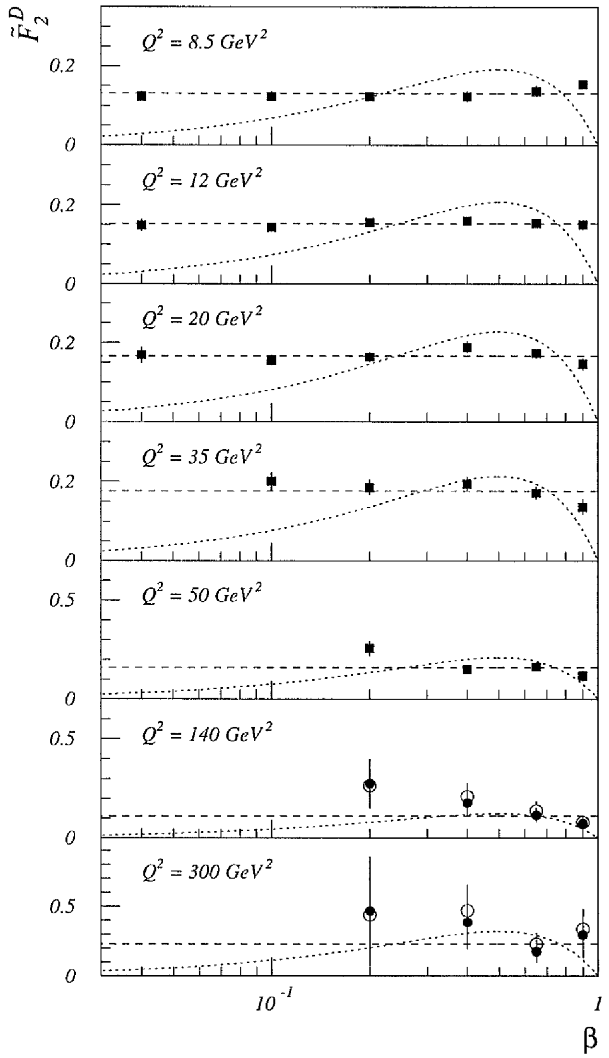

Figure 8.6: Dependence of $\tilde{F}_2^D(\beta, Q^2)$ on β, for the high Q^2 data assuming factorisation (solid circles) and with the breaking of factorisation following the form observed in the low Q^2 case (open circles). The H1 preliminary low Q^2 data are represented by the solid square markers. A fit assuming a constant dependence is denoted by the solid line along with a fit following a $\beta(1-\beta)$ dependence as predicted from hard partonic $\mathbb{P}$ models (dashed line).

Chapter 9

The Search for Charged Current Diffractive Events

9.1 Introduction

The wealth of evidence for a partonic structure within the $\mathbb{P}$ implies that diffractive processes mediated by the exchange of the charged $W^{\pm}$ bosons are possible. Assuming a gluon dominated structure, such an exchange would occur with the coupling of the $W^{\pm}$ to a soft quark within the valence sea of the $\mathbb{P}$ or via boson-gluon fusion, and is expected to be considerably suppressed.

With the limited CC statistics afforded by the luminosities so far achieved at HERA, the study of diffractive phenomena in the CC regime is constrained to be no more than a search for candidate events.

9.2 Modified Selection of the CC Sample

As discussed in section 6.2, insistence on a cut in the missing transverse momentum of $V > 25$ GeV imposes a limit of $Q^2 > 625$ GeV on the selected CC events. The number of diffractive NC DIS events observed on this Q^2 range is considerably suppressed, with no more than 0.5% satisfying the criteria from a DIS sample of some 800 events. As demonstrated in figure 3.3, at reasonable values of Q^2 ($< 10^4$ GeV) the NC DIS cross-section is an order of magnitude greater than that for the CC process. This implies that, given a CC sample of only 53 events, the chances of finding any of a diffractive nature are extremely small.

For this reason a modified selection is used, with a looser cut of $V > 10$ GeV and a consequential relaxation of the lower limit in Q^2 to 100 GeV. This results in a substantial increase in the *ep* background (figure 6.8) and additional cuts are required to reduce this.

9.2.1 The Selection Prescription

1. Trigger, vertex and run requirements as in section 6.2.
2. $V > 10$ GeV.
3. Non-*ep* background rejection using the topological finders and timing criteria described in section 6.3.
4. 'Electron' energy, $E_e < 8$ GeV, where electron candidates are located with the algorithm outlined in 5.4.2.
5. $E_{etag} = 0$ GeV, where E_{etag} is the measured energy deposit in the electron tagger.

A total of 4002 events survive the first two listed criteria. The LAr and CJC timing for these events is shown in figure 9.1 and the results of the topological and timing categorisation are summarised in table 9.1. From this an estimate of the remaining non-*ep* contamination, following rejection of non-prompt and non-CC class events, of $(1215 \times 74)/2127 = 43 \pm 5$ is made.

The electron finding routine is applied in order to reject high Q^2 NC background. The efficiency of the finder as a discriminater for CC events, where no electron should be found, is tested using a DJANGO CC Monte Carlo sample. The cut of $E_e < 8$ GeV rejects $2.7 \pm 0.4\%$ of the sample following the application of all other CC criteria. Tagged photoproduction events are removed with the cut imposed on E_{etag}. A total of 46 data events are rejected. The loss in the CC data, as assessed by the Monte Carlo, is negligible.

The resulting data set contains 285 events, comprising 247 e^+p and 38 e^-p interactions. It should be noted that this is still expected to be background dominated. The number of genuine CC events in the sample can be estimated following the polynomial parameterisation, described in section 6.5.1, of the e^+p and e^-p DJANGO CC Monte Carlos. After application of all the above cuts, integration of the polynomial fits to the Monte Carlo V distributions imply a total of 30 ± 8 e^+p and 5 ± 6 e^-p additional CC events in the range $10 < V < 25$ GeV i.e. 88 ± 12 events in the whole data sample.

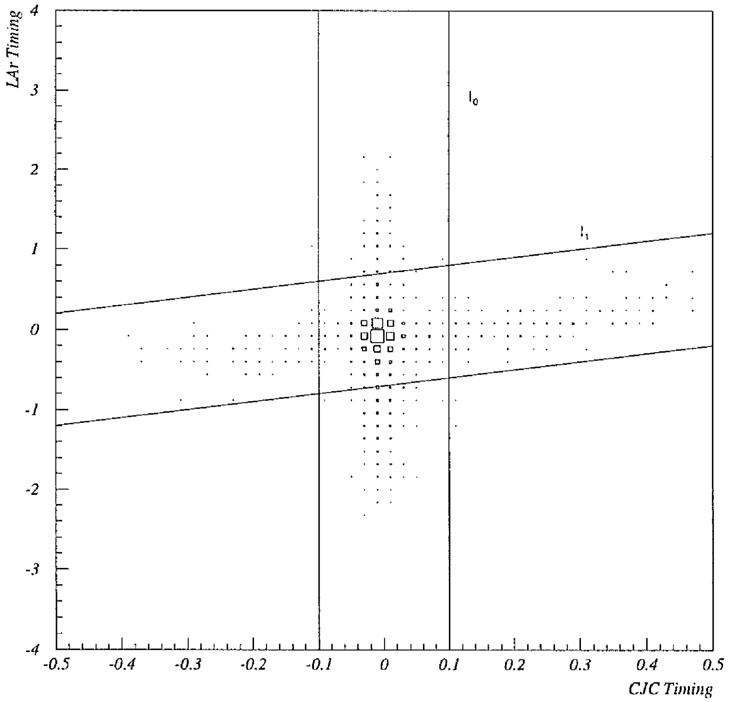

Figure 9.1: LAr timing against CJC timing in units of time for one bunch crossing for all selected events with $V > 10$ GeV.

Event Classification	All	P	S	C	U
All	4002	1801	879	1185	137
Halo	1713	787	723	115	88
Cosmic	1629	428	133	1021	47
CC Class	660	586	23	49	2

Table 9.1: Topological and timing classification for the $V > 10$ GeV CC selected events.

9.3 Diffractive Event Selection

The selection proceeds in the same way as for the NC DIS case with the addition of a visual scan to confirm the selection of any event. The cuts are applied as follows:

- Forward detector cuts.
- $\eta_{max} < 3.2$.
- $x_{\mathbb{P}} < 0.05$.
- Visual scan.

The selection results are summarised in table 9.2. The 6 events surviving all cuts are visually scanned, the results of which are as follows:

- 3 cosmic muon events with clear energy deposits in each side of the Tail Catcher.
- 1 beam halo overlay event.
- 1 misidentified NC event where an isolated track corresponding to the scattered positron points directly to the BBE-LAr Barrel crack.
- 1 CC candidate event, the classification of which is in agreement with the results of three independent scans [66].

	No. of Events Surviving Cut	
Cut	positron-proton	electron-proton
Forward Detector Cuts	14	6
η_{max} Cut	8	3
$X_{\mathbb{P}}$ Cut	4	2
Visual Scan	1	0

Table 9.2: Summary of the results of the CC diffractive selection procedure.

9.4 The Candidate Event

An event display of the one event selected from the final visual scan is shown in figure 9.2, with the measured event properties listed in table 9.3. There is one prominent cluster in the LAr calorimeter, with a centre of mass at $x = 8.6$ cm, $y = 170.1$ cm, $z = -46.4$cm, representing a total energy deposition of $22.8 \pm 2.0 \pm 0.7$ GeV; determined from the summation of all cell energies in the cluster with the systematic error corresponding to the uncertainty of 5% in the hadronic energy scale. The cluster is matched in $\theta - \phi$ space to a cluster reconstructed in the Tail Catcher, thus corresponding to a depth of $> 5\lambda$, indicative of a purely hadronic jet. The spatial distribution of the energy is inconsistent with that expected from cosmic showering with an increasing lateral dispersion with r. A second cluster (c.o.g at $x = 6.2, y = 37.3, z = 362.1$ cm) defines the border of the apparent rapidity gap. Extending to a depth of $\lesssim 4\lambda$, the cell distribution is again strongly suggestive of a hadronic jet. With no visible scattered positron there is a clear imbalance in the transverse momentum of the final state, particularly evident in the radial view of figure 9.2.

The event display shows activity in two cells of the third layer of the Plug. The total energy deposited in this component is measured at 0.18 GeV, well below the limit of 3 GeV, and is thus wholly consistent with detector or electronic noise. There are no paired hits in the FMD and no activity in the forward Iron endcap or the proton tagger.

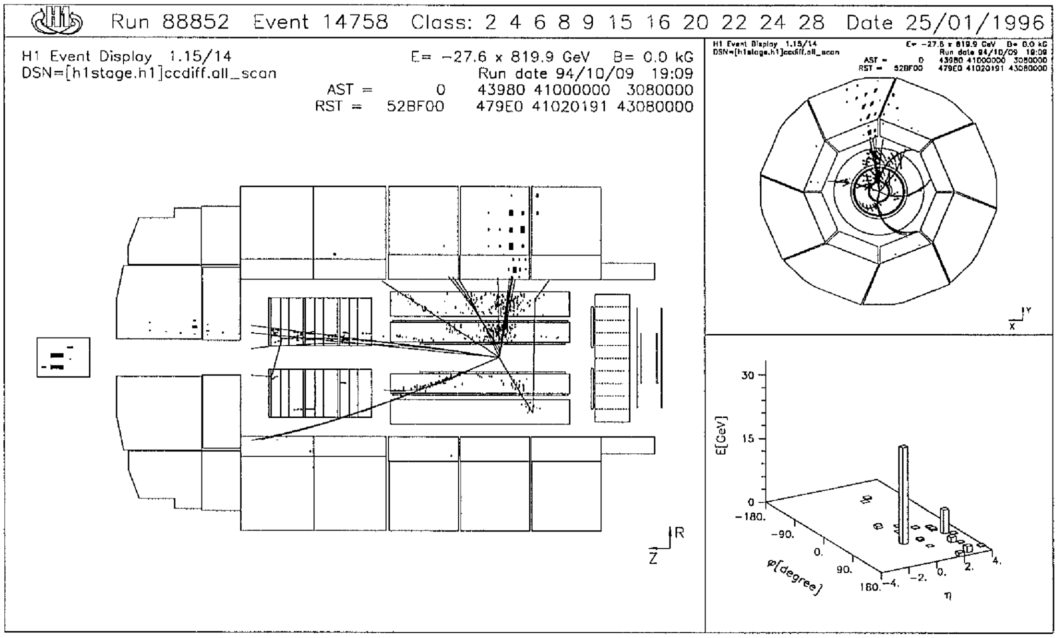

Figure 9.2: The CC diffractive candidate event.

Global Event Properties	
Q^2	$1100 \pm 170 \pm 160$ GeV^2
x	$0.025 \pm 0.004 \pm 0.003$
V	$23.6 \pm 1.4 \pm 0.9$ GeV
M_x	$23.6 \pm 2.5 \pm 1.0$ GeV
β	$0.66 \pm 0.16 \pm 0.02$
$x_{\mathbb{P}}$	$0.037 \pm 0.011 \pm 0.003$
η_{max}	2.99 ± 0.01
Hadronic Cluster 1:	
Transverse Momentum	$22.0 \pm 1.4 \pm 0.9$ GeV
Polar Angle	$105.3 \pm 0.5^\circ$
Electromagnetic Fraction	0.42
Hadronic Cluster 2:	
Transverse Momentum	$0.57 \pm 0.06 \pm 0.02$ GeV
Polar Angle	$6.0 \pm 0.5^\circ$
Electromagnetic Fraction	0.50

Table 9.3: The Kinematics of the Candidate Event.

9.5 Background Levels

The most likely background source to the process of CC diffraction is the smearing down of non-diffractive high $x_{\mathbb{P}}$ CC events into the signal region. The extent to which this can occur is assessed using the DJANGO generated standard e^+p CC sample.

Following all CC selection cuts 1945 events remain from a Monte Carlo sample of 5000 events. The spectra for the relevant diffractive variables, $x_{\mathbb{P}}$, β etc. are shown in figure 9.3. A total of 12 events satisfy all diffractive criteria. Normalisation of the sample to the predicted 71 ± 10 events in the data suggests a total background of 0.4 ± 0.1 events.

The level of photoproduction background can be estimated with the control sample used for standard CC background studies described in section 6.5.1. With the exclusion of the candidate event, only one event from the control sample which has not previously been identified as a cosmic interaction, survives all diffractive cuts. The event has a missing transverse momentum of $V = 12.1$ GeV which, considering the exponential form of the photoproduction distribution, suggests that such background in the kinematic region of the candidate event ($V > 20$ GeV) is negligible.

9.6 Limits to the Diffractive CC Cross Section

The upper limit to the elastic cross section for CC diffractive processes in e^+p collisions, σ_{UL}, can be set at the 95% confidence level using the formula:

$$\sigma_{UL}(e^p \rightarrow \overline{\nu}_e pX) = \frac{N}{\epsilon\mathcal{L}} \cdot f_{pdiss} \cdot f_{noise} \tag{9.1}$$

where ϵ represents any detector and selection inefficiencies, $\mathcal{L}$ the luminosity, f_{pdiss} the proton dissociation correction factor, f_{noise} the noise correction factor and N is defined by the general Poisson formula [67]:

$$0.95 = 1 - \frac{e^{-(\mu_B+N)} \sum_{n=0}^{n_0} \frac{(\mu_B+N)^n}{n!}}{e^{-\mu_B} \sum_{n=0}^{n_0} \frac{\mu_B^n}{n!}} \tag{9.2}$$

for the observation of n_0 events with a predicted background of μ_B. Therefore, with 1 candidate event and a background level of 0.4 events, $N = 4.42$. The error of ± 0.1 on this background level introduces a systematic error on N of ± 0.12. This is included in the final quoted upper limit.

The global inefficiency factor ϵ is calculated with generated CC diffractive events. With no data available for this process, and indeed no firm proof that it actually exists, generation requires that assumptions based upon NC DIS findings and standard CC measurements must be made. In order to account for any systematic errors inherent in such assumptions, two separate Monte Carlos samples using different parameterisations of the diffractive structure are employed:

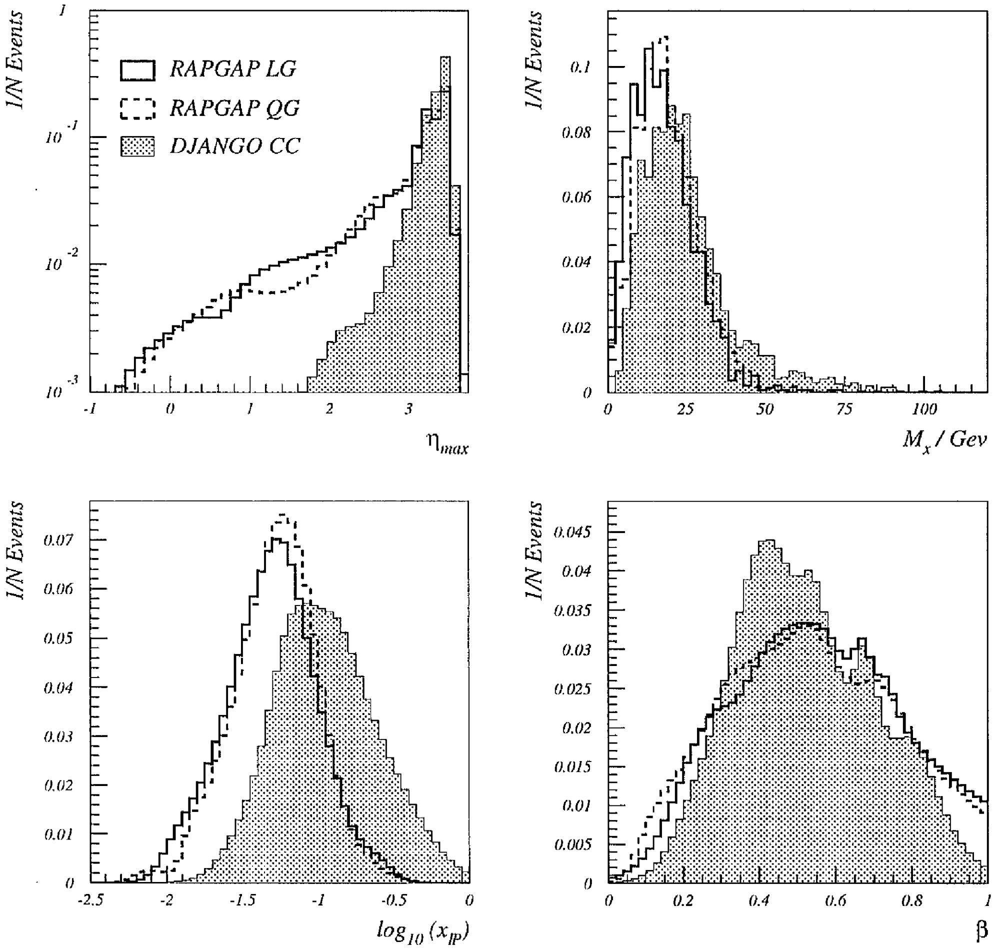

Figure 9.3: Comparison of the spectra of the diffractive variables for the generated diffractive CC samples (LG and QG, described in the text) and the standard CC DJANGO generated sample.

Analysis Step	Efficiency RAPGAP LG	Efficiency RAPGAP QG
CC Trigger	0.70 ± 0.02	0.72 ± 0.02
V Cut	$0.80 \pm 0.02 \pm 0.03$	$0.79 \pm 0.2 \pm 0.03$
Vertex	0.89 ± 0.02	0.89 ± 0.02
CC Selection	0.91 ± 0.03	0.91 ± 0.03
Forward Detector Cuts	0.68 ± 0.02	0.66 ± 0.02
η_{max} Cut	0.49 ± 0.02	0.49 ± 0.02
$x_{\mathbb{P}}$ Cut	$0.67 \pm 0.02 \pm 0.03$	$0.63 \pm 0.02 \pm 0.04$
Global ϵ	$0.21 \pm 0.01 \pm 0.01$	$0.19 \pm 0.01 \pm 0.01$

Table 9.4: Efficiencies for each analysis step for the selection of CC diffractive processes.

- RAPGAP LG: including a QCD Leading Gluon parameterisation based upon fits the 1994 H1 preliminary low Q^2 data.
- RAPGAP QG: incorporating a flatter gluon distribution, with the quark component of the $\mathbb{P}$ representing the maximum allowed within the limits of the 1994 data.

Both simulations include higher order radiative corrections. All input kinematics are chosen to match those of the DJANGO standard CC generation.

The inefficiencies for each analysis step as calculated with the diffractive CC Monte Carlos, are summarised in table 9.4. The errors quoted correspond to the limited statistics of the Monte Carlo samples (each 5000 events) and, in the case of the cuts on $x_{\mathbb{P}}$ and V, the effects of the 5% systematic uncertainty in the hadronic energy scale. The total acceptance is calculated to be extremely low ($\sim$ 20%), largely due to the loss of events arising from the diffractive selection cuts. The major contributing factor to this loss is the $\eta_{max} < 3.2$ requirement, the effect of which can be understood in terms of the QPM (section 3.4.1). The direction of the scattered parton in the QPM can be expressed as:

$$\eta = \frac{1}{2} log \left[\frac{E_p}{E} . \left(\frac{xs}{Q^2} - 1 \right) .x \right] \tag{9.3}$$

Thus, at the high values of x preferentially occupied by the CC events (for which $Q^2 \gg 100$ GeV) there is more hadronic activity in the forward direction than

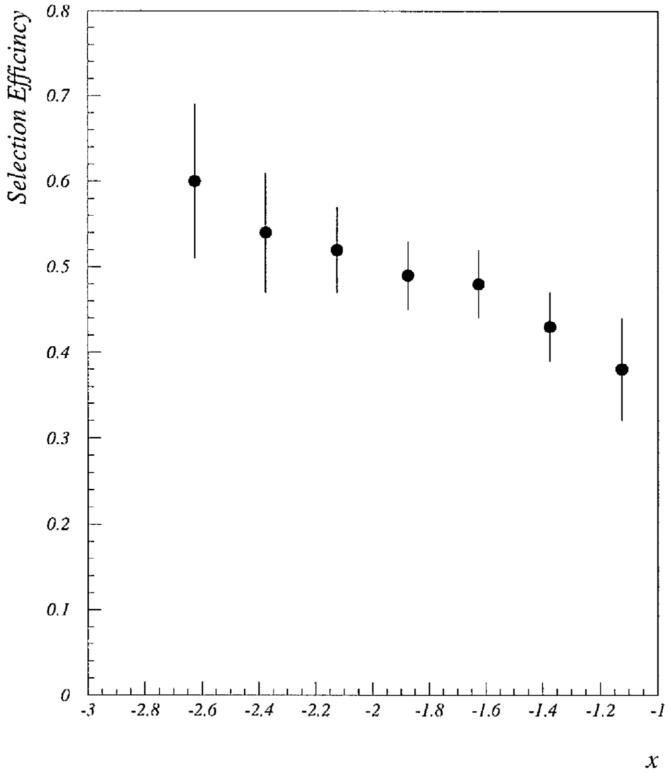

Figure 9.4: Efficiency of $\eta_{max} < 3.2$ requirement for the RAPGAP LG CC diffractive Monte Carlo with $V_{gen} > 10$ GeV.

for low x processes. The consequent reduction in the selection efficiency of the η_{max} requirement with x can be seen in figure 9.4. Such suppression of the size of the effective rapidity gap in the CC diffractive process also provides an explanation for the relatively poor performances of the $x_{\mathbb{P}}$ and forward detector cuts. The $\approx 70\%$ trigger efficiency is a direct consequence of the reduction in the missing transverse momentum requirement as demonstrated in figure 6.2.

Agreement is seen between the global ϵ values calculated from each Monte Carlo sample. As such, the mid-point between the two values is taken as the effective correction factor: $\epsilon = 0.20 \pm 0.01 \pm 0.01$.

The upper limit on the cross section for the elastic e^+p CC diffractive process in the region $V > 10$ GeV with one candidate observed from an integrated luminosity of $\mathcal{L} = 2.70 \pm 0.05$ pb^{-1} is then calculated as:

$$\sigma(e^+p \rightarrow \overline{\nu}_e pX \,|\, V > 10\,\mathrm{GeV}) \;=\; 8.0 \pm 0.6_{(sys.)}\,\mathrm{pb} \qquad (9.4)$$

The systematic error is the result of the uncertainties in each term of equation 9.1. The error could be incorporated into the limit to produce a single figure with a Bayesian approach [68]. However, as this makes assumptions on the true distribution of CC diffractive events, it is felt to be inappropriate. This limit compares with the cross section calculated from the estimated 71±10 standard CC events in the $V > 10$ GeV kinematic region of:

$$\sigma(e^+p \rightarrow \overline{\nu}_e X \,|\, V > 10\,\mathrm{GeV}) \;=\; 49.7 \pm 7.2_{(stat.)} \pm 3.1_{(sys.)}\,\mathrm{pb} \qquad (9.5)$$

where the selection efficiency is calculated from a standard DJANGO CC Monte Carlo to be 0.52 ± 0.03.

The upper limit to $\sigma(e^+p \rightarrow \overline{\nu}_e pX \mid V > 10\,\mathrm{GeV})$ would seem rather high in relation to the cross section for genuine CC events when compared with the ratio of diffractive to standard NC DIS processes. However, with only one candidate event, which has a $\sim 27\%$ probability of being a standard CC process, this measurement may well be more a reflection of the inefficiency of the selection procedure than of any new physics processes involved.

Chapter 10

Summary

For the first time diffractive processes have are investigated in the regime of high Q^2 NC DIS, where the scattered electron is located in the LAr calorimeter or the BEMC-BBE transition region. Following the identification of the scattered electron and imposition of cuts to remove background processes a sample of some 250 putative diffractive events are selected using the forward detectors and a calorimeter η_{max} cut.

Monte Carlo comparisons reveal that a mixture of diffractive interactions and standard DIS background events is insufficient to describe the data, particularly in the region of high $x_{\mathbb{P}}$. A further contribution from the pion exchange process would seem to be required in order to obtain a faithful representation of the data.

With this three component description of the data the limited form of the diffractive proton structure function $F_2^D(\beta, Q^2, x_{\mathbb{P}})$ is measured over the kinematic range $140 \leq Q^2 \leq 300$ GeV^2, $2.37\times10^{-3} \leq x \leq 0.0133$ and $0.1 \leq \beta \leq 0.9$. Under the assumption of factorisation the dependence of $F_2^D(\beta, Q^2, x_{\mathbb{P}})$ on $x_{\mathbb{P}}$ is parameterised by the form $x_{\mathbb{P}}^{-n}$, where $n = 1.08 \pm 0.21_{(stat.)} \pm 0.07_{(sys.)}$ as measured from data reconstructed using the DA method and $n = 1.28 \pm 0.20_{(stat.)} \pm 0.10_{(sys.)}$ as obtained from the Σ method. In both cases the measurement is in agreement with that from previous studies involving diffractive DIS interactions in the range $8.5 \leq Q^2 \leq 50$ GeV^2. Within the framework of the Regge Theory of hadronic interactions, such dependences on $x_{\mathbb{P}}$ corresponds to the intercepts $\alpha(0) = 1.04 \pm 0.11_{(stat.)} \pm 0.04_{(sys.)}$ (DA) and $\alpha(0) = 1.14 \pm 0.10_{(stat.)} \pm 0.05_{(sys.)}$ (Σ) of the leading Regge trajectory.

Both values are consistent with that of the soft $\mathbb{P}$ trajectory, and far higher than the intercepts predicted for meson exchange ($\alpha(0) \sim 0.5$) and pion exchange $\alpha(0) \sim 0$. As such, the dominant mechanism for the production of the rapidity gap events in the high Q^2 sample can be identified as diffractive.

Violations of factorisation can, however, be clearly observed in the 1994 low Q^2 measurements of $F_2^D(\beta, Q^2, x_{\mathbb{P}})$. Here, the exponent n is seen to vary as a quadratic function of β. There is no obvious dependence on Q^2. The limited statistics of the high Q^2 sample, however, obscure any such effect, with the dependence of n on β remaining consistent with a constant. A rise in the exponent is seen at $Q^2 = 300$ GeV^2, but with only two Q^2 bins it is impossible to draw any conclusions from this observation. Whether factorisation is assumed or not the possibility of a contribution from the hard BFKL $\mathbb{P}$ cannot be excluded.

The function $\tilde{F}_2^D(\beta, Q^2)$, a measure of the deep inelastic structure of the $\mathbb{P}$, is calculated both under the assumption of factorisation and following the quadratic β dependence found in the low Q^2 case. Unambiguous violations of scale invariance , symptomatic of QCD, are observed, the data being consistent with a linear $log(Q^2)$ dependence. $\tilde{F}_2^D(\beta, Q^2)$ is seen to rise with Q^2 up to $\beta = 0.65$, which, through analogy with the contrasting behaviour of the proton structure function, can be seen as evidence for a highly gluonic $\mathbb{P}$. A relatively flat dependence on β is observed.

Evidence for the diffractive process is sought in the CC regime using the same selection criteria as for the NC DIS case. One candidate event satisfying all requirements and inconsistent with non-ep background is located, from which the upper limit to the diffractive e^+p CC cross section is calculated to be $\sigma_{UL}(e^+p \rightarrow \overline{\nu}_e pX \mid V > 10\,\mathrm{GeV}) = 8.0 \pm 0.6_{(sys.)}$ pb.

The lack of a high level of data currently imposes severe limitations on any diffractive analysis in the high Q^2 regime, and conclusions can only be reached through comparison with the measurements made from previous low Q^2 studies. It is to be hoped, however, that with the improved luminosities anticipated over the next few years at H1, the behaviour of high Q^2 diffractive processes will be revealed with ever increasing clarity.

References

[1] H1 Calorimeter Group. *NIM*, **A336**:460, (1993).

[2] H. Wellisch et al. *Hadronic Calibration of the H1 LAr Calorimeter using Software Weighting Techniques.* (H1-02/94-346), (1994).

[3] H1 Calorimeter Group. *NIM*, **A336**:499, (1993).

[4] S. Kermiche and J. Marks. *LAr Electromagnetic Energy Scale Studies usng NC DIS (1+1) Jet and QED Compton Events for the* e^+p *1994 H1 Data.* (H1-12/95-466), (1995).

[5] H1 Collaboration. *The H1 Detector at HERA.* (93-103), July (1993).

[6] A. Panitch. *Energy Calibration and Resolution in the BEMC.* (H1-08/95-449), (1995).

[7] H.I Cronström et al. *NIM*, **A340**:304–308, (1994).

[8] H1 Collaboration. *Measurement of the* Q^2 *dependence of the Charged and Neutral Current Cross Sections in* $e^{\pm}p$ *Scattering at HERA.* (96-046), March (1996).

[9] J.D. Bjorken. *Phys. Rev.*, **163**:1767, (1967).

[10] J. Friedman and H.Kendall. *Ann. Rev. Nucl. Sci*, **22**:203, (1972).

[11] C. Franzinetti. *6th International Symposium on Electron and Photon Interactions at High Energy*,pub. North Holland. page 353, (1973).

[12] G. Altarelli and G. Parisi. *Nucl. Phys.*, **126**:298, (1977).

[13] Y.L. Dokshitser. *Sov. Phys. JETP*, **18**:641, (1977).

[14] H1 Collaboration. *A Measurement and QCD Analysis of the Proton Structure Function $F_2(x, Q^2)$ at HERA.* (96-039), March (1996).

[15] J.J. Sakuri. *Phys. Rev. Lett.*, **22**:981, (19690).

[16] H. Spiesberger G.A. Schuler. *Proceedings of the Workshop Physics at HERA, Vol. 3.* page 1419, Oct (1991).

[17] A. Kwiatkowski, H. Spiesberger and H.-J. Möhring. *Proceedings of the Workshop Physics at HERA, Vol. 3.* page 1294, Oct (1991).

[18] G. Ingelman. *Proceedings of the Workshop Physics at HERA, Vol. 3.* page 1366, Oct (1991).

[19] L. Lönnblad. *Comput. Phys.*, **71**:15, (1992).

[20] T. Sjöstrand. *Comp. Phys. Comm.*, **82**:74, (1994).

[21] ZEUS Collaboration. *Phys. Lett.*, **B315**:481, (1993).

[22] H1 Collaboration. *Nucl. Phys.*, **B429**:477, (1994).

[23] T. Regge. *Nuov. Cim.*, **14**:951, (1959).

[24] P.D.B. Collins and E. Squires. *An Introduction to Regge Theory and High Energy Physics*, Cambridge University Press, Cambridge. (1977).

[25] P.D.B. Collins and A.D. Martin. *Hadron Interactions*, Adam Hilger Ltd., Bristol. (1984).

[26] E.L. Berger et al. *Nucl. Phys.*, **B286**:704, (1987).

[27] G. Ingelman and K. Janson-Prytz. *Proceedings of the Workshop Physics at HERA*, vol. 1.

[28] K.H. Streng. *Proceedings of the Workshop Physics at HERA*, vol. 1.

[29] J.B. Dainton. *Deep-Inelastic Electron-Proton Diffraction*, talk presented at the VI Blois Workshop "Frontiers in Strong Interactions", Château de Blois,France. June (1995).

[30] A. Donnachie and P.V. Landshoff. *Phys. Lett.*, **B191**:309, (1987).

[31] P.V Landshoff. *The Two Pomerons*, University of Cambridge, Preprint. (**HEP-PH/9410250**), (1994).

[32] G. Ingelman and P.E. Schlein. *Phys. Lett.*, **B152**:256, (1985).

[33] D.A. Ross. *The Perturbative Pomeron and Physics at Low-x*, talk presented at the Institute of Physics Annual Meeting, Imperial College, London. April (1996).

[34] L.N. Lipatov. *Sov. Phys. JETP*, **63**:904, (1986).

[35] J.C Collins and P.V. Landshoff. *Phys. Lett.*, **B276**:196, (1992).

[36] M. Genovese, N.N Nikolaev and B.G Zakharov. *Diffractive DIS from the Generalized BFKL Pomeron. Predictions for HERA.* Jülich Preprint. **KFA-IKP(TH)-25**, (1994).

[37] H. Holtmann, A. Szczurek and J. Speth. Jülich preprint, submitted to Phys. Rev. D. **KFA-IKP(TH)-25**, (1994).

[38] H. Holtmann et al. *Phys.Lett.*, **B338**:363–368, (1994).

[39] H1 Collaboration. *Phys.Lett.*, **B348**:681–696, (1995).

[40] H1 Collaboration. *Phys. Lett.*, **B338**:507, (1994).

[41] J.P. Phillips for the H1 and ZEUS Collaborations. *Rapidity Gap Events at HERA and the Structure of the Pomeron*, talk presented at the Workshop on Deep Inelastic Scattering and QCD, Paris, France. April (1995).

[42] H. Jung. *Comp. Phys. Comm*, **86**:147, (1995).

[43] A. Mehta for the H1 Collaboration. *New Results on Diffractive Deep Inelastic Scattering*, talk presented at the Topical Conference on Hard Diffractive Processes, Eilat, Israel. February (1996).

[44] B. List. *Diplomarbeit: Diffraktive J/ψ -Production in Elecktron-Proton-Stößen am Speicherrung HERA.* (H1-10/93-319), (1993).

[45] F. Charles et al. *Photoproduction as Background in Deep Inelastic Scattering a Low x.* (H1-09/94-380), (1994).

[46] Z. Zhang et al. *A Measurement of* $F_2(x, Q^2)$ *with the 1993 Data at High* Q^2 *Region.* (H1-09/94-379), (1994).

[47] A. De Roeck et al. *Analysis II of the 1992 Data of the Structure Function* $F_2(x, Q^2)$. (H1-12/93-332), (1993).

[48] A. Blondel and F. Jacquet. *Proceedings of the study of an ep facility for Europe.* (79/48):391–394, (1979).

[49] U. Bassler and G. Bernardi. *On the Kinematic Reconstruction of Deep Inelastic Scattering at HERA.* (94-231), July (1994).

[50] S. Bentvelsen et al. *Proceedings of the Workshop Physics at HERA*, vol. 1.

[51] C. Hoeger. *Proceedings of the Workshop Physics at HERA*, vol. 1. 1:43, Oct (1991).

[52] U. Bassler et al. *A Global DIS Event Selection for the 1993 Structure Function Measurement*, ELAN-Analysis 1 Group. (H1-02/95-429), (1995).

[53] D. Milstead. *Private Communication.*

[54] H.P Wellisch and C. Leverenz. *Measurement of the Proton Structure Function* $F_2(x, Q^2)$ *in the Medium* Q^2 *Region with the H1 Detector at HERA.* (H1-08/95-447), (1995).

[55] H1 Collaboration. *Measurement of the* e^+ *and* e^- *Induced Charged Current Cross Sections at HERA. Z. Phys.*, **C67**:565–575, (1995).

[56] André Schöning. *ASCOSM, Cosmic Finder auf Basis Topologischer Energieverteilungen*, Internal Electroweak Group Note. (1993).

[57] Karsten Reuter. *Description of the KTR-Finder to Identify Muons*, Internal Electroweak Group Note. (1995).

[58] A. Pieuchot et al. *Pile-Up Energy Detection using the Liquid Argon Big Tower Timing Information.* (H1-01/95-423), (1995).

[59] T. Carli et al. *Performance of the H1 LAr Trigger in 1994.* (H1-01/95-444), (1995).

[60] J.P. Sutton. *Private Communication.*

[61] H1 Collaboration. *Observation af an* $e^+p \rightarrow \mu^+X$ *Event with High Transverse Momentum at HERA.* (94-248), December (1994).

[62] S.J de Jong and J.J Engelen. *Proceedings of the Workshop Physics at HERA*, vol. 2. page 533, (1987).

[63] A. Mehta. *Measurement of the Diffractive Proton Structure Function and Calibration of the Forward Muon Detector at H1*, ph. d thesis. (RALT-037), (1994).

[64] J.P. Phillips. *The Deep-Inelastic Stucture of Diffraction*, ph.d thesis. (RALT), (1995).

[65] A. Mehta. *Private Communication.*

[66] Electroweak Group. *Private Communication.*

[67] *Physical Review D, Particles and Fields*, Part 1, American Physical Society. (1994).

[68] R.J Barlow. *Statistics*, Manchester Physics Series, John Wiley and Sons. (1989).

Acknowledgements

Thank Christ that's over.

Well, nobody seems to think it too pretentious to have acknowledgements filled with quotes, so here's one from His Bobness:

> "*I wish that for just one time*
> *You could stand inside my shoes*
> *And just for that one moment*
> *I could be you*
>
> *Yes, I wish that for just one time*
> *You could stand inside my shoes*
> *You'd know what a drag it is*
> *To see you*"
>
> *Positively 4th Street*

Yeah, well, I was going to have that awfully whimsical Groucho Marx quote about clubs and members, but then I never really did sign up, so I suppose it's not appropriate.

I am indebted to many people who have helped me and guided me throughout these last few years. Firstly, I would like to thank the people who matter the most: my parents for their extraordinary help and support and Verena Veitinger for her love and tolerance particularly over the last six months when she must have been on the verge of nausea with having to listen to me moaning about that thesis.

Now it's been said before that "without his help and selfless dedication none of this would have been possible" and you know it's not meant. In my case, however, it's safe to say that without the assistance of Andrew Mehta and Little Davey Milstead, there wouldn't be a thesis at all. As well as being the cleverest person in the world, and quite apart from developing all the code and analysis tools used in this work, Andrew is to be thanked for allowing me to take nine months to do something he could manage in five minutes. Yeah, I exaggerate a bit, it would have taken him no more than two. If it hadn't been for Dave's help with Fortran, willingness to answer my stupid questions and illuminating philosophies aired during those breaks, I would have packed up, forgotten about the thesis and got a proper job. Uh, yeah, thanks.

Then, of course, there was that man, Dr Paul Sutton: a gentleman, a scholar and a force of nature, who I'll have a pint with anytime, sir. He, along with Stuart Robertson, picked me up and got me started and sang "New York, New York" and is also one of the main reasons for me completing this thesis.

Thanks to my fellow Manc lads, Peter Bispham and Mark Burton, for sharing all of those Hamburg days, for their dedication to the cause of yobbery and for not leaving me to die on the Reeperbahn. Thanks to Alan Wilson too, for his unique contribution to high culture. My thanks also go to the following DESY people: 'TC' Phillip Biddulph, Chris Hilton, Roland Martin, Dave Cussans, Ben Waugh, Achim Braemer and the Electroweak boys, Julian Phillips, Vicky Hudgson and Lee West.

Back in Manchester, I would like to thank my supervisor, Professor Robin Marshall for all his help, advice, support and encouragement. I am extremely grateful to Roger Barlow for his willingness to help with all my tedious and trying statistics problems and I also very much appreciated the words of encouragement from Mike Ibbotson, Fred Loebinger, Joe Foster and Trudy Denny. Thanks also go to Fred for his supervision in my first year and for allowing me on this course to begin with.

Thanks to Colin Denté, a true polymath turned entrepreneur, and those free thinkers Roger Manvell and Robert Butler. I am also grateful to Big Dave Hutchinson and Steve Lane for their drinking antics and for leaving me to look after their coats and to Nico Petropoulis for, well, being himself. Nick Lumb is to be thanked for putting up with my loutishness and for his culinary tips and a big thank you goes to the Greenhall family for all their hospitality during my Manchester days.

Then there's Wayne Santana, Dwight Spears, Abdul the alchemist and Robert Anton Wilson, all of whom provided me with much entertainment. A special mention mention also goes to Tom, Ella, Max and the Elk.

Anyways, I'm all out of sycophancy, so I s'pose that's it. End of thesis. I'm sure you enjoyed reading it as much as I did writing it.